

University of Nevada, Reno

**Electroporation of Intracellular Membranes of Adrenal
Chromaffin Cells with High Intensity, 5-ns Electric
Pulses: an Experimental and Modeling Study**

A dissertation submitted in partial fulfillment of the requirements for the degree of
Doctor of Philosophy in Biomedical Engineering

By
Josette El Zaklit

Dr. Indira Chatterjee/Dissertation Advisor
Dr. Gale Craviso/Dissertation Co-advisor

December 2016

© by Josette El Zaklit 2016
All Rights Reserved



THE GRADUATE SCHOOL

We recommend that the dissertation
prepared under our supervision by

JOSETTE EL ZAKLIT

Entitled

**Electroporation Of Intracellular Membranes Of Adrenal Chromaffin Cells With
High Intensity, 5-Ns Electric Pulses: An Experimental And Modeling Study**

be accepted in partial fulfillment of the
requirements for the degree of

DOCTOR OF PHILOSOPHY

Dr. Indira Chatterjee, Advisor

Dr. Gale Craviso, Committee Member

Dr. Yantao Shen, Committee Member

Dr. Jihwan Yoon, Committee Member

Dr. Normand Leblanc, Graduate School Representative

David W. Zeh, Ph. D., Dean, Graduate School

December, 2016

ABSTRACT

Externally applied nanosecond-duration electric pulses (NEP) can affect cells by permeabilizing the plasma membrane, resulting in the formation of nanopores, as well as by porating membranes of intracellular organelles that can lead to Ca^{2+} release from internal stores. In this regard, we have previously reported that when excitable adrenal chromaffin cells are exposed to up to ten, 5-ns pulses applied at an electric field amplitude of 5-6 MV/m, the only response observed is Ca^{2+} influx through voltage-gated Ca^{2+} channels. The mechanism underlying voltage-gated Ca^{2+} channel activation is attributed to Na^+ influx via nanopores. In contrast, there is no evidence of Ca^{2+} release from intracellular stores due to intracellular poration of Ca^{2+} -storing organelles, such as the endoplasmic reticulum (ER).

Using a combination of experimental and numerical modeling approaches, the goal of this study was to elucidate the basis for the lack of poration of intracellular Ca^{2+} stores in chromaffin cells exposed to a 5-ns, 5-6 MV/m pulse. Fluorescence imaging of intracellular Ca^{2+} levels together with whole-cell recordings obtained in patch clamped cells indicated that the E-field amplitude that was required to cause Ca^{2+} release from intracellular stores, which was identified as the ER, was twice the E-field amplitude required to cause plasma membrane permeabilization (8 MV/m versus 4 MV/m, respectively). A numerical model of a chromaffin cell was constructed to understand the requirement for the higher E-field amplitude to cause intracellular membrane poration. While initial modeling results agreed with the experimental findings with respect to the E-field threshold amplitude required to

electroporate the plasma membrane, they did not show that intracellular membrane poration required a higher E-field amplitude. Therefore, the model was refined by using realistic sizes and measured dielectric properties of secretory granules to confirm the source of intracellular Ca^{2+} released and understand the requirement for the high E-field amplitude to electroporate the membrane of intracellular organelles. Modeling results identified the ER as the primary target of the NEP, and highlighted the importance of knowing accurately the electrical properties of the different structures to understand the basis for intracellular membrane permeabilization.

Establishing agreement between the experimental and modeling results is essential for understanding why high E-field thresholds for stimulating chromaffin cells by causing Ca^{2+} influx that triggers exocytosis and catecholamine release, and those for causing unwanted effects on intracellular structures differ by more than twofold in magnitude. Such knowledge is important for the potential use of NEPs as a novel stimulus for modulating neurosecretion.

Dedicated to my family.

ACKNOWLEDGEMENTS

At the beginning of this dissertation, I would like to take the time to thank all the people who in one way or another have contributed to making this work possible.

First and foremost, I would like to express my sincere gratitude to both of my advisors Dr. Indira Chatterjee and Dr. Gale Craviso who have given me the opportunity to work on this fascinating project and for continuously supporting, helping and inspiring me throughout my PhD journey. I am highly grateful for their aspiring guidance, motivation, stimulating discussions and constructive criticism. Without their valuable supervision this dissertation would not have been accomplished.

Besides my advisors, I am highly grateful to Dr. Normand Leblanc for his insightful comments and questions during the research meetings.

I would also like to thank Dr. Jihwan Yoon for all the help he provided me when I first joined the research group, mainly for making electrodes, writing LABVIEW codes and running SEMCAD simulations.

I offer my sincere gratitude to Dr. Yantao Shen for being part of my committee.

I gratefully acknowledge Dr. Lisha Yang for isolating and culturing bovine chromaffin cells, performing patch clamp experiments and providing me with the data to complement my experimental and numerical modeling results.

I would also like to express my deepest appreciation to Robert Terhune who was always willing to help, for running SEMCAD simulations and for spending time to work on the clusters.

I gratefully acknowledge Dr. Michael Stacey (Old Dominion University) and Dr. Ahmet Can Sabuncu (Southern Methodist University) for determining the dielectric properties of chromaffin cells. I am also thankful to Dr. Nina Semenova (Old Dominion University) for dissociating cells to perform the dielectric measurements.

I am immensely grateful to Dr. James Weaver (Massachusetts Institute of Technology) and Dr. Thomas Vernier (Old Dominion University) for their valuable and instructing discussions. I am also thankful to Dr. Seung Hyun Yoo (Incheon, Korea) for taking time to answer my questions about secretory granules.

I also offer my gratitude to the undergraduate students who worked in the laboratory, especially to Jordanna Payne for making electrodes, Eric Evans for helping with the picospritzer, Steve Shen for writing LABVIEW codes and Jonathan Watterson for his lab support. I would also like to thank Mike Maskaly for machining the holder for the electrodes and the stand for the perfusion system, and Mike Holcomb for providing fresh bovine adrenal glands.

I thankfully acknowledge the Air Force Office of Scientific Research (AFOSR Grant FA9550-14-1-0018) for providing the funding that made my PhD work possible.

Most importantly I could not have accomplished this work without my family by my side. I would like to thank my mom and dad for taking care of my three little boys, and for their love and immense support.

Last but not least, I would like to offer my sincerest gratitude to my loving, encouraging and patient husband whose continuous support during the dissertation is so appreciated.

TABLE OF CONTENTS

LIST OF TABLES	ix
LIST OF FIGURES	x
LIST OF ABBREVIATIONS	xii
CHAPTER 1. Introduction	1
1.1. Nanosecond electric pulses (NEPs), a tool for intracellular manipulation ...	1
1.1.1. Theoretical approach	2
1.1.2. Spatially distributed continuum models	4
1.1.3. Molecular dynamics (MD) simulations	5
1.1.4. Experimental approaches	6
1.2. NEPs, a potential novel stimulus for neuromodulation	9
1.2.1 Excitable adrenal chromaffin cells, a model of neurosecretion	9
1.2.2 Chromaffin cell function	10
1.2.3 Responses of chromaffin cells to 5-ns pulses	12
1.2.4 Questions to be addressed	13
1.3. Dissertation outline	15
CHAPTER 2. Implementation and Validation of a 2D Numerical Model of a Cell Exposed to a NEP	18
2.1. Introduction	18
2.2. Methods	19
2.2.1 Cell system geometry	19
2.2.2 Cell system mesh and Voronoi cells (VC)	21
2.2.3 Meshed transport network method (MTNM)	26
2.2.4 Asymptotic model of electroporation	27
2.3. Results	30
2.3.1 Spatial response	30
2.3.2 Angular response	34
2.3.3 Temporal response	37
2.4. Review of the electrical properties of cells	39
2.5. Conclusions	44

CHAPTER 3. Exposing Adrenal Chromaffin Cells to 5-ns Electric Pulses Requires Higher Electric Fields to Porate Intracellular Membranes than for Porating the Plasma Membrane	45
3.1. Introduction	45
3.2. Materials and methods	46
3.2.1 Chromaffin cell isolation, culturing and dissociation	46
3.2.2 Fluorescence imaging of intracellular Ca²⁺ levels	47
3.2.3 Statistical analysis	48
3.2.4 Whole-cell recording of membrane conductance	49
3.2.5 NEP exposure	50
3.2.6 Reagents	54
3.2.7 2D cell modeling	56
3.3. Results	68
3.3.1 Experimental findings	68
3.3.2 Numerical modeling results	78
3.3.3 Reducing the electrical conductivity of the secretory granule interior increased the E-field threshold required for electroporating the granule membrane	84
3.4. Discussion	86
3.4.1 Plasma membrane permeabilization	87
3.4.2 Permeabilization of the membranes of intracellular Ca²⁺-storing organelles	88
3.5. Conclusions	93
CHAPTER 4. Exposing Adrenal Chromaffin Cells to High Intensity, 5-ns Electric Pulses Causes Electroporation of the ER Membrane	95
4.1. Introduction	95
4.2. Materials and methods	96
4.2.1 Chromaffin cell isolation, culturing and dissociation	96
4.2.2 Fluorescence imaging of intracellular Ca²⁺ levels	97
4.2.3 NEP exposure	99
4.2.4 Reagents	103
4.2.5 2D model of chromaffin cell organelles	104
4.3. Results	113

4.3.1	Experimental findings	113
4.3.2	Numerical modeling results	128
4.4.	Discussion	134
4.4.1	Characteristics of NEP-induced Ca^{2+} release from the ER	135
4.4.2	Identification of the source of Ca^{2+} released in response to a 5-ns pulse.	137
4.4.3	Comparison between the modeling and experimental results	141
4.5.	Conclusions	145
CHAPTER 5. Conclusions and future work		146
5.1	Further refinement of the numerical model: modeling a realistic shape of the ER.....	149
5.2	Further exploration of a possible shielding effect	150
5.3	Other possible mechanisms responsible for intracellular Ca^{2+} release	150
REFERENCES.....		152
APPENDIX A: Abstract of Paper Presented at the Annual Meeting of Bioelectromagnetics Society (BioEM2015), Asilomar, CA, June 14-19, 2015		165
APPENDIX B: Abstract of Paper Presented at the Annual Meeting of Bioelectromagnetics Society (BioEM2016), Ghent, Belgium, June 5-10, 2016.....		169

LIST OF TABLES

Table 2.1: Electrical parameters used in the 2D cell model [93].	25
Table 2.2: Electroporation parameters used in the 2D cell model [93,96].	30
Table 2.3: Summary of the electrical properties of cells [97,99-104].	42
Table 2.4: Summary of the electrical properties of nuclei [97,101,102].	43
Table 2.5: Summary of the electrical properties of mitochondria [105,106].	43
Table 2.6: Measured dielectric properties of chromaffin cells.	43
Table 3.1: Geometrical parameters used in the 2D cell model.	60
Table 3.2: Electrical parameters used in the 2D cell model [102,109,111].	65
Table 3.3: Electroporation parameters used in the 2D cell model [93,96].	68
Table 3.4: Temperature increase as a function of E-field amplitude.	71
Table 4.1: Electrical parameters used in the 2D model of chromaffin cell organelles.	109
Table 4.2: Electroporation parameters used in the 2D model of chromaffin cell organelles [93,96].	112

LIST OF FIGURES

Fig. 1.1. Schematic diagram of the E-field distribution around and through the cell for different pulse durations.	4
Fig. 1.2. Physiological stimuli for neurosecretion.	11
Fig. 1.3. Stimuli for evoking catecholamine release from chromaffin cells.	14
Fig. 2.1. Cell system geometry.	20
Fig. 2.2. Schematic showing the anodic and cathodic poles on the cell membrane.	21
Fig. 2.3. Cell system mesh.	23
Fig. 2.4. Cell system Voronoi cells.	24
Fig. 2.5. Schematic representing the relationship between the triangular mesh and associated VCs.	25
Fig. 2.6. Equivalent electrical circuit for the membrane.	29
Fig. 2.7. Spatial distribution of the electric potential and pore density at different time points during (1.5, 3.6 and 8.5 ns) and after (1 μ s, 30 s) pulse application.	33
Fig. 2.8. Angular response of the TMP and pore density on the plasma membrane during and after pulse application.	36
Fig. 2.9. Angular response of the TMP and pore density on the nuclear membrane during and after pulse application.	38
Fig. 2.10. Temporal response of the TMP at the poles of the plasma and nuclear membranes (PM and NM, respectively).	39
Fig. 2.11. Temporal response of the TMP and pore density at the anodic pole of the cell membrane following pulse application.	40
Fig. 3.1. Photograph of the actual experimental setup used for patch clamp whole-cell recording.	50
Fig. 3.2. Details of the NEP exposure system.	53
Fig. 3.3. Details of the FDTD simulations.	56
Fig. 3.4. Cell system geometry.	59
Fig. 3.5. Cell system mesh.	61
Fig. 3.6. Cell system Voronoi cells.	63
Fig. 3.7. Equivalent electrical circuit for the membrane.	67
Fig. 3.8. Release of Ca^{2+} from intracellular stores in chromaffin cells evoked by a 5-6 ns pulse.	70
Fig. 3.9. Lack of effect of a 17 MV/m pulse on chromaffin cell morphology.	73
Fig. 3.10. Ca^{2+} transients evoked by carbachol.	75
Fig. 3.11. E-field thresholds for plasma membrane permeabilization and Ca^{2+} influx. ...	77
Fig. 3.12. Influence of σ_{cyto} on the electroporation of the plasma membrane.	80
Fig. 3.13. Transmembrane potential (TMP) and pore density as a function of E-field amplitude.	82

Fig. 3.14. Temporal evolution of pore density computed at the anodic pole of the different cellular membranes in response to a pulse applied at an E-field amplitude of 4 MV/m.....	83
Fig. 3.15. Influence of σ_{cyto} on the E-field threshold amplitudes required for electroporation of the nuclear envelope, OMM, IMM, ER and secretory granule membranes.	85
Fig. 3.16. Pore density computed at the anodic pole of the granule membrane, at the end of the pulse, for the different conductivities of the granule interior.	86
Fig. 4.1. Details of the NEP exposure system.....	100
Fig. 4.2. Details of the SEMCAD X FDTD simulations.	103
Fig. 4.3. Zoomed-in view of the model geometry illustrating the different organelles..	105
Fig. 4.4. Mesh and VCs of the localized 2D geometric model.	108
Fig. 4.5. Equivalent electrical circuit for the membrane.....	112
Fig. 4.6. Representative fluorescence Ca^{2+} trace in chromaffin cells at rest in the absence of extracellular Ca^{2+}	114
Fig. 4.7. Representative Ca^{2+} transient evoked by continuous application of carbachol via perfusion in the absence of extracellular Ca^{2+}	116
Fig. 4.8. Representative intracellular Ca^{2+} responses of chromaffin cells exposed to a single 5-ns pulse applied at an E-field amplitude of 17 MV/m in the absence of extracellular Ca^{2+}	116
Fig. 4.9. NEP-evoked Ca^{2+} responses in chromaffin cells in the presence of caffeine and absence of extracellular Ca^{2+}	119
Fig. 4.10. NEP-evoked Ca^{2+} responses in chromaffin cells in the presence of caffeine and ryanodine and absence of extracellular Ca^{2+}	122
Fig. 4.11. NEP-evoked Ca^{2+} responses in chromaffin cells in the presence of CPA and absence of extracellular Ca^{2+}	125
Fig. 4.12. NEP-evoked Ca^{2+} responses in chromaffin cells in the presence of caffeine, ryanodine and CPA and absence of extracellular Ca^{2+}	128
Fig. 4.13. Influence of σ_{ERin} on the E-field threshold amplitude required to electroporate the ER membrane.....	130
Fig. 4.14. Pore density calculated at the anodic pole of the ER membrane for $\sigma_{\text{ERin}} = 0.01$ S/m for the different configurations of the granules and electrodes.	132
Fig. 4.15. Spatial distribution of the electric potential in and around the ER for an applied E-field of amplitude 9 MV/m.	133
Fig. 4.16. Pore density computed at the anodic pole of the ER and granule membranes for a range of E-field amplitudes from 3 to 25 MV/m.	134
Fig. 4.17. TMP as a function of the applied E-field for different values of σ_{ERin}	143

LIST OF ABBREVIATIONS

BSS	Balanced salt solution
BSA	Bovine serum albumin
CICR	Ca ²⁺ -induced Ca ²⁺ release
CPA	Cyclopiazonic acid
DAG	Diacylglycerol
DMPP	1,1-dimethyl-4-phenylpiperazinium
E-field	Electric field
ER	Endoplasmic reticulum
HBSS	Hank's balanced salt solution
IMM	Inner mitochondrial membrane
IP ₃	Inositol-1,4,5-triphosphate
IP ₃ R	IP ₃ receptor
MD	Molecular dynamics
MTNM	Meshed transport network method
NEP	Nanosecond electric pulse
OMM	Outer mitochondrial membrane
PIP ₂	Phosphatidylinositol 4,5-bisphosphate
PLC	Phospholipase C
PMCA	Plasma membrane Ca ²⁺ -ATPase
REB	Reversible electrical breakdown
RyR	Ryanodine receptor

SERCA	Sarco/endoplasmic reticulum Ca ²⁺ -ATPase
TG	Thapsigargin
TMP	Transmembrane potential
V-ATPase	Vesicular H ⁺ -ATPase
VC	Voronoi cell
VGCC	Voltage-gated Ca ²⁺ channel

CHAPTER 1. Introduction

1.1. Nanosecond electric pulses (NEPs), a tool for intracellular manipulation

The ability of biological cells to interact with external electric pulses of different amplitudes and durations has enabled the use of these pulses to manipulate cell functions in a number of ways. Millisecond and microsecond duration pulses with amplitudes smaller than 1 MV/m have been shown to affect mainly the plasma membrane by creating transient aqueous pores in the lipid bilayer, a phenomenon known as electroporation [1-4]. Formation of pores in the plasma membrane allows molecules such as drugs and genes to be delivered to the cell interior [5-7]. Shortening the pulse duration into the nanosecond range has gained a lot of interest recently because of the ability of these pulses to reach the cell interior, interact with membranes of intracellular organelles, modulate cell functions and induce a number of cellular processes such as apoptosis [8-13]. The amplitude of these nanosecond pulses can reach several tens of MV/m with current day pulsers. If the amplitude is not too high, conservation of cell viability is possible [14]. Using NEPs to manipulate cells in this manner has opened up a new field of research with the potential to use NEPs for therapeutic benefits such as cancer therapy [13,15].

Several theoretical and experimental approaches have been used to study the interaction of electric field (E-field) pulses with biological cells. A theoretical approach first predicted an interaction of NEPs with intracellular structures [10,11]. Early experiments conducted in biological cells exposed to NEPs validated this theory [9,16]. Later, more sophisticated models were developed to represent complex NEP-induced phenomena such as

electroporation, both at the cellular [17-20] and molecular levels [3,4,21,22]. These modeling approaches were confirmed by experiments that reported NEP effects on cells and intracellular organelles. In the next section, theoretical and experimental approaches relevant to the work described in this dissertation will be discussed.

1.1.1. Theoretical approach

To understand the effect of pulsed E-fields on biological cells, the cell is represented by an equivalent electrical circuit in which the cell membrane, consisting of an insulating lipid bilayer, and the cytoplasm, considered as a conductive medium, are each represented by a resistance R and capacitance C placed in parallel [10,11]. When a spherical cell is exposed to an external E-field, E , charge accumulates on both sides of the cell membrane, resulting in a transient rise in transmembrane potential (TMP) V_m given by [23,24]:

$$V_m(t) = 1.5 r_{\text{cell}} E \cos\theta [1 - e^{(-t/\tau_m)}] \quad (1)$$

$$\text{with} \quad \tau_m = r_{\text{cell}} C_m (\rho_i + \rho_e / 2) \quad (2)$$

where r_{cell} is the cell radius, θ the angle between the normal to the cell membrane and the E-field direction, τ_m the time constant of the membrane, C_m the specific membrane capacitance, ρ_i and ρ_e the resistivities of the intracellular and extracellular media, respectively. The time constant τ_m is defined as the time required to charge the cell membrane and depends upon the electrical properties of the cell and of the medium surrounding it [25]. For example, for a mammalian cell with $r_{\text{cell}} = 10 \mu\text{m}$, $C_m = 1 \mu\text{F}/\text{cm}^2$, and $\rho_i = \rho_e = 100 \Omega\cdot\text{cm}$, the charging time is 150 ns. The TMP across an organelle membrane and the organelle membrane charging time can be calculated similarly [10].

Depending on the pulse duration (τ_p), the E-field can interact with the cell in different ways. When long duration pulses are applied such that $\tau_m < \tau_p$, the membrane charges fully and the E-field is excluded from the cell interior because the resistive component of the membrane dominates (Fig. 1.1a). However, when the pulse duration is shortened to the nanosecond range such that $\tau_m > \tau_p$, the capacitive component of the membrane becomes dominant, thus allowing the E-field to penetrate into the cell and affect intracellular structures (Fig. 1.1b) [11,18,26].

Because the TMP depends on the amplitude of the applied E-field, if E is increased such that V_m reaches a critical threshold voltage value of ~ 1 V, known as the threshold for reversible electrical breakdown (REB) [2,27,28], the membrane becomes extremely (5 orders of magnitude more) conductive because of transient aqueous pores forming in the lipid bilayer, a phenomenon known as electroporation [3,4,21,22]. By controlling the amplitude and duration of the applied electric pulse, it is possible to selectively affect the plasma membrane or intracellular membranes or both. For example, if a NEP is applied such that the voltage across an organelle membrane reaches the critical voltage before the plasma membrane, pores form in the organelle membrane while the plasma membrane remains intact [26]. The ability of NEPs to affect intracellular membranes without affecting the plasma membrane and cell viability led the researchers to study experimentally the effect of these ultrashort pulses, as will be discussed in a later section.

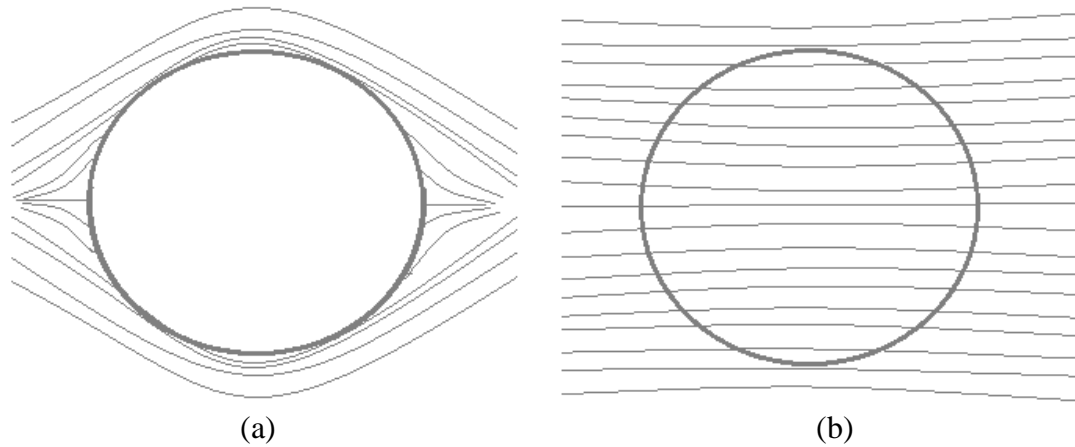


Fig. 1.1. Schematic diagram of the E-field distribution around and through the cell for different pulse durations. (a) For microsecond duration pulses the E-field is excluded from the cell interior. (b) For nanosecond duration pulses the E-field penetrates into the cell.

1.1.2. Spatially distributed continuum models

The theoretical approach provides a basic understanding of the interaction of E-fields with cell membranes and intracellular organelles, in the absence of electroporation (i.e. before the TMP reaches the critical voltage for electroporation). However, once electroporation occurs, more sophisticated numerical models are needed to predict the response of a cell to NEPs. Two spatially distributed continuum models were developed for this purpose [19,29]. These models can be coupled with nonlinear phenomena such as electroporation in which pore dynamics are defined by the Smoluchowski equation [2,30-35], thus giving a more complete quantitative representation of the cellular responses to a NEP. The Smoluchowski equation is a partial differential equation that describes pore distribution as a function of time and radius of pores, the size of which are heavily dependent on the pulse duration.

The first model used to describe pore dynamics is based on the asymptotic model of electroporation developed by Neu and Krassowska (1999) [34]. This model uses a fixed pore radius (~1 nm) and assumes that pores do not expand and that pore creation dominates pore expansion for high intensity (MV/m) NEPs [20]. The second model is more sophisticated and takes into account pore expansion and contraction, thus giving a more complete picture of pore dynamics and wherein the pores are assumed to have a variable radius [36-38]. Models with dynamic pores are most useful for microsecond duration pulses, which can create pores that can expand significantly allowing large molecules to go through [38-40]. Because of the ultrashort (< 10 ns) duration of the pulses used in this study, the asymptotic model of electroporation was adopted, as will be discussed in detail in Chapter 2 of this dissertation.

Simulations using microsecond duration pulses have shown that pores predominantly formed in the plasma membrane leaving the intracellular membranes unelectroporated [17,41]. However, when nanosecond duration pulses were used, the models predicted that membranes of intracellular organelles electroporated in addition to electroporation of the plasma membrane [17,41,42]. Due to the very short duration of the pulses used, spatially distributed models are useful for providing information about electroporation that is difficult to obtain experimentally, and are helpful in explaining and understanding the experimental observations.

1.1.3. Molecular dynamics (MD) simulations

MD is the only available computational method to date that provides a description of the effect of NEPs on the lipid bilayer at the atomistic and molecular level [3,21,22].

Because of the intensive computations required in MD simulations, only a small nanometer-size 3D membrane patch surrounded by an aqueous solution is typically modeled. Hundreds of lipid molecules forming the phospholipid bilayer and thousands of water molecules are included in the MD model. Ions such as Na^+ , K^+ and Cl^- can also be added to the system.

The formation of nanometer-diameter pores (nanopores) in the lipid bilayer by NEPs has been predicted by MD simulations. Upon application of the E-field, NEP-induced hydrophilic pores form in the lipid bilayer as evidenced by the penetration of water molecules into the membrane, forming a water chain across the bilayer [3,4,37]. MD simulations provide important pore information such as pore creation time, pore lifetime, pore radius, structure of the pore, transport and conductance properties of pores [37,43-45], information that cannot be easily obtained experimentally. Information obtained from MD simulations can be used in continuum models to help understand the interaction of NEPs with the lipid membranes at the molecular level.

1.1.4. Experimental approaches

Studying experimentally the effect of NEPs on intracellular structures required the development of new pulse generators producing high intensity ($> 1 \text{ MV/m}$) NEPs [46,47]. Initial studies indicated that NEPs mainly affected intracellular organelles, with little or no effects being detected on the plasma membrane [8,9,13]. In this regard, NEPs were shown to permeabilize intracellular granules in human eosinophils [9] and endocytotic vesicles in B16 F1 mouse melanoma cells [48]. Permeabilization was detected by entry of calcein from the cytosol into the granules [9] and release of lucifer yellow from the vesicles into

the cytosol [48]. Permeabilization of the nuclear membrane was evidenced by a decrease in fluorescence intensity of acridine orange in the nucleus of HL-60 cells in response to 10- and 60- nanosecond duration electric pulses [49]. NEPs also affected mitochondrial membranes by causing a loss of mitochondrial membrane potential, caspase activation and cytochrome *c* release in Jurkat and HL-60 cells [50,51].

Furthermore, NEPs have been shown to porate membranes of intracellular Ca^{2+} -storing organelles, specifically the endoplasmic reticulum (ER), leading to an increase in intracellular Ca^{2+} levels [52-56]. In some of these studies the ER was identified as the source of intracellular Ca^{2+} released since depletion of the ER of Ca^{2+} abolished the NEP-induced Ca^{2+} rise [54]. Other effects such as activation of signaling pathways inside the cell leading to accumulation of inositol-1,4,5-trisphosphate (IP_3) in the cytoplasm have also been reported [57,58].

Later studies showed that the plasma membrane was also affected by NEPs as demonstrated by phosphatidylserine externalization using fluorescence microscopy [22,59]. The passage of normally non-permeant dyes such as propidium iodide and YO-PRO-1 through the membrane to the cell interior [60] and the formation of nanopores in the lipid bilayer that allowed small ions to penetrate into cells [61,62,63-70] have also been used as indicators of plasma membrane permeabilization.

A more sensitive technique, allowing better detection of NEP-induced plasma membrane permeabilization, is whole-cell patch-clamp electrophysiology. Studies using the patch clamp technique showed that 60- and 600-ns duration electrical pulses cause long-lasting nanopores in the plasma membrane of GH3, PC-12, Jurkat and CHO-K1 cells as determined from an increase in the inward current and plasma membrane ion

conductance [65,67]. The size of the nanopores was suggested to be less than 1 nm, agreeing with theoretical models that predict the formation of nanometer-sized pores by NEPs in the lipid bilayer [37,60].

Another example of NEP-induced effects on the plasma membrane was reported in a study conducted in CHO cells using fluorescence imaging of Ca^{2+} [54]. The authors showed that a single 60-ns electric pulse causes nanopore formation in the plasma membrane as evidenced by Ca^{2+} influx into cells, as well as in the membranes of intracellular organelles as evidenced by Ca^{2+} release from intracellular stores [54]. These experiments agreed with continuum models that predicted the formation of nanopores in the plasma membrane as well as in the membranes of intracellular organelles.

Experimentally observed NEP-induced effects have been reported in studies conducted mainly on non-excitabile cells such as Jurkat T-lymphocytes [52,53], CHO cells [54,55] and HL-60 cells [56,57]. However, a few studies were conducted to understand how NEPs affect excitable cells such as cardiac myocytes [71], neurons [58,72], GH₃ cells [69,70] and chromaffin cells [73,74]. For example, Roth et al. (2013) showed that the plasma membrane of neural cells was permeabilized by a single 95- to 600-ns (0.84-16.2 KV/cm) pulse, and that the nanopores that formed were permeable to Ca^{2+} . Another study conducted by Wang et al. (2009) showed that multiple 4-ns (10-80 KV/cm) pulses caused Ca^{2+} -permeable pores to form in the plasma membrane of cardiomyocytes, and mobilized Ca^{2+} from intracellular stores by inducing action potentials.

Our research group at the University of Nevada Reno is among the few worldwide involved in studying NEP-induced effects on neural-type cells, investigating the mechanism by which ultrashort (< 10 ns) high intensity (> 1 MV/m) electric pulses interact

with the plasma membrane as well as with the membranes of intracellular organelles in excitable adrenal chromaffin cells.

1.2. NEPs, a potential novel stimulus for neuromodulation

Current electrical stimulation techniques use microsecond duration electric impulses for therapeutic purposes in a number of applications such as stimulation of muscle contraction [75], modulation of hormone secretion [76,77] and alteration of neuronal activity to treat neurological disorders [78,79]. Shortening the duration of the electric pulses from the currently used microsecond range to the nanosecond range could benefit currently used electric stimulation approaches for neurostimulation. In this regard, we have strong experimental evidence that high intensity (> 1 MV/m), 5-ns duration electric pulses can alter neural cell excitability by a novel mechanism without causing adverse effects on the cells [74,80]. In particular, our focus has been to understand the mechanism of interaction of 5-ns electric pulses with adrenal chromaffin cells that leads to alterations in cell excitability, causing the exocytotic release of catecholamines.

1.2.1 Excitable adrenal chromaffin cells, a model of neurosecretion

Chromaffin cells are a well-characterized *in vitro* model of neural-type/neurosecretory cells that have been extensively used to investigate the mechanisms underlying exocytosis. They are derived from the neural crest, reside in the medulla of adrenal glands and share many similarities to sympathetic neurons such as the synthesis, storage and release of the catecholamines epinephrine and norepinephrine, the latter using the same mechanisms

involved in synaptic transmission as neurons, i.e. exocytosis triggered by influx of Ca^{2+} through voltage-gated Ca^{2+} channels (VGCC) [81]. Compared to neurons, chromaffin cells are easy to isolate and maintain in suspension culture that preserves their round morphology. As will become evident in the following chapters, this simple spherical cell morphology was crucial for facilitating interpretation and analysis of experimental and cell modeling results. Below is a brief description of the basic function of these cells *in vivo*.

1.2.2 Chromaffin cell function

In vivo, the role of chromaffin cells is to release the catecholamines epinephrine and norepinephrine into the blood stream in response to stimulation of the sympathetic nervous system (fight-or-flight response). Each chromaffin cell is innervated by the splanchnic nerve that releases the neurotransmitter acetylcholine. When acetylcholine binds to nicotinic receptors, which are ligand-gated Na^+ channels present in the plasma membrane of chromaffin cells, it causes Na^+ influx and plasma membrane depolarization. When the cell is depolarized, VGCCs are activated allowing extracellular Ca^{2+} to enter the cell. The local rise in intracellular Ca^{2+} concentrations promotes granule fusion with the plasma membrane, exocytosis and release of catecholamines (Fig. 1.2) [82]. In addition, elevated intracellular Ca^{2+} triggers Ca^{2+} -induced Ca^{2+} release (CICR) from the ER through the ryanodine receptors (RyR). Intracellular Ca^{2+} levels are regulated by the function of several intracellular Ca^{2+} -storing organelles such as the ER, mitochondria and secretory granules. These organelles are present in close proximity to each other beneath the plasma membrane and contribute to regulating the exocytotic process [81-83].

Acetylcholine also binds to muscarinic receptors, which are G-coupled protein receptors present in the plasma membrane of chromaffin cells. When these receptors are activated, they in turn activate the membrane-associated enzyme phospholipase C (PLC). PLC hydrolyzes phosphatidylinositol 4,5-bisphosphate (PIP₂) into diacylglycerol (DAG) and IP₃. IP₃ diffuses through the cytosol to the ER, binds to the IP₃-receptors (IP₃R) in the ER membrane and causes Ca²⁺ to be released from the ER [84,85]. If Ca²⁺ is released next to the exocytotic site, it can increase the release of catecholamines. However, this exocytotic stimulus is minimal compared with that evoked by Ca²⁺ influx.

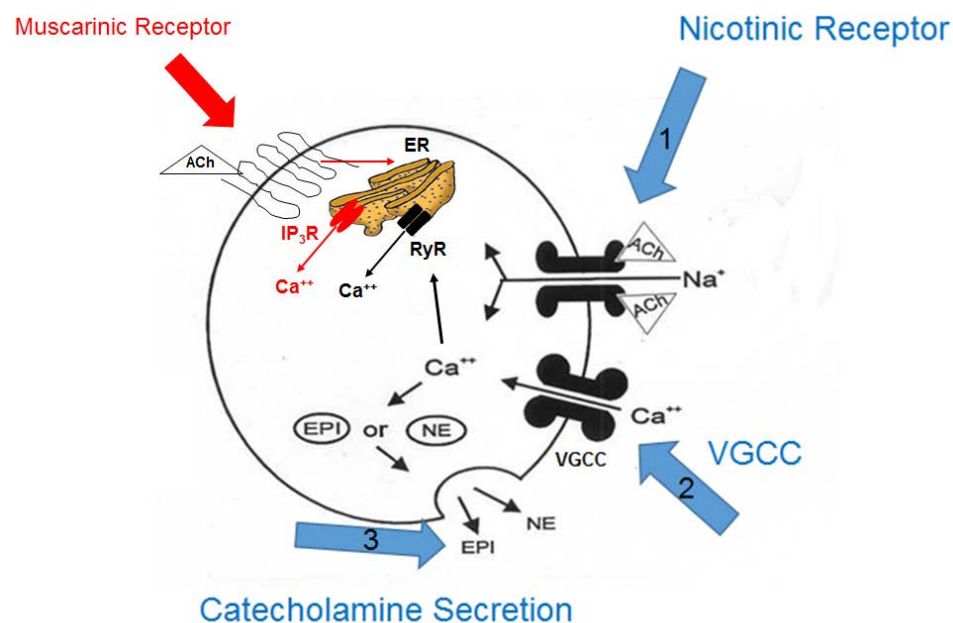


Fig. 1.2. Physiological stimuli for neurosecretion. Binding of ACh to the nicotinic receptors causes Na⁺ influx into the cell, activation of VGCCs and Ca²⁺ influx. Ca²⁺ entry causes CICR through the RyR in the ER. Binding of ACh to the muscarinic receptors causes activation of the PLC/IP₃ pathway inside the cell and Ca²⁺ release from the ER through the IP₃R. The increase in intracellular Ca²⁺ levels triggers granule fusion and exocytosis.

To terminate the Ca^{2+} signal, the excess intracellular Ca^{2+} is taken up rapidly by intracellular Ca^{2+} stores such as the mitochondria (through the mitochondrial Ca^{2+} uniporter) and the ER (via the sarco/endoplasmic reticulum Ca^{2+} -ATPase (SERCA) pump). Ca^{2+} can also be removed to the outside of the cell via the activity of the plasma membrane Ca^{2+} -ATPase (PMCA) pump and the $\text{Na}^+/\text{Ca}^{2+}$ exchange system. Once intracellular Ca^{2+} levels return to their basal concentration, the cell is ready for the next stimulus [82].

The ER, which is the most common Ca^{2+} source in chromaffin cells, contains ~ 3 mM Ca^{2+} , most of it is bound to low-affinity high-capacity Ca^{2+} -binding proteins present in the lumen of the ER [86,87]. Secretory granules have been postulated to be another Ca^{2+} source. Secretory granules occupy $\sim 30\%$ of the volume of the cytosol (20,000-30,000 granules/cell) [88] and contain the highest Ca^{2+} concentrations (~ 40 mM) which constitute more than 60% of the total Ca^{2+} content [89]. However, 99.9% of the granular Ca^{2+} is strongly bound to chromogranins A and B, which are high-capacity, low-affinity Ca^{2+} binding proteins, and only 0.1% of the intragranular Ca^{2+} is free (20-100 μM) [89]. Mitochondria also constitute an important source of Ca^{2+} in chromaffin cells [83]. These three Ca^{2+} -storing organelles represent potential targets of NEPs in chromaffin cells, as will be discussed in detail in the following chapters.

1.2.3 Responses of chromaffin cells to 5-ns pulses

As stated previously, our focus is to elucidate the basis for the mechanism by which NEPs alter chromaffin cell excitability. We have shown that exposing adrenal chromaffin cells to a single 5-ns, 5-6 MV/m pulse causes VGCC activation, Ca^{2+} influx, an increase in intracellular Ca^{2+} concentrations and the exocytotic release of catecholamines [73,74,90].

Fluorescence imaging of intracellular Ca^{2+} has shown that Ca^{2+} influx relies on Na^+ influx [74], and a recent study conducted by our group showed that a single 5-ns, 6 MV/m pulse permeabilizes the plasma membrane by causing NEP-induced inward currents that are carried mainly by Na^+ [91]. Important to note is that NEP-induced catecholamine release shares similarities to the normal physiological stimulus that evokes catecholamine release *in vivo*. Briefly, when acetylcholine binds to nicotinic receptors, it causes Na^+ influx, plasma membrane depolarization, activation of VGCCs, Ca^{2+} influx, an increase in intracellular Ca^{2+} levels and the exocytotic release of catecholamines (Fig. 1.3a). However, the pathway by which an NEP causes Na^+ to enter the cell is thought to be through ion-conducting nanopores formed in the plasma membrane and not through protein ion channels, as previously reported [74]. Thus, we hypothesize that a single 5-ns pulse reversibly depolarizes the plasma membrane by causing Na^+ -conducting nanopores in the lipid bilayer. The ability of a NEP to mimic the action of a physiological stimulus to evoke exocytosis (Fig. 1.3b) points to the potential use of NEPs as an alternate way for modulating neurostimulation.

1.2.4 Questions to be addressed

While we have shown that a single 5-ns, 5-6 MV/m electric pulse is capable of stimulating chromaffin cells and causing Ca^{2+} influx through VGCCs, exposing chromaffin cells to up to ten, 5-ns, 5-6 MV/m pulses does not cause release of Ca^{2+} from intracellular stores [90,92]. The lack of intracellular Ca^{2+} release in chromaffin cells using 5-ns electric pulses was surprising since one might expect that the ultrashort duration of these pulses would allow interaction of the NEPs with intracellular organelles. Therefore, the focus of

this dissertation was to address the issue of the lack of poration of membranes of intracellular Ca^{2+} stores in chromaffin cells.

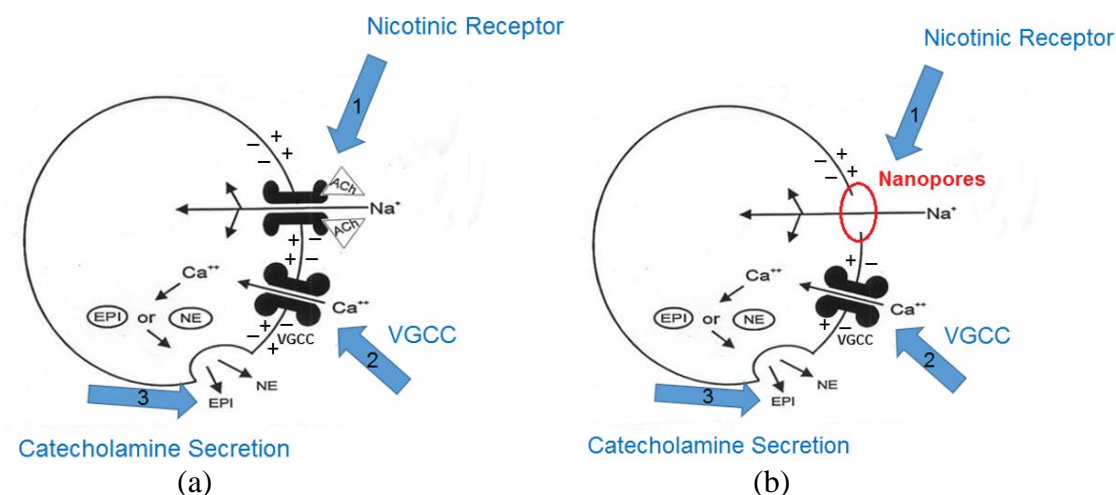


Fig. 1.3. Stimuli for evoking catecholamine release from chromaffin cells. (a) Catecholamine release *in vivo*. (b) Catecholamine release evoked by a NEP. Binding of acetylcholine (ACh) to the nicotinic receptor or the interaction of a NEP with the plasma membrane cause Na^+ influx into the cell (arrow 1), either through Na^+ channels or through nanopores, respectively. Na^+ influx causes plasma membrane depolarization, activation of VGCCs (arrow 2), Ca^{2+} influx, rise in intracellular Ca^{2+} levels and subsequent release of the catecholamines epinephrine (EPI) and norepinephrine (NE) (arrow 3).

Studies in CHO cells using 10-, 60- and 300-ns duration electric pulses reported that these NEPs caused nanopores to form in the membrane of the ER causing Ca^{2+} release that increased with the amplitude of the applied E-field. The authors also showed that short pulse durations (i.e. 10 ns) evoked higher intracellular responses compared to the long pulse durations (i.e. 60 and 300 ns) [54,55]. Based on these findings, it may be that the amplitude of the applied E-field (i.e. 5-6 MV/m) was too small to cause permeabilization of intracellular membranes in chromaffin cells and release of Ca^{2+} from internal stores.

This possibility was therefore thoroughly investigated in this dissertation, and depending on the outcome, the goal was to understand the basis for the findings.

1.3. Dissertation outline

Using a combination of experimental and numerical modeling approaches, the objective of this investigation was to understand why intracellular Ca^{2+} -storing organelles in chromaffin cells do not appear to be the target of 5-ns electric pulses.

The first approach employs fluorescence imaging experiments and patch clamp electrophysiology* to:

1. Determine whether Ca^{2+} release from intracellular Ca^{2+} stores occurs when chromaffin cells are exposed to E-field amplitudes higher than 6 MV/m.
2. Determine the E-field threshold amplitudes required to cause Ca^{2+} release from internal stores and those required to cause plasma membrane permeabilization.

Knowledge of these E-field thresholds is important for verifying that NEPs can excite chromaffin cells and cause Ca^{2+} influx that triggers exocytosis and catecholamine release without causing additional, unwanted effects on intracellular structures, such as poration of intracellular organelles.

3. Determine, in the case where intracellular Ca^{2+} release occurs, the source(s) of intracellular Ca^{2+} released.

* Patch clamp experiments were performed by Dr. Lisha Yang, Department of Pharmacology, University of Nevada Reno.

The second approach employs a 2D numerical model of a chromaffin cell exposed to a single NEP that was constructed based on the meshed transport network method (MTNM) developed by Smith and Weaver (2008) [40]. The model was refined based on the experimental findings and on actual dielectric properties measured in chromaffin cells. The aims of the model were to:

1. Identify the source(s) of intracellular Ca^{2+} release and validate it against the experimental findings.
2. Understand the basis for intracellular membrane permeabilization.

Refining the model based on the experimental observations to obtain the best agreement between the experimental and modeling results is one of the major goals of this study.

In summary, the dissertation is structured as follows:

Chapter 2 describes the detailed implementation of the 2D cell model with its validation against the cell model found in [93]. Chapter 3 uses a combination of experimental and numerical modeling approaches to determine the E-field threshold amplitudes required to cause electroporation of intracellular membranes and those required to cause electroporation of the plasma membrane. Chapter 4 describes the pharmacological approaches used to identify the source(s) of intracellular Ca^{2+} released in chromaffin cells by a 5-ns pulse and the refinements made to the numerical model to validate the source of intracellular Ca^{2+} and understand the requirement of high E-fields needed to electroporate intracellular membranes. Chapter 5 concludes this dissertation with a discussion of how this work might be extended in the future.

Chapters 3 and 4 of this dissertation as well as the measurements of chromaffin cell properties (discussed in Chapter 2) constitute the subject of three separate papers to be submitted to peer-reviewed journals following dissertation submission.

CHAPTER 2. Implementation and Validation of a 2D Numerical Model of a Cell Exposed to a NEP

2.1. Introduction

This chapter describes the implementation and validation of a 2D numerical cell model that was used to predict and understand the electrical response of a cell exposed to a single NEP. As stated in the Introduction, the model was based on the meshed transport network method (MTNM) developed by Smith and Weaver (2008) [40] and the asymptotic model of electroporation developed by Neu and Krassowska [34]. A brief description of both models is presented.

The Matlab code that was used to construct the model, compute all geometrical parameters as well as all circuit components, create netlists containing all node elements and connections in the circuits, and analyze the results was written by the author of this dissertation and represents an important part of this dissertation project. The 2D cell model was simulated using the circuit simulation software package LT SPICE IV (Linear Technology, Milpitas, CA, USA).

Validation of the model was essential to verify that the results obtained from the simulations agreed closely with the results published by Smith (2006) [93]. The model was validated by creating a geometry similar to the one described by Smith (2006) but with one intracellular organelle whereas two organelles were present in Smith's model, and by employing the same electrical (i.e. dielectric properties and pulse) and electroporation parameters used by Smith (2006) [93].

Since the accuracy of the dielectric properties of a cell and its organelles are critical in determining the accuracy of the numerical model and hence its correlation with experimental results, the chapter concludes with a thorough literature review of the dielectric properties of cells and organelles as determined in different cell types.

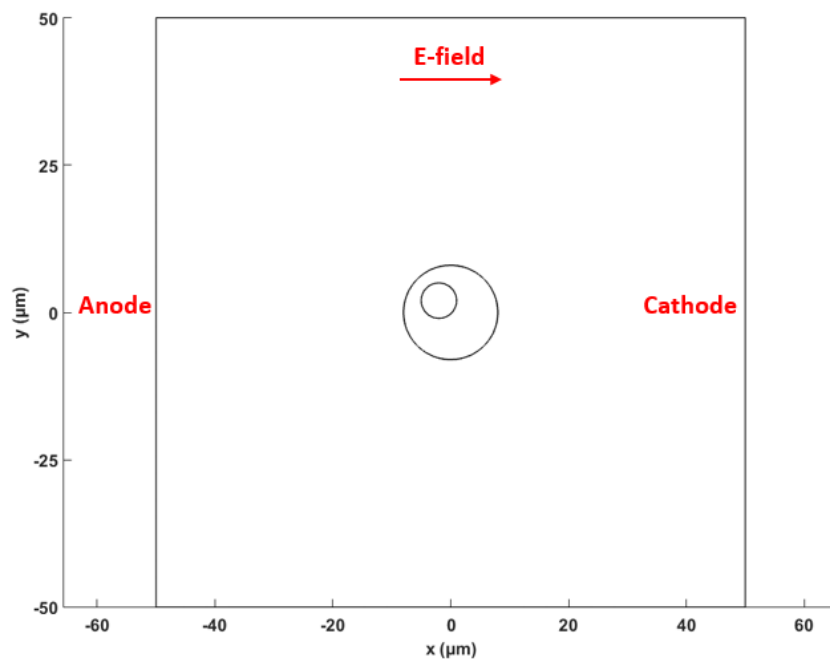
2.2. Methods

2.2.1 Cell system geometry

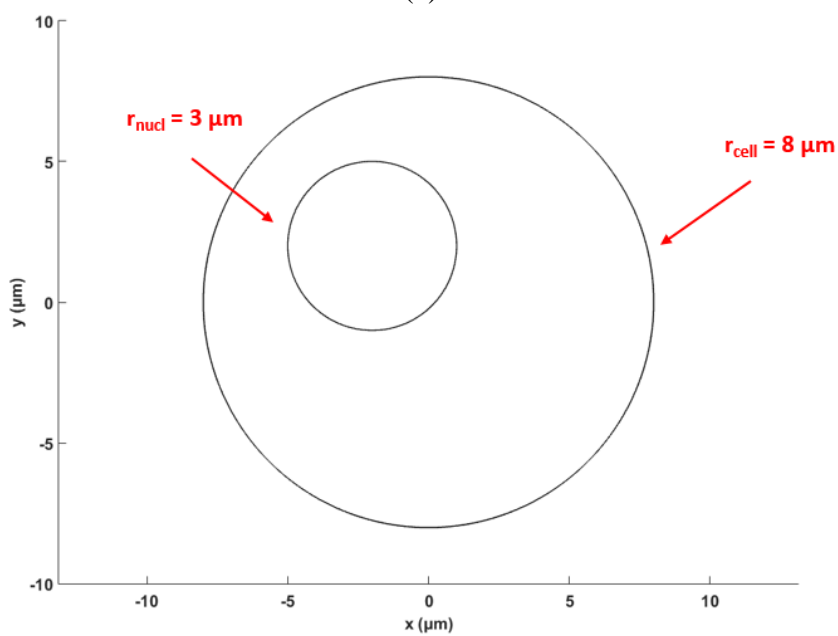
A 2D geometrical model of a cell was constructed in Matlab (2015a, Mathworks). The cell system geometry (Fig. 2.1a) consisted of a circle of radius $r_{\text{cell}} = 8 \mu\text{m}$, representative of a chromaffin cell [88], centered inside a bounding box (i.e. system boundary) of dimensions $100 \mu\text{m} \times 100 \mu\text{m}$. The system depth d was calculated by $d = (4/3)r_{\text{cell}} = 10.67 \mu\text{m}$, assuming that the cylindrical cell has the same volume as a spherical cell of the same radius [39].

A large structure representing a nucleus of radius $r_{\text{nuc}} = 3 \mu\text{m}$ [93] was placed offset inside the cell (Fig. 2.1b). The cell and nucleus had single membranes of thickness $d_m = 5 \text{ nm}$ [93]. The cell plasma membrane was assigned a resting potential of $V_{\text{rest}} = -86 \text{ mV}$ [93], and no resting potential was assigned to the nuclear membrane.

The E-field was applied by means of idealized planar electrodes placed at $x = -50 \mu\text{m}$ (anode) and $x = 50 \mu\text{m}$ (cathode). The E-field applied was calculated by dividing the voltage applied between the electrodes by the distance between the electrodes. The schematic in Fig. 2.2 shows the anodic and cathodic poles of a cell, i.e., the regions where the E-field is perpendicular to the cell membrane ($\cos \theta = 1$) and thus where the E-field amplitude is the highest.



(a)



(b)

Fig. 2.1. Cell system geometry. (a) The cell was centered in a 100 $\mu\text{m} \times 100 \mu\text{m}$ region. (b) A large structure representing the nucleus was placed inside the cell at (-2 μm , 2 μm).

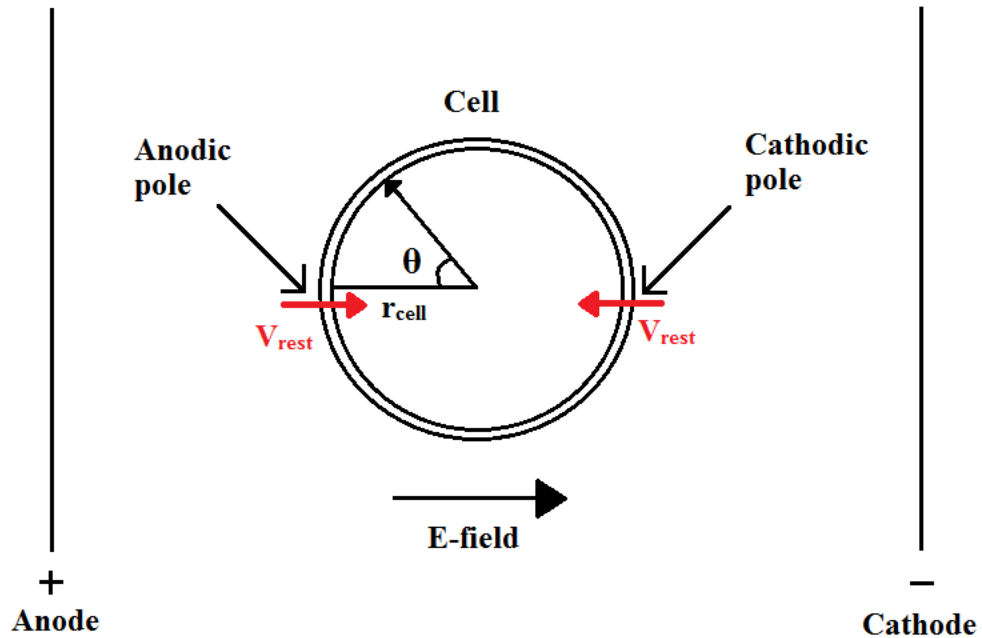


Fig. 2.2. Schematic showing the anodic and cathodic poles on the cell membrane. θ is the angle between the normal to the membrane and the direction of the E-field. V_{rest} represents the cell resting potential.

2.2.2 Cell system mesh and Voronoi cells (VC)

After constructing the geometry, a triangular mesh (Figs. 2.3a and 2.3b) was generated for the cell system using the mesh generation algorithm developed by Persson and Strang [94]. During mesh generation, nodes were fixed along the membranes. The triangular elements in the mesh varied in size, starting from a fine mesh in and around the membranes and increasing in size as the system boundary was approached. The cell and nuclear membranes had 51 and 19 membrane node pairs, respectively.

Each node in the triangular mesh was associated with a VC (Figs. 2.4a and 2.4b), which by definition encloses the region closer to that node than to any other node [95]. More specifically, the VCs represent the small volumes into which the entire domain is discretized (i.e., divided). The physical space was represented by the VCs and the computational space was represented by the circuit nodes that approximate the behavior of each VC with which they are associated (Fig. 2.5a).

The cell system was represented by equivalent electrical circuits (i.e. resistors R and capacitors C) placed between each pair of adjacent nodes and included subcircuits representing the electrolytes, membranes and pore densities, as described in detail in [93]. R and C values were computed based on the electrical properties (i.e. conductivity and permittivity) assigned to each region and on the geometrical parameters obtained from the mesh (i.e. distance between nodes and length of VC edges).

Matlab was used to compute all geometrical parameters and circuit components, and create netlists containing all node elements and connections in the circuits. Netlists were then imported into a circuit simulation software package LT SPICE IV (Linear Technology, Milpitas, CA, USA) where the 2D cell model was simulated. The generated data (i.e. node voltages and currents) were exported back into Matlab for plotting and analysis of the results. The electrical parameters used in the simulations were taken from [93] and are defined in Table 2.1.

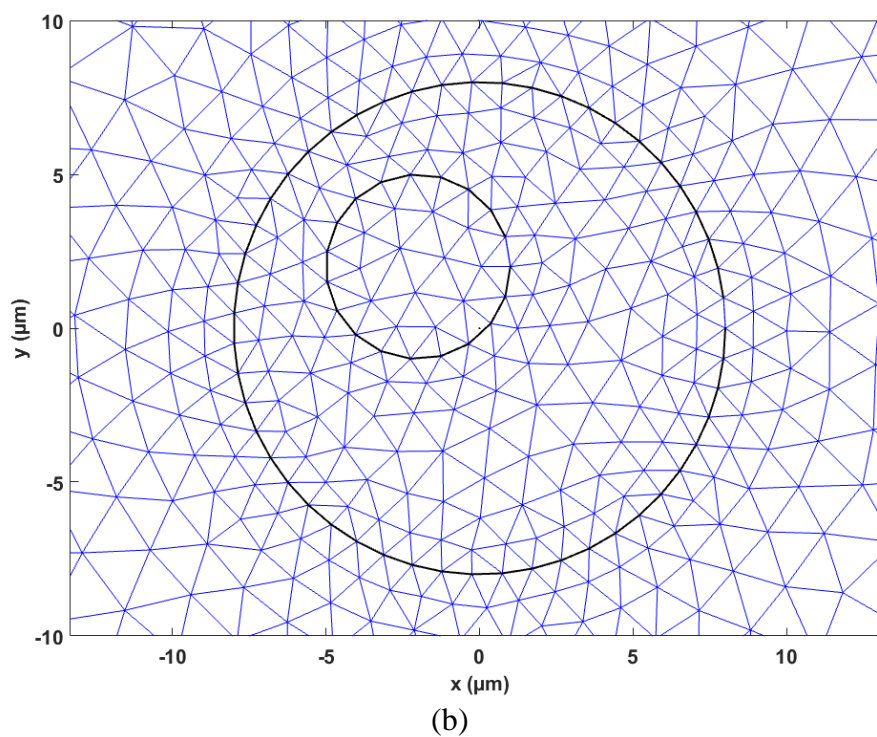
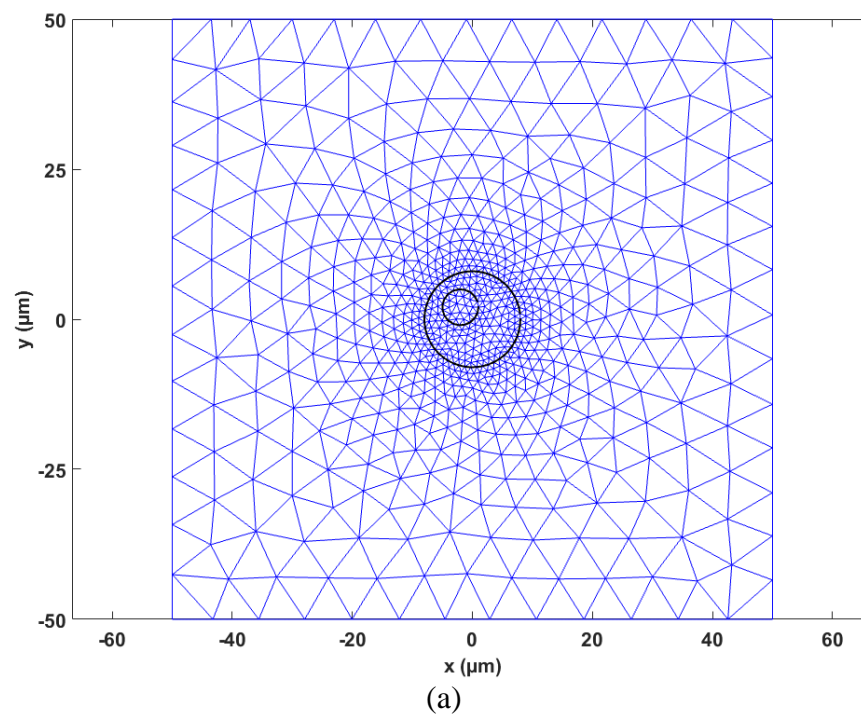


Fig. 2.3. Cell system mesh. The cell system mesh is shown at two scales (a,b). The mesh has 816 nodes, 1626 triangles and 2441 edges, and a 1 μm membrane node spacing.

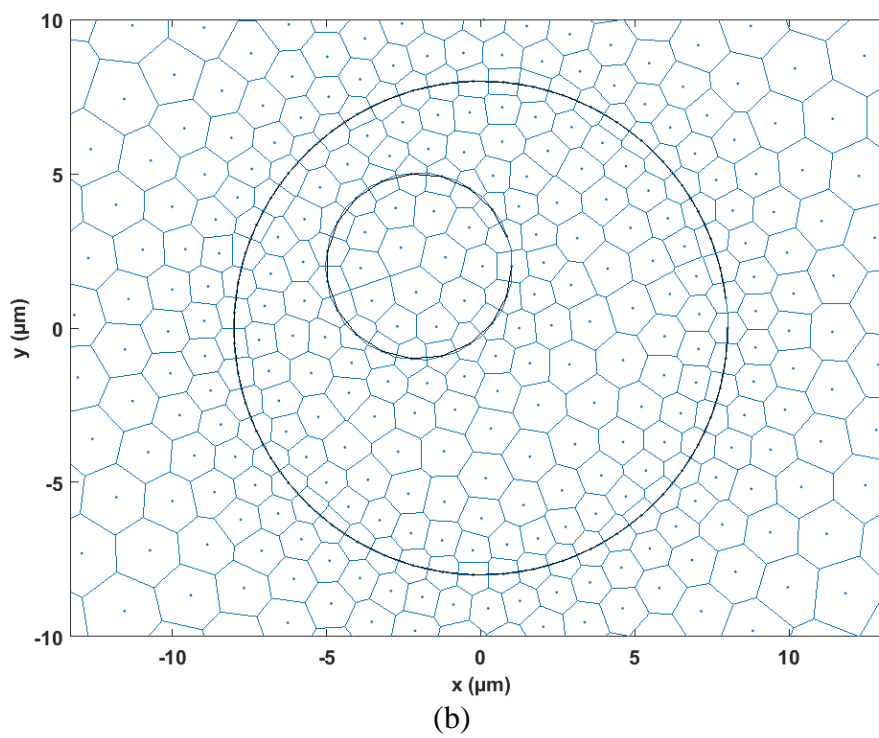
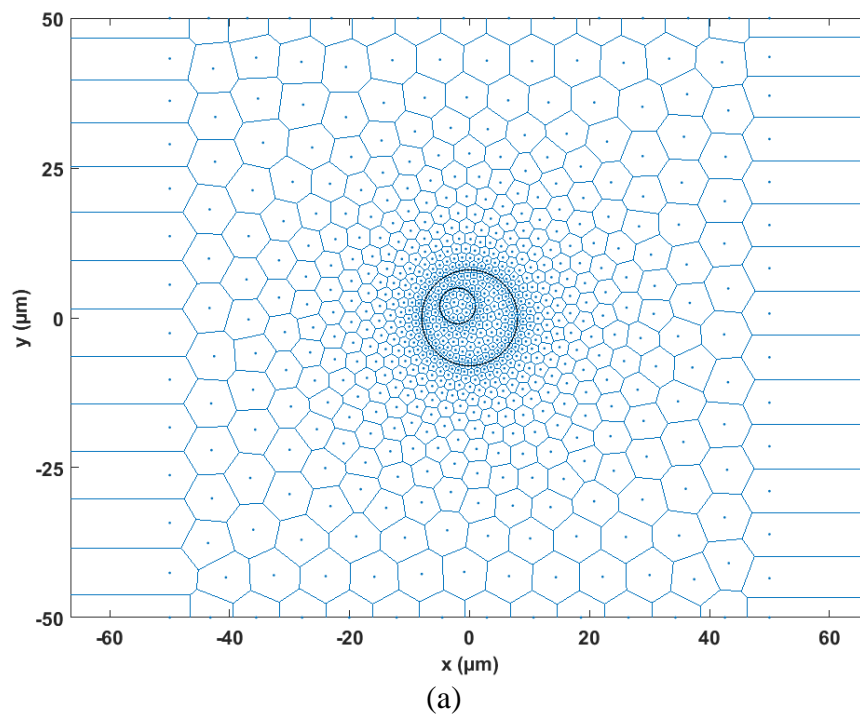


Fig. 2.4. Cell system Voronoi cells. The cell system Voronoi cells is shown at two scales (a,b).

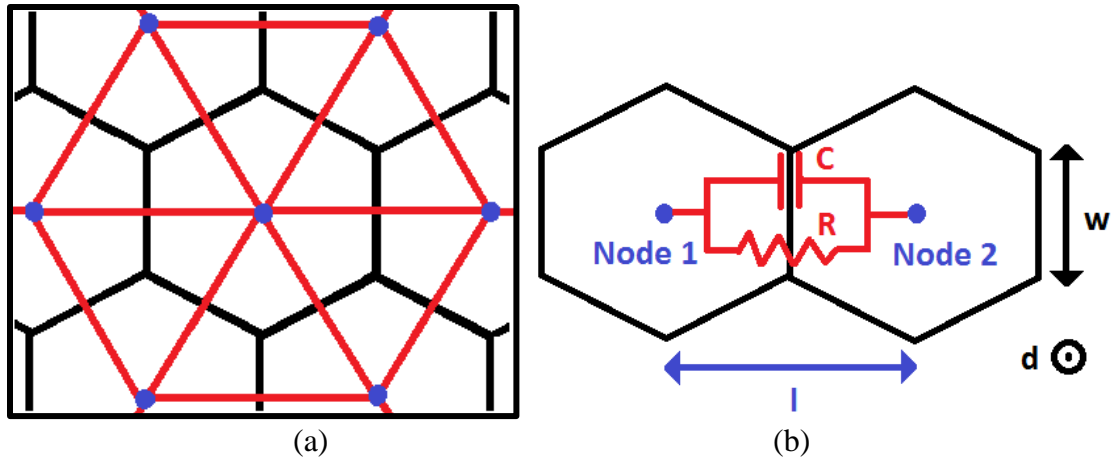


Fig. 2.5. Schematic representing the relationship between the triangular mesh and associated VCs. (a) The system is discretized into VCs, each associated with a node. Shown are the nodes (blue) connected by triangulation (red) and the VCs with which they are associated (black). The VC interface bisects the triangle edge at a right angle. (b) Circuit representation of the electrical transport between adjacent VCs.

Table 2.1: Electrical parameters used in the 2D cell model [93].

<u>Conductivity ($S.m^{-1}$)</u>	
Extracellular medium	1.2
Plasma membrane	9.5×10^{-9}
Nuclear envelope	9.5×10^{-9}
Cytoplasm	1.2
Nucleoplasm	1.2
<u>Relative permittivity</u>	
Extracellular medium	80
Plasma membrane	5
Nuclear envelope	5
Cytoplasm	80
Nucleoplasm	80

2.2.3 Meshed transport network method (MTNM)

The MTNM is a method that defines transport between adjacent volumes (represented here by the VCs) in terms of constitutive relations represented by equivalent circuit networks. Transport can be electrical, diffusive, thermal, etc. More complex nonlinear phenomena such as electroporation can also be modeled with the MTNM. In this dissertation, only electrical transport and electroporation are modeled using this method.

Electrical transport is represented by the constitutive relations that describe the total electrical current I that flows between adjacent VCs in terms of the electric potential V of the VCs [93]:

$$I = -\frac{\Delta V}{R} - C \frac{d}{dt}(\Delta V) \quad (1)$$

where ΔV is the potential difference between nodes, R and C are the resistors and capacitors placed between each pair of adjacent nodes (Fig. 2.5b). R and C are calculated based on the electrical properties assigned to each region and on the mesh geometry, from:

$$R = \frac{1}{\sigma} \frac{l}{wd} \quad (2)$$

$$C = \varepsilon \frac{wd}{l} \quad (3)$$

where σ and ε are the conductivity and permittivity assigned to each region, respectively, w the width of the VC interface between nodes, l the distance between nodes and d the system depth. Because two spatial variables (i.e., l and w) were varied in the constitutive relations with the depth of the system (d) being fixed, the model was considered a 2D model.

To include electroporation, each electrical circuit representing the membrane is associated with a pore density subcircuit that is used to compute the local pore density, transmembrane potential (TMP) and electroporation current through pores, as described below.

2.2.4 Asymptotic model of electroporation

The electrical response of the cell exposed to the NEP was modeled using the asymptotic model of electroporation [34] that describes the nonlinear changes in membrane conductance due to electroporation. This model assumes that pores do not expand for time durations in the nanosecond range and high amplitude electric pulses [20]. Hence, the pore radius is fixed at a value of 0.8 nm [93] throughout the simulations.

Pore dynamics are defined in the simplified form of the Smoluchowski equation, which is an ordinary differential equation given by [93]:

$$\frac{dN(t)}{dt} = \alpha e^{\left(\frac{V_m(t)}{V_{ep}}\right)^2} \left(1 - \frac{N(t)}{N_0} e^{-q\left(\frac{V_m(t)}{V_{ep}}\right)^2} \right) \quad (4)$$

where N is the local pore density, α the pore creation rate coefficient, V_m the transmembrane potential, V_{ep} the characteristic voltage of electroporation, N_0 the equilibrium pore density in the nonelectroporated membrane, and q an electroporation coefficient.

Modeling the membranes required the incorporation of the nonlinear changes in membrane conductance due to electroporation. In addition to the passive RC circuit that exists between each pair of nodes that span the membrane, a current source i_p representing

the current through pores was added to the membrane model (Fig. 2.6a). The current through pores in a small area A_m of the membrane was calculated from the conductance per pore G_m , the pore density N , and the TMP V_m by:

$$i_p(t) = G_p(V_m)N(t)A_m V_m(t) \quad (5)$$

The TMP was determined by the voltage difference across the membrane, and the conductance per pore, representing the increase in membrane conductivity due to electroporation, was calculated from:

$$G_p(V_m) = \sigma_p \frac{\pi r_m^2}{d_m} \frac{e^{v_m-1}}{\frac{\omega_0 e^{\omega_0 - \eta v_m - \eta v_m}}{\omega_0 - \eta v_m} e^{v_m} - \frac{\omega_0 e^{\omega_0 + \eta v_m + \eta v_m}}{\omega_0 + \eta v_m}} \quad (6)$$

where σ_p is the pore conductivity, r_m the fixed pore radius, d_m the membrane thickness, ω_0 the energy barrier inside a pore, η the relative entrance length of a pore, and v_m the dimensionless TMP given by:

$$v_m = \frac{V_m q_e}{kT} \quad (7)$$

$q_e = 1.6 \times 10^{-19}$ C is the charge of an electron, $k = 1.38 \times 10^{-23}$ J/K the Boltzmann constant, and T the absolute temperature.

The pore density N was calculated by solving equation (4) using the subcircuit shown in Fig. 2.6b. In this subcircuit, the voltage $N(t)$ across the capacitor C_N is given by:

$$\frac{dN(t)}{dt} = \frac{i_N(t)}{C_N} \quad (8)$$

where $C_N = 1/\alpha$ and $i_N(t)$, representing the current flowing into the capacitor, is given by:

$$i_N(t) = e^{\left(\frac{V_m(t)}{V_{ep}}\right)^2} \left(1 - \frac{N(t)}{N_0} e^{-q\left(\frac{V_m(t)}{V_{ep}}\right)^2} \right) \quad (9)$$

When the sum of the currents flowing into the node is positive, a positive current flows into the capacitor, the capacitor charges and the voltage $N(t)$ at the node increases, thus creating pores. Otherwise, when the sum of the currents flowing into the node is negative, a negative current flows into the capacitor, the capacitor discharges and the voltage $N(t)$ at the node decreases, thus destroying pores [93]. The electroporation parameters used in equations (4)-(9) were taken from [93,96] and are defined in Table 2.2.

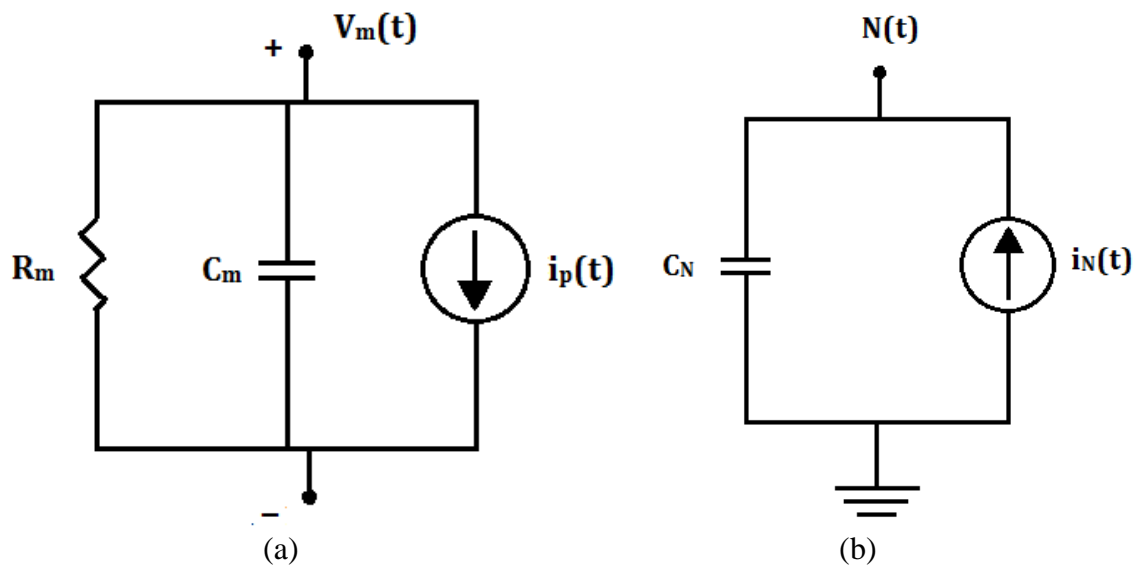


Fig. 2.6. Equivalent electrical circuit for the membrane. (a) Resistors R_m and capacitors C_m were placed between each pair of nodes spanning the membrane, in addition to the current i_p through pores. (b) The pore density subcircuit associated with each membrane circuit was used to solve the pore dynamics equation (4).

Table 2.2: Electroporation parameters used in the 2D cell model [93,96].

<u>Parameter</u>	<u>Value</u>
Pore creation rate coefficient (α)	$1 \times 10^9 \text{ m}^{-2} \text{ s}^{-1}$
Characteristic voltage of electroporation (V_{ep})	0.258 V
Electroporation coefficient (q)	2.46
Equilibrium pore density (N_0)	$1.5 \times 10^9 \text{ m}^{-2}$
Pore radius (r_m)	0.8 nm
Pore energy barrier (ω_0)	2.65 kT
Conductivity of aqueous solution in pores (σ_p)	1.2 S.m^{-1}
Pore relative entrance length (η)	0.15
Absolute temperature (T)	300 K

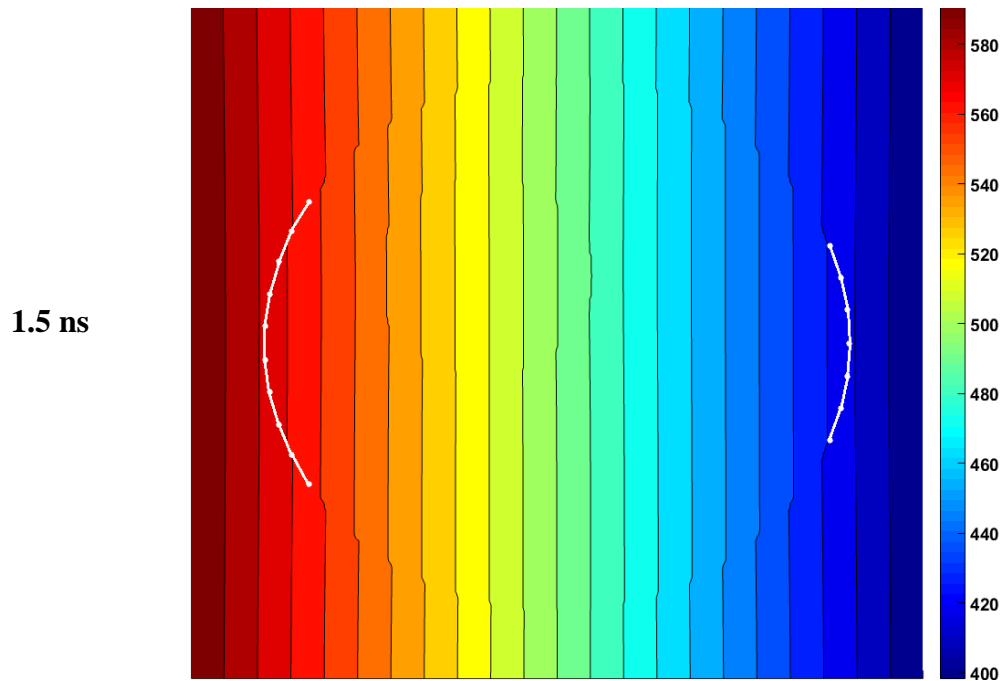
2.3. Results

Presented below are the simulation results for a cell exposed to a single 10-ns, 10 MV/m trapezoidal pulse with 1.5 ns rise- and fall-times. The same pulse was used in [93] and the results obtained from our simulations were compared to the ones reported by Smith (2006) [93]. All types of cell responses (i.e. spatial, angular and temporal) presented by Smith (2006) [93] were plotted in this chapter to validate the accuracy of the modeling results, and give a complete explanation of the cell response to the applied E-field.

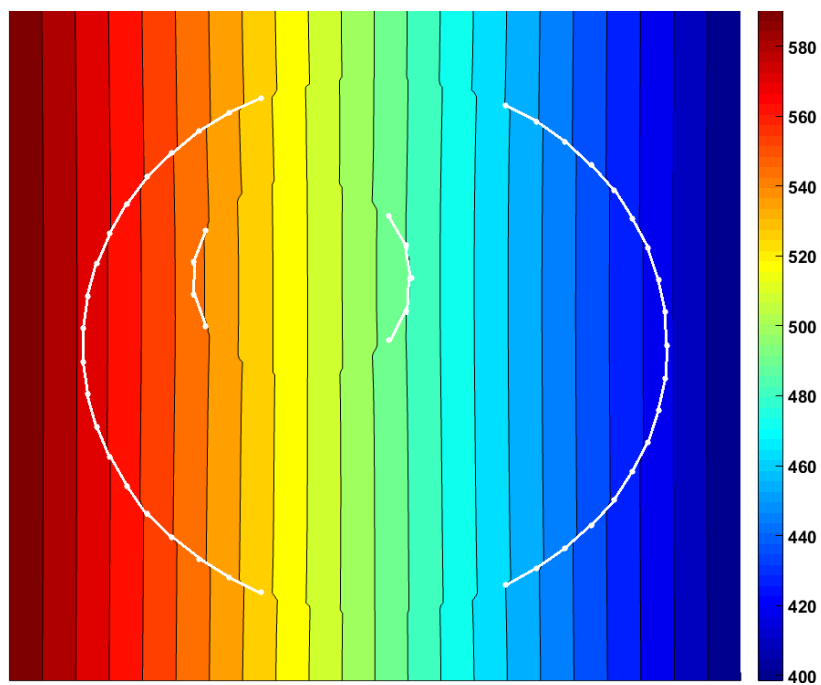
2.3.1 Spatial response

When the pulse is applied, the cell membrane begins to charge (Fig. 2.7; 1.5 ns). Because of the high frequency content of the pulse during the pulse rise-time, the capacitive component of the membrane dominates. The TMP on the cell and nuclear membranes rapidly increases, starting from the polar regions, where it is the highest, and decreases as it approaches the equatorial regions. Pores form when the TMP reaches a critical value of $\sim 1\text{V}$, corresponding to the threshold for reversible electrical breakdown (REB)

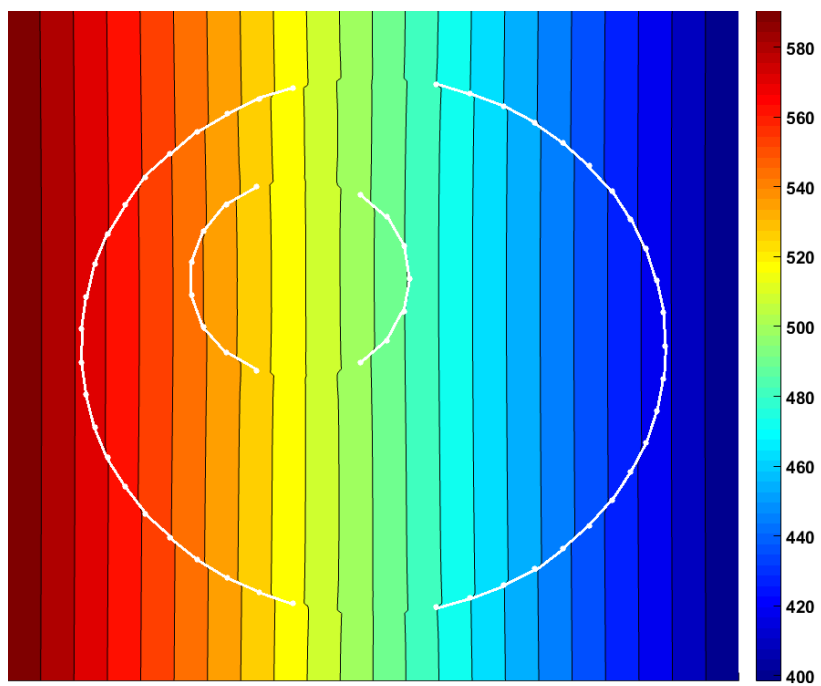
[2,27,28,30]. The TMP and pore density keep increasing away from the poles during the remainder of the pulse, electroporating increasing regions in the cell and nuclear membranes (Fig. 2.7; 3.6 ns) until the end of the pulse plateau (Fig. 2.7; 8.5 ns) where all pores have formed in large regions of both membranes. During the pulse fall-time, the TMP decreases and all the membranes rapidly discharge following pulse application (Fig. 2.7; 1 μ s). The pore density decreases exponentially with a time constant τ of 1.5 s ($\tau = N_0/\alpha$ [93]) corresponding to the pore lifetime, and the cell resting potential ($V_{\text{rest}} = -86$ mV) is reestablished after 30 s, once all the pores in the plasma membrane have closed (Fig. 2.7; 30 s). These results are in agreement with those reported by Smith (2006) [93].



3.6 ns



8.5 ns



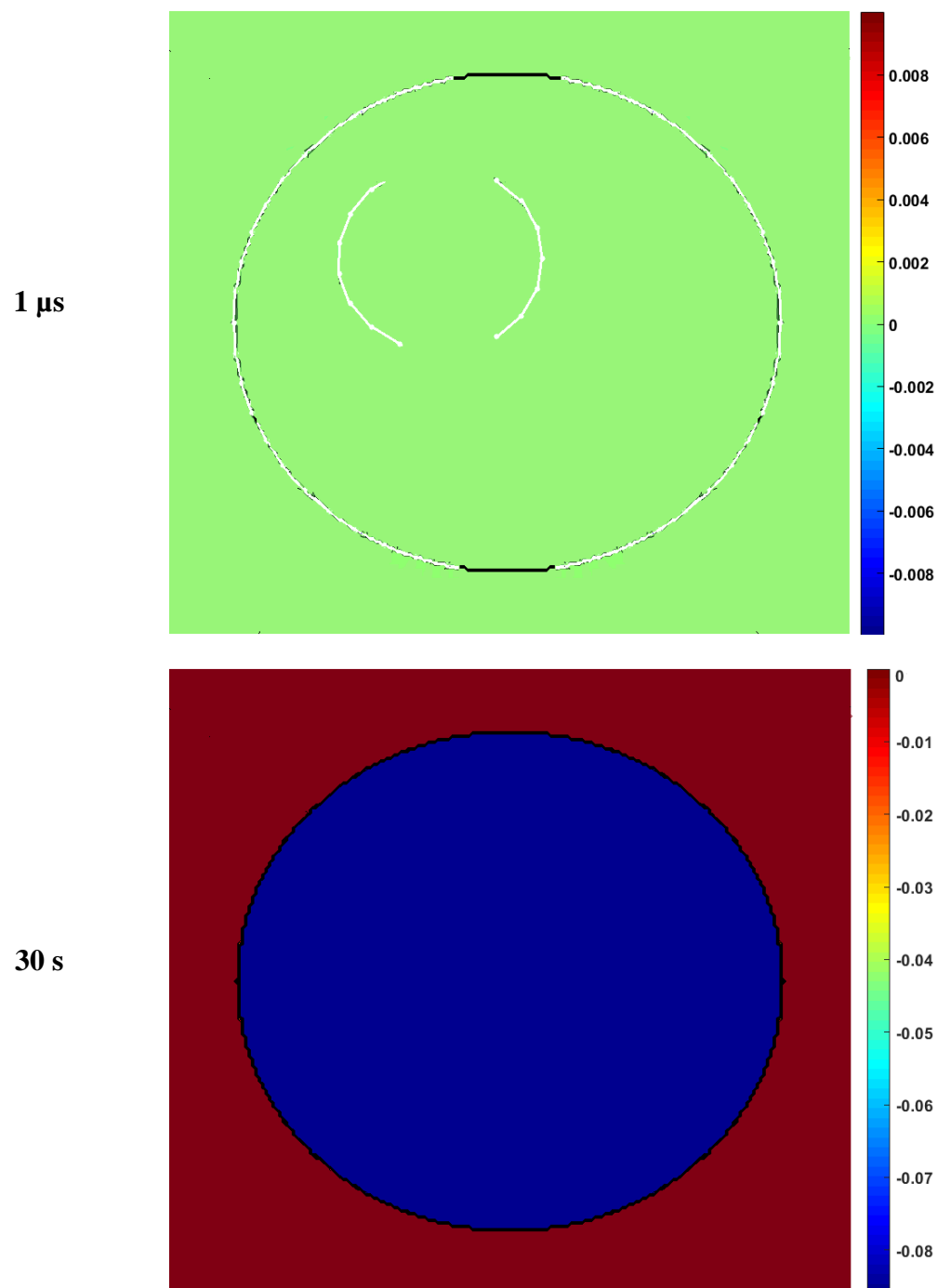


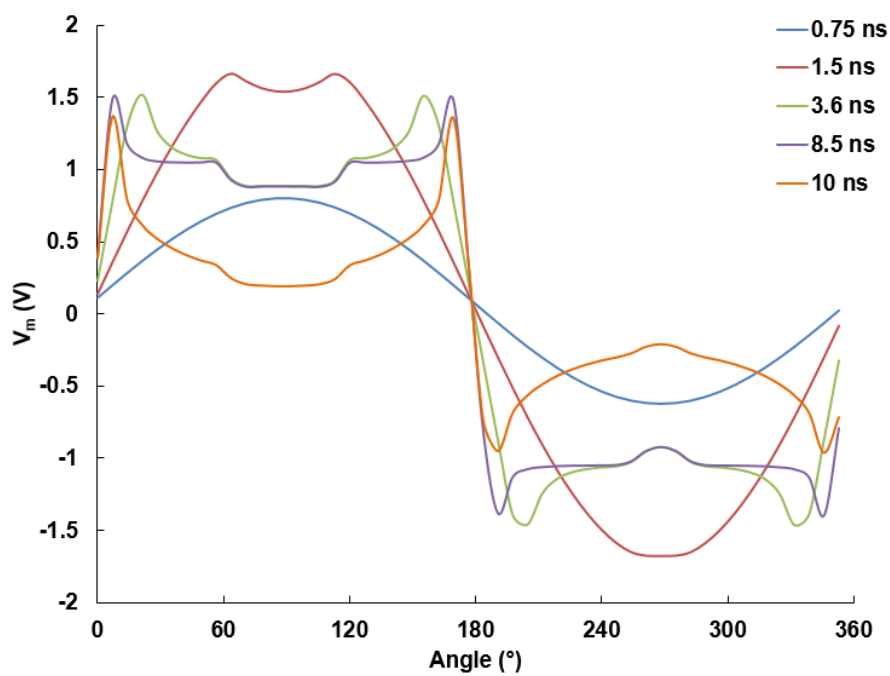
Fig. 2.7. Spatial distribution of the electric potential and pore density at different time points during (1.5, 3.6 and 8.5 ns) and after (1 μs, 30 s) pulse application. The white regions represent a pore density greater than 10^{14} m^{-2} , representing regions with significant electroporation [93]. The color bar represents the electric potential in Volts (V).

2.3.2 Angular response

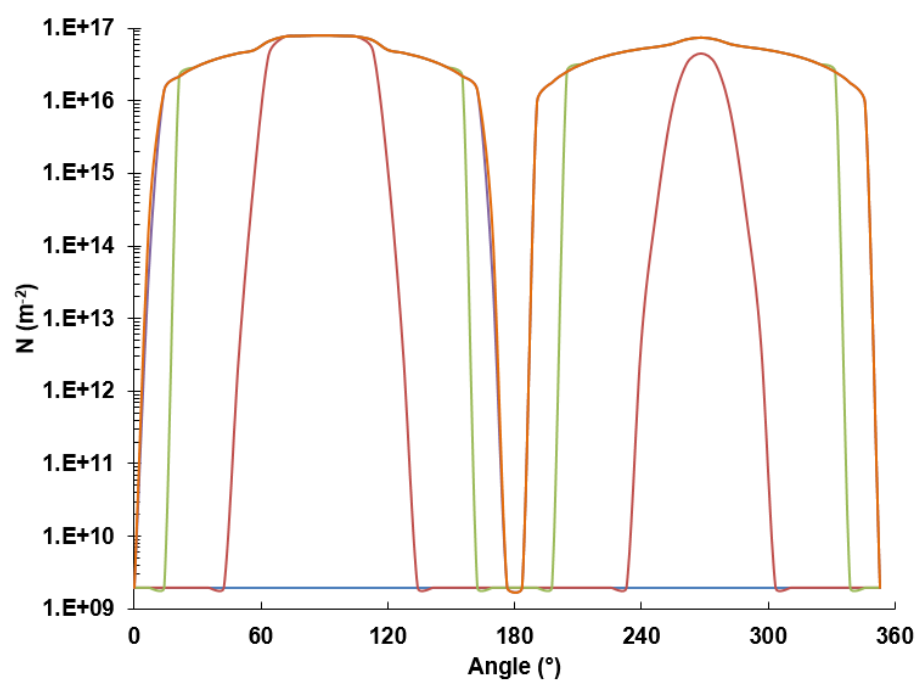
Fig. 2.8 shows the angular response of the TMP (Figs. 2.8a and 2.8c) and the corresponding pore density N (Fig. 2.8b and 2.8d) at different time points during and after pulse application. In this section, the polar angle θ was designated to each membrane such that the anodic side of the membrane corresponded to $\theta = 0$. In this way, the anodic and cathodic poles of the membranes corresponded to $\theta = 90^\circ$ and $\theta = 270^\circ$, respectively.

During the pulse, the TMP has a cosine shape initially (Fig. 2.8a; 0.75 ns). However, as the pulse evolves and the TMP reaches and exceeds ~ 1 V, pores start to form in the polar regions of the cell, starting from the anodic pole ($\theta = 90^\circ$) at 1.4 ns and slightly later (1.5 ns) at the cathodic pole ($\theta = 270^\circ$) (Fig. 2.8b). The slight asymmetry that exists between the anodic and cathodic poles is due to the cell resting potential ($V_{\text{rest}} = -86$ mV). Briefly, when the pulse is applied, the TMP on the membrane increases. Since $V_{\text{rest}} \neq 0$ mV, it superimposes onto the TMP causing a slightly higher TMP at the anodic pole of the cell (where V_{rest} and the E-field have the same direction) compared to that on the cathodic pole (where V_{rest} and the E-field have opposite directions) (see Fig. 2.2).

Pore formation causes the conductance of the membrane to increase. Such an increase in membrane conductance reduces the voltage drop across the membrane, decreasing the TMP to ~ 1 V. The TMP diverges from the cosine shape and the dips observed in the peaks represent the areas in the membrane that have been electroplated (Fig. 2.8a). Towards the end of the pulse, a large region of the membrane is electroplated. Following pulse application, the membrane discharges and the TMP reaches 0 V by 1 μ s. The cell resting potential is reestablished after 30 s (Fig. 2.8c), after all the pores have closed (Fig. 2.8d). These results are in agreement with those reported by Smith (2006) [93].



(a)



(b)

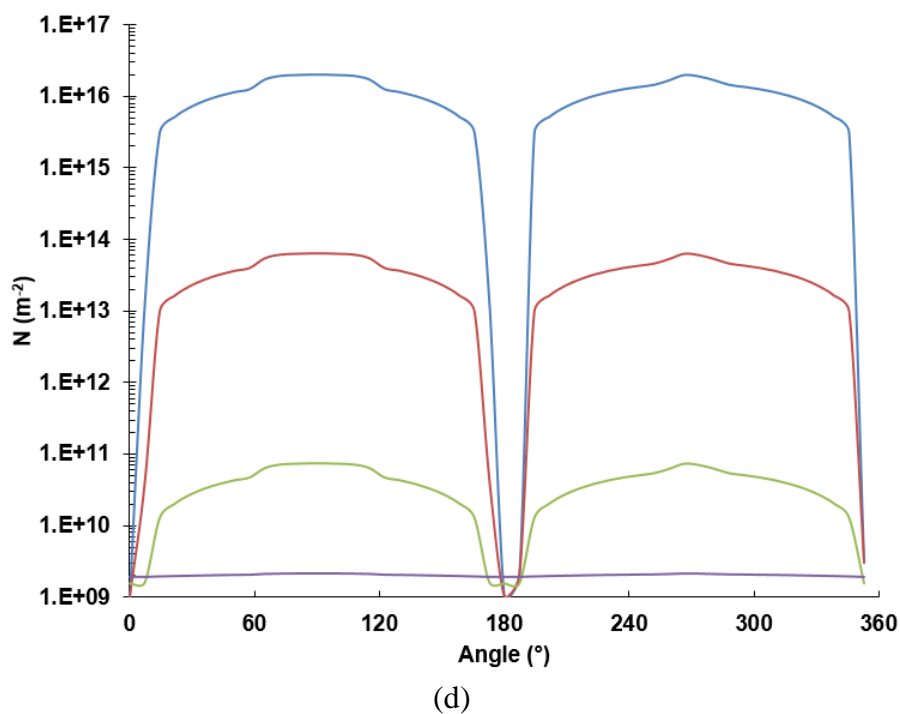
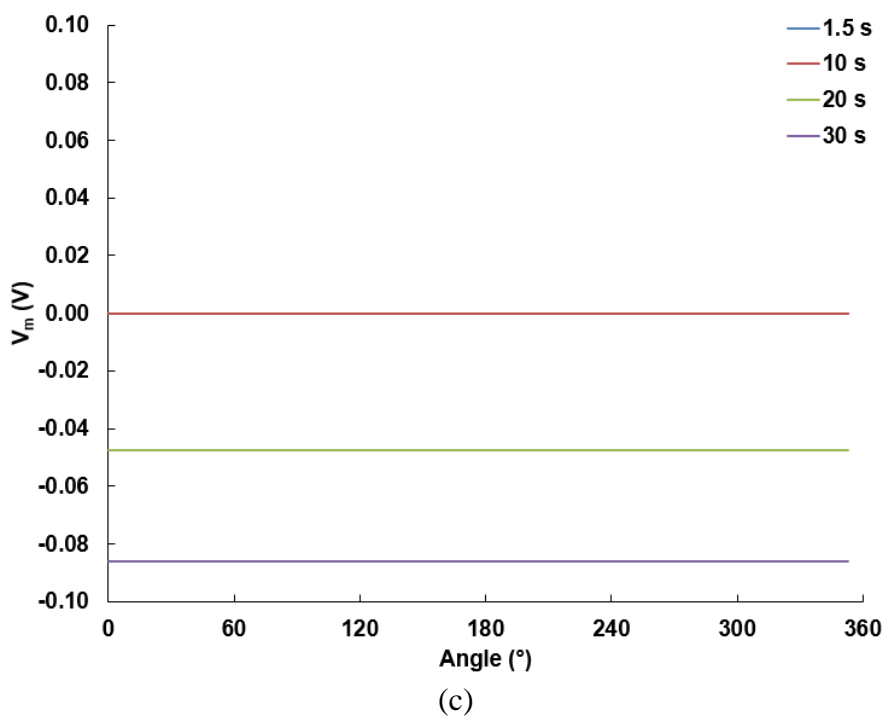


Fig. 2.8. Angular response of the TMP and pore density on the plasma membrane during and after pulse application. (a) and (b) TMP and pore density during the pulse. (c) and (d) TMP and pore density after the pulse.

The same angular behavior is observed in the nuclear membrane. Briefly, during the pulse, initially the TMP has a cosine shape, increasing in amplitude up to 1.5 ns (Fig. 2.9a). As the pulse evolves, when the E-field inside the cell becomes high enough, the TMP on the nuclear membrane reaches ~ 1 V and pores start to form in the polar regions of the nuclear membrane (Fig. 2.9b). The TMP deviates from the cosine shape and the dips observed in the peaks represent the areas that have been electroporated. When the pulse ends, the TMP goes back to 0 V within 1 μ s and pores close with a time constant of 1.5 s. These results are in agreement with those reported by Smith (2006) [93].

2.3.3 Temporal response

The temporal response of the TMP at the anodic and cathodic poles of the cell and nuclear membranes is shown in Fig. 2.10. During the pulse, the TMP increases on both membranes. The anodic pole of the cell membrane electroporates first (1.4 ns) followed by the cathodic pole of the cell (1.5 ns) followed by the poles of the nuclear membrane (2.7 ns). The anodic and cathodic poles of the plasma membrane reach a maximum TMP of 1.673 and 1.670 V, respectively, while the anodic and cathodic poles of the nuclear membrane reach a maximum TMP of 1.665 V. Pore formation in both membranes causes the conductance of the membranes to increase dramatically, and limits the TMP from increasing further, driving it down toward ~ 1 V. After the pulse, all the membranes discharge and the TMPs reach 0 V by 1 μ s. The cell resting potential ($V_{\text{rest}} = -86$ mV) is reestablished after 30 s (Fig. 2.11a), after all the pores in the plasma membrane have closed (Fig. 2.11b). These results are in agreement with those reported by Smith (2006) [93].

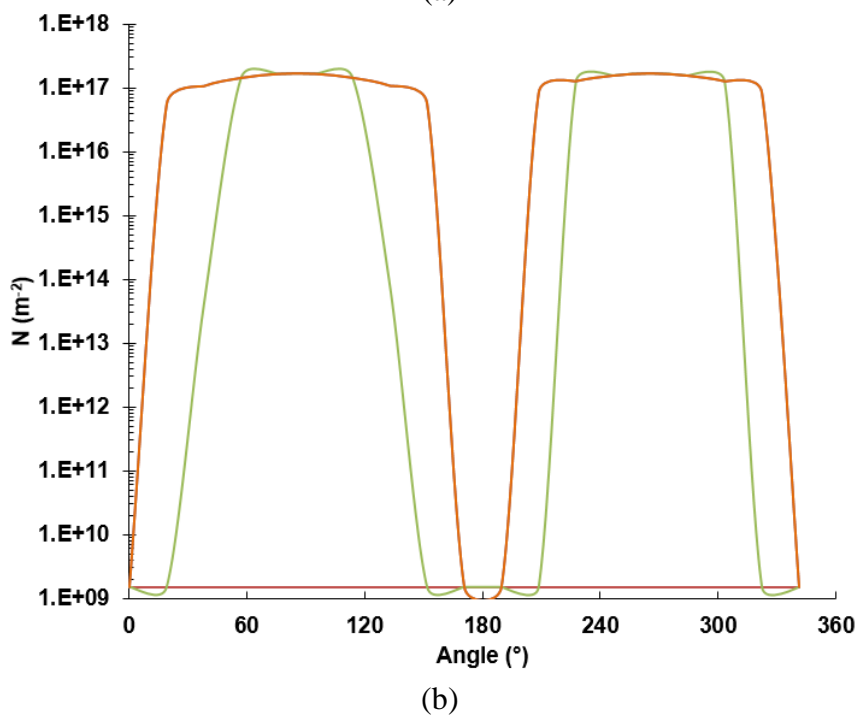
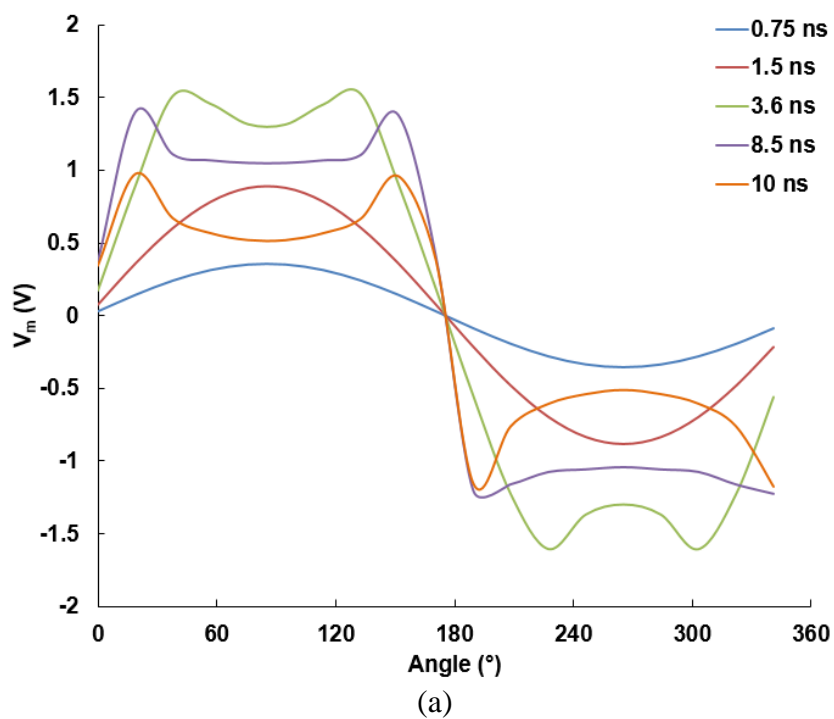


Fig. 2.9. Angular response of the TMP and pore density on the nuclear membrane during and after pulse application. (a) TMP during and after the pulse. (b) Pore density during and after the pulse.

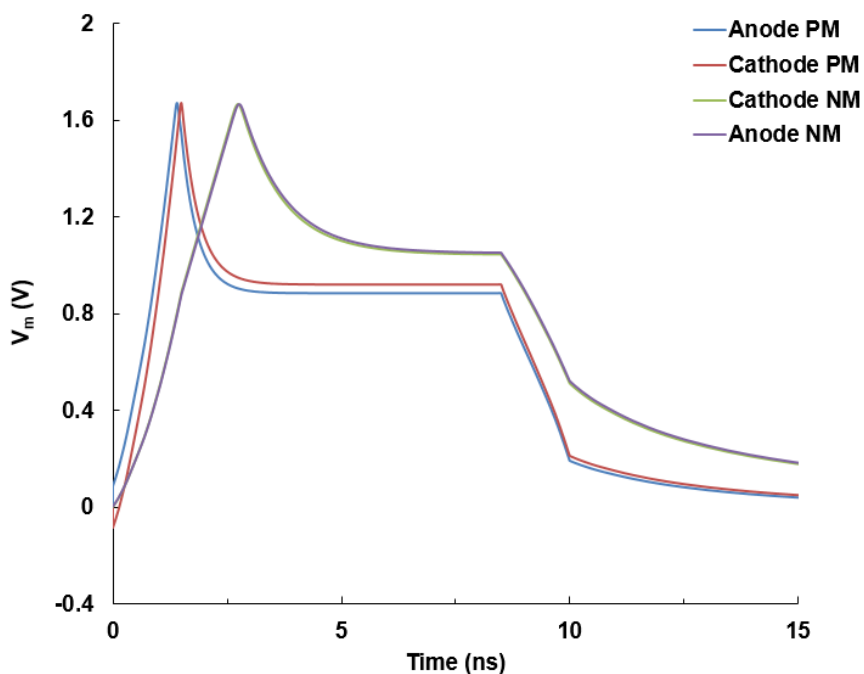
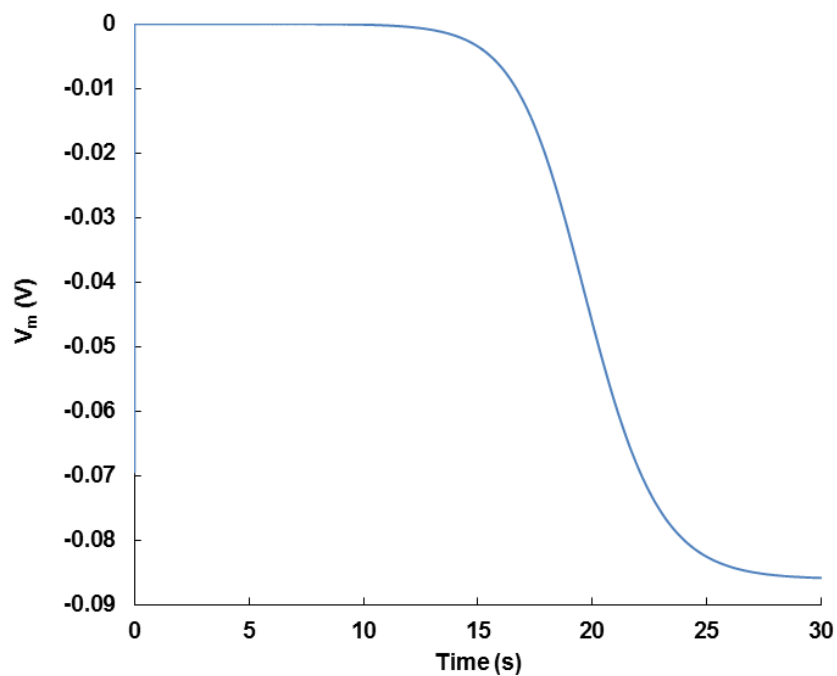


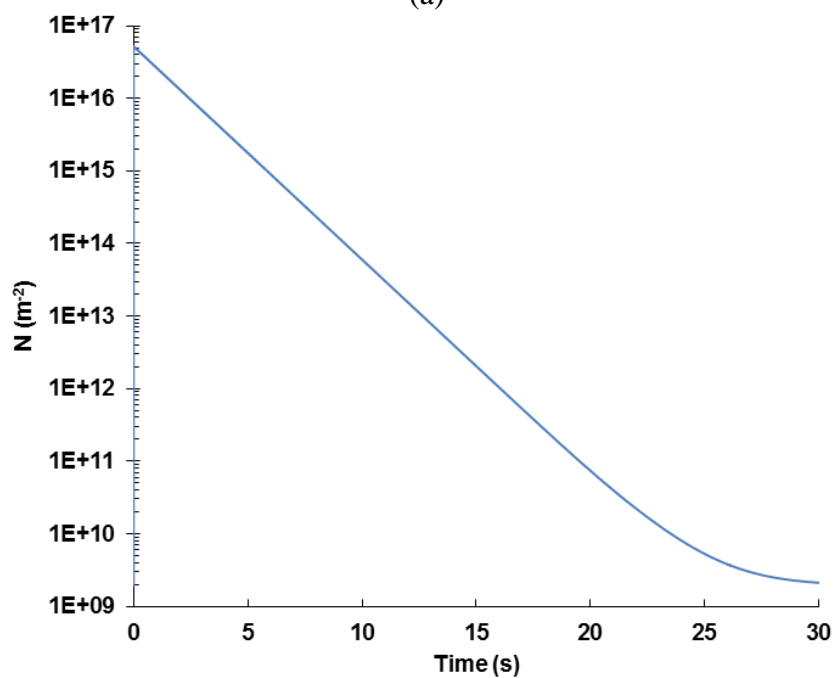
Fig. 2.10. Temporal response of the TMP at the poles of the plasma and nuclear membranes (PM and NM, respectively).

2.4. Review of the electrical properties of cells

Accurate knowledge of the dielectric properties of the constituents of a specific type of cell is critical for correlating the numerical modeling and experimental results. An extensive literature search was conducted in order to determine what data existed for dielectric properties of cells and organelles and how the parameters differ between cell types. The results of the literature survey are summarized in Tables 2.3, 2.4 and 2.5.



(a)



(b)

Fig. 2.11. Temporal response of the TMP and pore density at the anodic pole of the cell membrane following pulse application. (a) TMP at the anodic pole. (b) Pore density at the anodic pole. Similar behavior was also observed at the cathodic pole of the membrane.

In this dissertation, a 2D cell model of an adrenal chromaffin cell is constructed in the following chapters. To our knowledge, there have been no measurements performed on the dielectric properties of these cells. Therefore, a collaboration with Prof. Michael Stacey (Frank Reidy Research Center for Bioelectrics, Old Dominion University, Norfolk, VA, USA) and Dr. Ahmet Can Sabuncu (Department of Mechanical Engineering, Southern Methodist University, Dallas, TX, USA) was formed to measure the dielectric properties of chromaffin cells (manuscript in preparation). The technique adopted to determine these properties is “microfluidic impedance spectroscopy” in which a microfluidic device containing a cell suspension is used to perform dielectric spectroscopy measurements [97]. Details of the method as well as the fabrication of the microfluidic chamber used to perform the measurements can be found in [97]. Briefly, the impedance spectrum (recorded for frequencies ranging from 1 kHz to 20 MHz) of a chromaffin cell suspension is measured using a microfluidic chamber connected to a precision impedance analyzer via a BNC port. Cell complex permittivity is derived from impedance data by: 1) fitting the cell dielectric spectrum into a Maxwell-Wagner mixture model, 2) obtaining the Clausius-Mossotti factor, which is a function of the cell complex permittivity, and 3) calculating the cell complex permittivity using this factor and a double shell model. Details of these steps can be found in [97].

Extraction of the dielectric properties of subcellular structures requires the use of a vesicular cell model, originally used by Raicu et al. (1998) for modeling hepatocytes [98]. This model is chosen for chromaffin cells because of the large number of secretory granules that are present in their cytoplasm [88]. Using a combination of the measured impedance data and the vesicular cell model, some dielectric properties proper to chromaffin cells such

as the cytoplasm conductivity, secretory granule membrane permittivity and interior conductivity are extracted using a fitting algorithm that minimizes the residuals between the model and experimental data [97]. These measured parameters are found in Table 2.6.

Table 2.3: Summary of the electrical properties of cells [97,99-104].

Cell type	σ_{cyto} (S m^{-1}) ^a	C_{memb} (mF m^{-2}) ^b	ϵ_{memb} ^c	$\sigma_{\text{memb}} \times 10^{-6}$ (S m^{-1}) ^d
Red blood cell	0.52 ± 0.051	9 ± 0.8		
T-lymphocyte	0.65 ± 0.15	10.5 ± 3.1		
B-lymphocyte	0.73 ± 0.18	12.6 ± 3.5		
Monocyte	0.56 ± 0.10	15.3 ± 4.3		
Granulocyte	0.60 ± 0.13	11 ± 3.2		
K562	0.30 ± 0.02	9.7 ± 0.9		
MDA-231	0.62 ± 0.073	25.9 ± 3.7		
MCF-7	0.23 ± 0.01	12.4 ± 1.8		
MCF-7TaxR	0.14 ± 0.40	20.6 ± 1.1		
MCF-7DoxR	0.40 ± 0.02	12.4 ± 0.9		
MCF-7MDR1	0.27 ± 0.31	12.6 ± 0.7		
H357	0.31 ± 0.02	18.9 ± 2.5		
UP	0.45 ± 0.05	11.4 ± 0.6		
786-O	0.47 ± 0.09	36.7 ± 10.0		
T2	0.55 ± 0.14	45.3 ± 15.1		
L5178Y	1.1 ± 0.02	9.8 ± 0.2	8.82 ± 0.19	0.08
Jurkat	0.32 ± 0.002	12.2 ± 1.1		
<u>B-cells</u>				
B-normal	1.31 ± 0.08		12.8 ± 1.6	56 ± 29
Magala	0.55 ± 0.2		11.4 ± 2.4	8.8 ± 0.7
Raji	0.58 ± 0.02		8.8 ± 1.1	8.2 ± 0.6
Bjab	0.88 ± 0.11		8.0 ± 0.7	11.0 ± 5.3
Daudi	0.85 ± 0.09		7.2 ± 0.7	9.5 ± 1.4
<u>T-cells</u>				
T-normal	0.65 ± 0.13		11.1 ± 1.4	27.4 ± 6.2
Peer	0.81 ± 0.09		9.5 ± 0.7	12.9 ± 3.6
HDMAR	0.88 ± 0.25		7.4 ± 1.2	14.5 ± 4

^a Cytoplasmic conductivity

^b Cell membrane specific capacitance

^c Cell membrane relative permittivity

^d Cell membrane conductivity

Table 2.4: Summary of the electrical properties of nuclei [97,101,102].

Cell type	σ_{ne} (mS m ⁻¹) ^a	σ_{np} (S m ⁻¹) ^b	ϵ_{ne} ^c	C_{ne} (μ F cm ⁻²) ^d
L5178Y	7.0 ± 2.0	0.8 ± 0.04	19 ± 2	
Jurkat		0.63 ± 0.005		1.57 ± 0.01
<u>B-cells</u>				
B-normal	11.1 ± 7.2	2.04 ± 0.29	106 ± 35	
Magala	3.7 ± 0.9	1.08 ± 0.03	72.5 ± 11.6	
Raji	4.0 ± 1.6	1.02 ± 0.25	79.9 ± 34.4	
Bjab	2.1 ± 0.7	1.39 ± 0.54	108 ± 35	
Daudi	2.7 ± 0.3	1.44 ± 0.35	66.1 ± 7.5	
<u>T-cells</u>				
T-normal	8.8 ± 0.6	1.26 ± 0.27	85.6 ± 16.7	
Peer	2.1 ± 0.6	1.42 ± 0.2	61.6 ± 17	
HDMAR	3.0 ± 0.2	1.58 ± 0.28	101.2 ± 55.3	

^a Nuclear membrane conductivity^b Nucleoplasmic conductivity^c Nuclear membrane permittivity^d Nuclear membrane specific capacitance

Table 2.5: Summary of the electrical properties of mitochondria [105,106].

Cell type	σ_i (mS cm ⁻¹) ^a	C_{mito} (μ F cm ⁻²) ^b
Rat liver	1.1-10.0	0.5-0.6
Guinea pig heart	0.5-7.6	1.1-1.3

^a Mitochondrial internal conductivity^b Mitochondrial membrane specific capacitance

Table 2.6: Measured dielectric properties of chromaffin cells.

C_{memb} (μ F cm ⁻²)	σ_{cyto} (S m ⁻¹) ^a	$C_{gran-memb}$ (μ F cm ⁻²) ^b	$\sigma_{gran-int}$ (S m ⁻¹) ^c
1.28 ± 0.18	1.31 ± 0.31	5.54 ± 2.26	0.32 ± 0.1

^a Cytoplasmic conductivity (excluding the granules)^b Granule membrane specific capacitance^c Granule interior conductivity

2.5. Conclusions

In this chapter, the construction and simulation of a 2D cell model exposed to a single NEP were described and the results were validated against those reported by Smith (2006) [93]. The spatial, angular and temporal cell responses obtained from this model were very similar (maximum error on the TMP was less than 0.01%) to the ones obtained by Smith (2006) using a model with 600 membrane node pairs. These results indicated that the Matlab code written is valid, and that the model constructed with a smaller number of nodes in the cell membrane (51 membrane node pairs) is accurate.

Because of the limited capacity of the computers available in our laboratory, the model with 51 membrane node pairs described in this chapter was constructed in order to be able to run simulations up to a time period of 30 s. In the following chapters of this dissertation, models with multiple structures were constructed using similar Matlab codes that were modified to create the needed geometry to study the NEP-induced effects on the cell and/or its intracellular organelles. The number of cell membrane node pairs (Chapter 3) was increased up to 296 nodes, the highest achievable with the computer resources available in our laboratory. However, simulations using those models were run only for 1 μ s. Even though it was not possible to fully track what happened at times after 1 μ s (i.e., up to 30 s), the data obtained from the 1 μ s simulations were sufficient to accurately interpret the model results and compare them to the experimental observations.

The variation in the properties observed across cell types shows the importance of knowing accurately the parameters for a specific type of cell. In the following chapters, emphasis will be placed on some of these parameters (e.g. σ_{cyto}) that were implemented in the models and had a significant effect on the interpretation of the simulation results.

CHAPTER 3. Exposing Adrenal Chromaffin Cells to 5-ns Electric Pulses Requires Higher Electric Fields to Porate Intracellular Membranes than for Porating the Plasma Membrane

3.1. Introduction

High intensity, nanosecond-duration electric pulses (NEPs) permeabilize the plasma membrane as well as membranes of intracellular organelles, the latter causing Ca^{2+} release from internal stores. This chapter describes the results obtained experimentally in isolated adrenal chromaffin cells in which the E-field thresholds for a 5-6 ns duration pulse to cause plasma membrane permeabilization versus poration of intracellular membranes were established. The experimental approaches that were used include monitoring whole-cell currents in patch-clamped* cells to assess plasma membrane permeabilization and fluorescence microscopy to assess release of Ca^{2+} from internal stores. This chapter also describes how a 2D cell model was constructed and the results used to understand the high E-field requirement for porating intracellular membranes.

* Patch clamp experiments were performed by Dr. Lisha Yang, Department of Pharmacology, University of Nevada Reno, and the results were used in this dissertation to complement the results obtained from fluorescence imaging of Ca^{2+} .

3.2. Materials and methods

3.2.1 Chromaffin cell isolation, culturing and dissociation

Bovine chromaffin cells were isolated from the medulla of fresh adrenal glands using the method described by Waymire et al. (1993) [107]. Briefly, fresh adrenal glands were obtained from a local abattoir (Wolf Pack Meats, Reno, NV, USA). The outer cortex was removed by dissection and a perfusion catheter inserted in the adreno-lumbar vein of the medulla. To flush out red blood cells, the tissue was perfused with a $\text{Ca}^{2+}/\text{Mg}^{2+}$ -free Hank's balanced salt solution (HBSS) of the following composition: 137 mM NaCl, 5.37 mM KCl, 0.44 mM KH_2PO_4 , 0.54 mM Na_2HPO_4 , 4.17 mM NaHCO_3 , 5.55 mM D-Glucose, 5 mM HEPES, phenol red (0.001%) and 0.02% bovine serum albumin (BSA), pH 7.2. The medulla was then digested by perfusing it via the adreno-lumbar vein with HBSS containing collagenase B (0.05%) and CaCl_2 (50 μM). Once digestion was complete, the swollen tissue was gently agitated to obtain single cells, which were subjected to a sequence of four centrifugation steps to remove debris and any remaining red blood cells. After the final centrifugation step, the cells were diluted to a final concentration of 4×10^5 cells/ml in Ham's F-12 medium supplemented with 10 % bovine calf serum, 100 U/ml penicillin, 100 $\mu\text{g}/\text{ml}$ streptomycin, 0.25 $\mu\text{g}/\text{ml}$ fungizone, and 6 $\mu\text{g}/\text{ml}$ cytosine arabinoside, placed into tissue culture flasks and incubated for 5.5 hours at 36.5°C under a humidified atmosphere of 5% CO_2 . During this incubation, non-chromaffin cells present in the cell mixture adhered to the bottom of the tissue culture flask whereas the chromaffin cells remained in suspension. At the end of the differential plating step, the cells were collected from each flask, distributed into 60 mm Petri dishes at a density of 1×10^5 cells/ml

and maintained in suspension culture in the supplemented Hams' F12 medium at 36.5°C under a humidified atmosphere of 5% CO₂. Cells were used up until 3 weeks in culture.

For all experiments, the large aggregates of cells that form in suspension culture were dissociated into single isolated cells with the protease dispase [108]. Briefly, the enzyme was added directly to a dish of cells for a minimum of 6 hours. After collecting the cells by centrifugation, cells were incubated at 37°C in Ca²⁺/Mg²⁺-free HBSS lacking KH₂PO₄, NaHCO₃ and phenol red. After 10 min, the incubation was interrupted and the cells were gently triturated to facilitate dissociation. The incubation/trituration steps were repeated 4 times. Once cell aggregates were fully dissociated, the cells were plated onto either fibronectin-coated 35 mm glass bottom dishes (inner glass diameter: 20 mm for fluorescence imaging) or into fibronectin-coated glass coverslips (for patch clamp). Cells were used for a period not exceeding 2 days after attachment.

3.2.2 Fluorescence imaging of intracellular Ca²⁺ levels

Cells were incubated with a cell permeant Ca²⁺-sensitive fluorescent indicator Calcium Green-1-AM (1 μM; 480/535 nm) for 45 min at 37°C in a balanced salt solution (BSS) with the following composition: 145 mM NaCl, 5 mM KCl, 1.2 mM NaH₂PO₄, 2 mM CaCl₂, 1.3 mM MgCl₂, 10 mM glucose, 15 mM HEPES and 0.1% BSA, pH 7.4. After incubation, cells were washed twice with dye-free BSS lacking BSA and placed on the stage of a Nikon TE2000 epifluorescence microscope equipped with a 100X objective. For experiments conducted in the absence of extracellular Ca²⁺, the BSS lacked Ca²⁺ and contained 1 mM EGTA. Fluorescence images of the cells, which were obtained before, during and after stimulus application, were captured by an iXonEM + DU-897 EMCCD

camera (Andor Technology Ltd., Belfast, UK) using the open source microscopy software Micro-Manager (version 1.4). The exposure time of the camera was set to 10 ms for the receptor agonist stimulation experiments, and was increased to 100 ms for the NEP stimulation experiments to reduce the noise in the signal. Continuous baseline Ca^{2+} fluorescence of the cells was monitored 10 s prior to stimulus application and continued for 20-30 s after the stimulus. Sequences were analyzed using the public-domain image processing program ImageJ. The change in fluorescence intensity (ΔF) of the cells was calculated by subtracting the background fluorescence from the fluorescence of the cell ($\Delta F = F_{\text{cell}} - F_{\text{background}}$). ΔF was then normalized to the fluorescence intensity value (F_0) at the time when the stimulus was applied ($\Delta F/F_0$). Bright field images were obtained before and after the applied stimulus.

In some experiments, cells were stimulated with the mixed nicotinic-muscarinic receptor agonist carbachol that was applied with a pressure ejection Picospritzer^R system. The glass micropipette (tip diameter: 1 μm) that delivered the agonist was positioned at a distance of one cell diameter from the target cell. A program written in LabVIEW (version 9, National Instruments, Austin, TX) triggered the ejection of the agonist, with the duration of the pressure pulse set at 5 ms.

3.2.3 Statistical analysis

For statistical analysis, experiments were repeated at least once using cells from different days in culture and different cell preparations. The normalized Ca^{2+} responses of the cells shown in Figs. 3.8c and 3.11c are represented as mean \pm standard deviation (S.D.).

3.2.4 Whole-cell recording of membrane conductance

A coverslip with attached cells was placed in a cell perfusion chamber positioned on the stage of a Nikon TS-100 inverted epifluorescence microscope (experimental setup shown in Fig. 3.1). Cells were continuously perfused at a rate of 0.5 ml/min with the same BSS used in the fluorescence imaging experiments. Cells were viewed with a 40X objective and bright field images of the cells were captured with a CoolSNAP HQ DIFF CCD camera (Photometrics, Tucson, AZ) and SimplePCI software (version 6.6.0.0, Hamamatsu Corporation, Hamamatsu City, Japan) at the start and end of experiments. The whole-cell variant of the patch clamp technique was used in voltage clamp mode to monitor NEP-evoked changes in membrane conductance*. A complete description of the method is described in [91]. Briefly, a glass micropipette (tip diameter: 1 μm), filled with an internal solution of the following composition: 10 mM NaCl, 30 mM KCl, 110 mM K-gluconate, 1 mM MgCl₂, 10 mM EGTA, 3 mM MgATP, and 10 mM Hepes, pH 7.2, was applied to the cell via a motorized MS-314 micromanipulator (Märzhäuser Wetzlar, Wetzlar, Germany). After rupturing the membrane to achieve the whole-cell recording mode, monitoring was carried out at a holding potential of -70 mV to minimize the probability of voltage-gated channel activation contributing to the observed membrane responses.

* The NEP exposure system for patch clamp experiments was setup by Dr. Jihwan Yoon, Department of Electrical and Biomedical Engineering, University of Nevada Reno, and whole-cell recording experiments were performed by Dr. Lisha Yang, Department of Pharmacology, University of Nevada Reno.

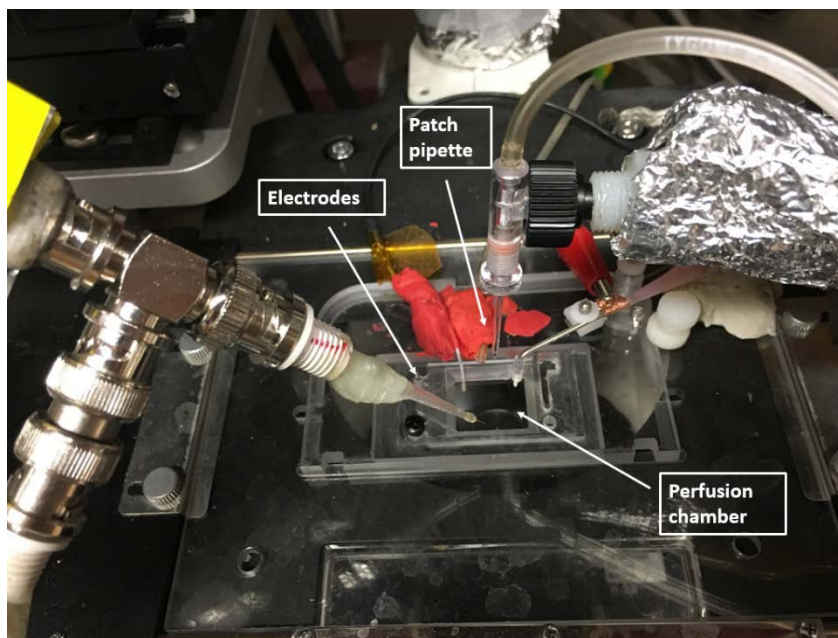


Fig. 3.1. Photograph of the actual experimental setup used for patch clamp whole-cell recording.

3.2.5 NEP exposure

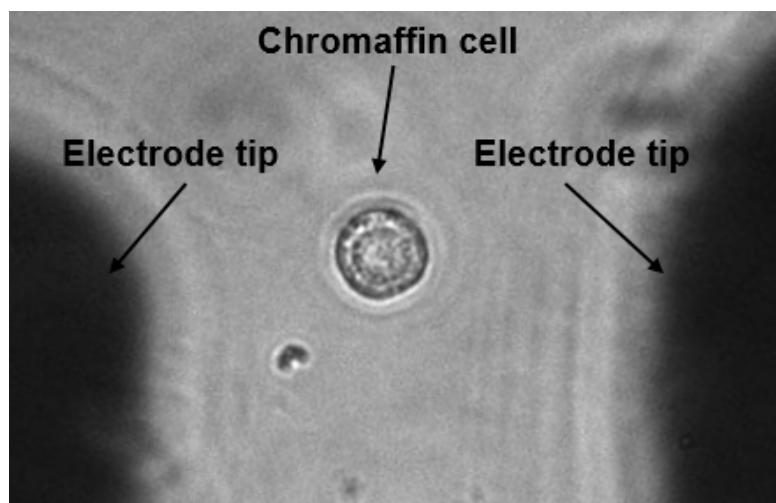
For the fluorescence imaging experiments, a 5-6 ns pulse was applied to a cell by means of two cylindrical gold-plated tungsten rod electrodes (127 μm diameter) spaced 100 μm apart. The tips of the electrodes were immersed in the BSS bathing the cells and placed 40 μm above the bottom of the dish, with the imaged cell located at the center of the gap between the electrode tips (Fig. 3.2a). The entire experimental setup is shown in Fig. 3.2b.

Single pulses with amplitudes that produced electric fields (E-fields) ranging from 2 to 21 MV/m (see the subsection below for the E-field calculation) at the location of the cell were generated by a custom-fabricated nanosecond pulse generator (Transient Plasma Systems, Torrance, CA). Depending on the pulse amplitude, the pulse width varied from 5 to 6 ns, with the shorter durations obtained at the highest E-field amplitudes. Delivery of

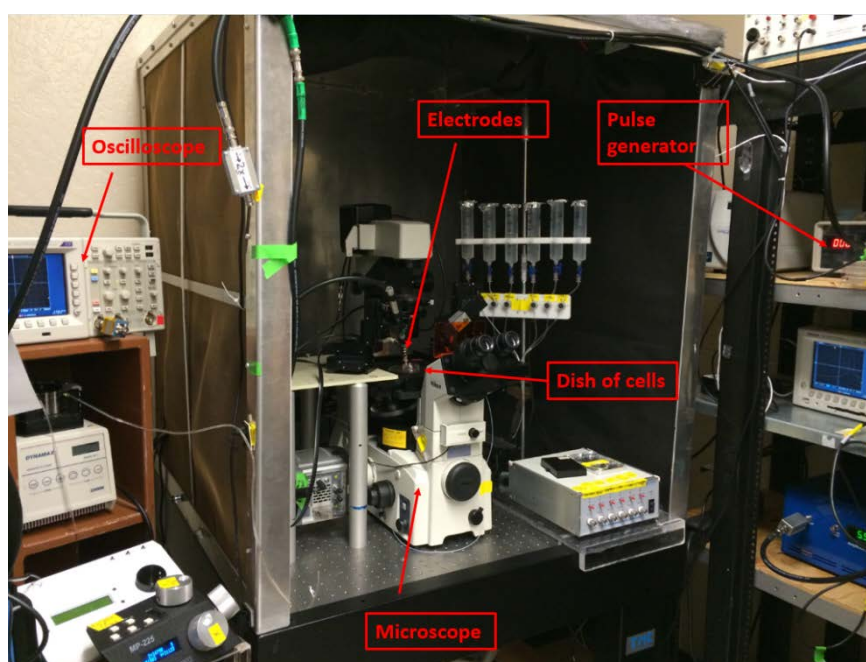
pulses was triggered externally by a program written in LabVIEW, and pulse traces (Fig. 3.2c) captured with a TDS 3102C oscilloscope (Tektronix, Beaverton, OR, USA).

For the patch-clamp experiments, a tungsten-rod electrode system similar to the one used in the fluorescence imaging experiments was used to deliver NEPs to a patch-clamped cell. The electrodes were positioned 40 μm above the bottom of the coverslip on which the cells were attached. Using a motorized MP-225 micromanipulator (Sutter Instruments, Novato, CA), the electrodes were positioned so that the patch-clamped cell was located at the center of the gap between the electrode tips. Single pulses with amplitudes that produced E-fields ranging from 3 to 8 MV/m at the location of the cell were generated by a custom-fabricated nanosecond pulse generator (Transient Plasma Systems, Torrance, CA), similar to the one used in the fluorescence imaging experiments. All experiments included two sham exposures preceding the application of a NEP to ensure that any observed response from the cell was not due to an artifact created by the exposure system. Measurements were made immediately before and 8 ms after NEP exposure using an automated system controlled externally by a program written in LabVIEW [91].

In all experiments (fluorescence imaging and patch clamp), a cell was exposed to the E-field only once.



(a)



(b)

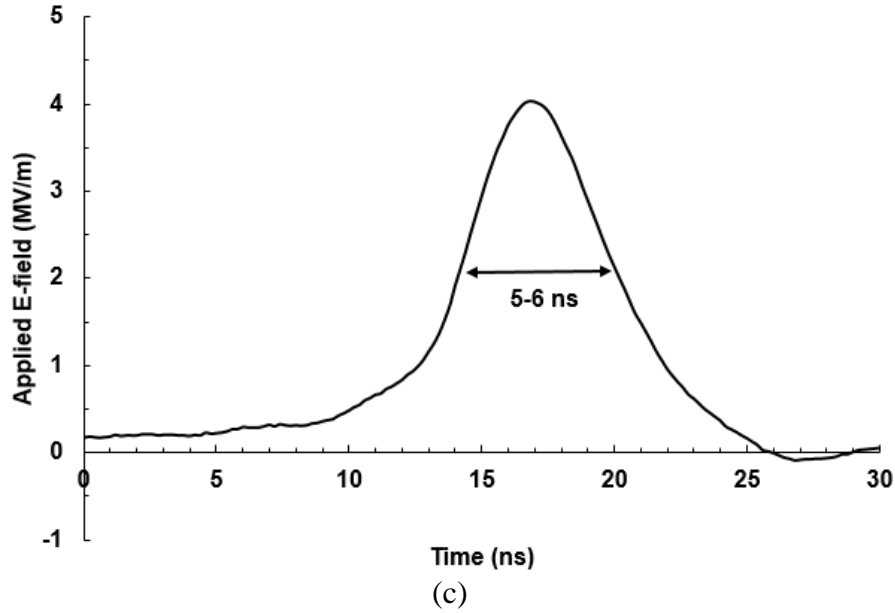


Fig. 3.2. Details of the NEP exposure system. (a) Photomicrograph of an attached cell showing the electrode tips that are positioned $40\ \mu\text{m}$ above the bottom of the dish. (b) Photograph of the actual experimental setup used for the fluorescence imaging experiments. (c) Representative waveform of a 5-6 ns pulse applied in experiments to chromaffin cells. The pulse duration corresponds to the width at half maximum.

3.2.1.1. *Numerical computation of the E-field distribution in the vicinity and at the location of the cell*

The E-field distribution in the vicinity and at the location of the cell was computed* using the commercially available Finite-Difference Time-Domain software package SEMCAD X (version 14.8.5, SPEAG, Zurich, Switzerland). Briefly, experimental voltage trace data, recorded on an oscilloscope, were collected from several NEP traces, averaged together and then used as input excitation in SEMCAD X to compute the E-field distribution as follows.

* SEMCAD X simulations were performed by Dr. Jihwan Yoon and Robert Terhune, Department of Electrical and Biomedical Engineering, University of Nevada Reno, and the results were used in this dissertation to calculate the E-field amplitudes applied to cell during experiments.

A three-dimensional (3D) geometric model was created in SEMCAD X to represent the portion of the exposure system that included the exposed ends of the electrode tips, the $50\ \Omega$ matching resistance (matching the characteristic impedance of the electrodes to that of the cables and pulse delivery system), the BSS, and the glass chamber representing the glass bottom dish onto which the cells are attached (Fig. 3.3a). The entire exposure system was not modeled because of computational limitations. The electrode tips were positioned $40\ \mu\text{m}$ above the chamber floor and were surrounded by BSS, as in actual experiments.

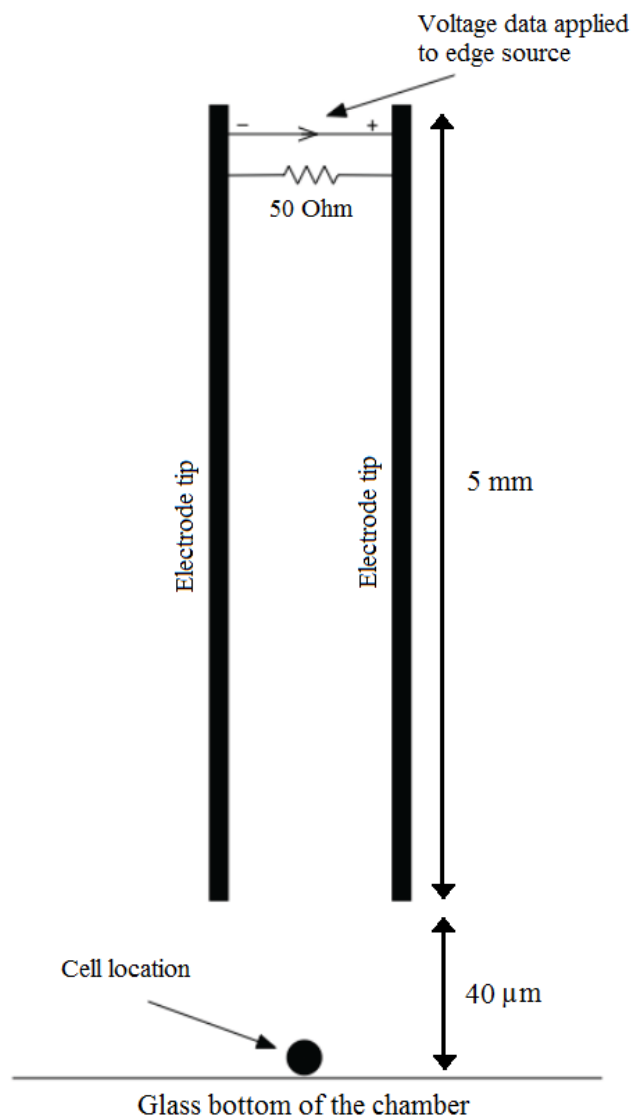
A SEMCAD simulation was then performed wherein the averaged voltage data of the pulse was fed to the edge source which supplies the pulse, located at the top of the electrodes as shown in Fig. 3.3a. The E-field at the location of the cell (Fig. 3.3b) was computed and detected by a point sensor placed at the cell location.

A conversion factor was obtained by dividing the peak E-field detected by the point sensor by the peak voltage applied to the edge source. This conversion factor was used to calculate the E-field amplitude delivered to the cells, by multiplying the peak voltage measured via the oscilloscope during experiments by the conversion factor obtained from the simulations.

3.2.6 Reagents

Calcium Green-1-AM was purchased from Molecular Probes (Eugene, OR, USA), Ham's F-12, dispase II and the antibiotic-antimycotic were purchased from Gibco Laboratories (Grand Island, NY, USA), bovine calf serum was purchased from Gemini Bio-products (West Sacramento, CA, USA), and collagenase B was purchased from Roche

Diagnostics (Indianapolis, IN, USA). All other chemicals and reagents were reagent grade and purchased from standard commercial sources.



(a)

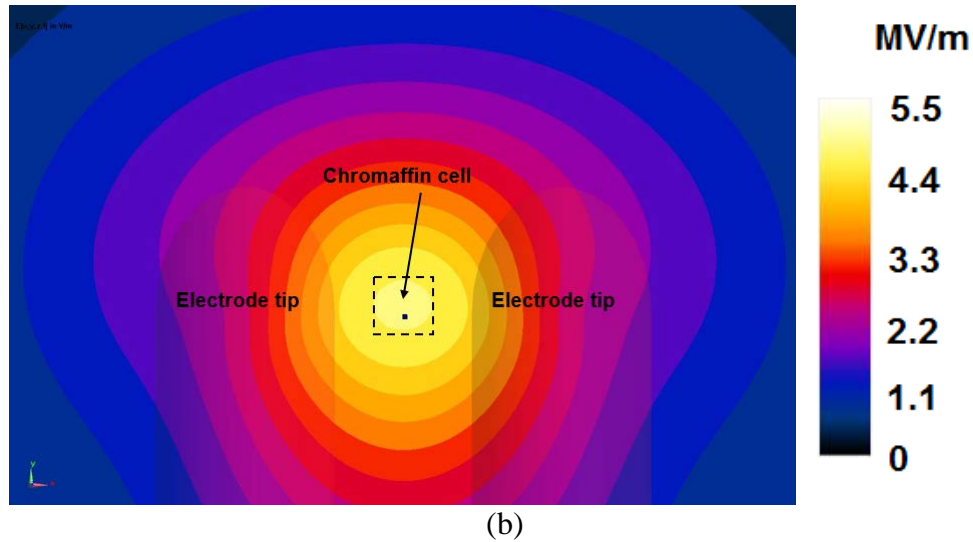


Fig. 3.3. Details of the FDTD simulations. (a) Schematic showing the geometry used in the FDTD simulations. The point sensor used to detect the E-field computed in the simulations is placed at the cell location. (b) E-field distribution in the vicinity and at the location of the cell when a voltage of 2700 V was applied. The dotted box represents the region over which a cell can be located in experiments.

3.2.7 2D cell modeling

A 2D geometric model of a chromaffin cell exposed to a single 5-6 ns pulse was constructed in Matlab (2015a, Mathworks) based on the meshed transport network method (MTNM) developed by Smith and Weaver (2008) [40]. The electrical response of the cell was based on the asymptotic model of electroporation developed by Neu and Krassowska (1999) [34]. Below is a description of the geometry and parameters used in the model.

3.2.7.1 Cell system geometry

The cell system geometry (Fig. 3.4a) consisted of a circle of radius $r_{\text{cell}} = 8 \mu\text{m}$, representative of a chromaffin cell [88], centered inside a bounding box of dimensions $100 \mu\text{m} \times 100 \mu\text{m}$, representing the $100 \mu\text{m}$ gap between the electrodes. The system depth was

calculated by $d = (4/3)r_{\text{cell}} = 10.67 \mu\text{m}$, assuming that the cylindrical cell has the same volume as a spherical cell of the same radius [39].

Four circular structures representing intracellular Ca^{2+} -storing organelles were placed arbitrarily offset from the cell center (Fig. 3.4b) and consisted of: a large structure representing a nucleus of radius $r_{\text{nucl}} = 2.5 \mu\text{m}$ [88], a smaller structure representing a mitochondrion of radius $r_{\text{mito}} = 1 \mu\text{m}$ [93], an ER represented by a structure of radius $r_{\text{ER}} = 500 \text{ nm}$, and a secretory granule represented by a structure of radius $r_{\text{gran}} = 400 \text{ nm}$ [88]. All geometrical parameters are summarized in Table 3.1.

The cell, ER and secretory granule were each assigned a single membrane that had a thickness of $d_m = 5 \text{ nm}$; the nucleus and the mitochondrion were assigned double membranes structures. The two membranes forming the nuclear envelope were assumed identical and the intermembrane space between the nuclear membranes was neglected [109]. Therefore, the transmembrane potential (TMP) across one nuclear membrane was assumed to be half the TMP across the whole nuclear envelope. In this way, the nuclear envelope required twice the TMP to electroporate compared to the single membrane structures. The inner and outer mitochondrial membranes (IMM and OMM, respectively) were separated by a 15 nm intermembrane space (IMS) filled with electrolyte. Because the IMM area is roughly fivefold greater than the OMM area [110], the effective IMM area was increased by a factor of 5 compared to the OMM by increasing the local capacitance fivefold [17]. The cell plasma membrane and secretory granule membrane were assigned resting potentials of -70 mV and the IMM was assigned a resting potential of -174 mV , values typical for a chromaffin cell [82]. The E-field was applied by means of idealized planar electrodes placed at $x = -50 \mu\text{m}$ (anode) and $x = 50 \mu\text{m}$ (cathode) mimicking the

experimental setup. In the model, the applied E-field was calculated by dividing the voltage applied between the electrodes by the distance between the electrodes (i.e. 100 μm). The averaged voltage traces of the pulse captured during experiments were implemented in the cell model.

3.2.7.2 Cell system mesh and Voronoi cells (VC)

After constructing the geometry, a triangular mesh (Fig. 3.5) was generated using the mesh generation algorithm developed by Persson and Strang [94]. During mesh generation, nodes were fixed along the membranes. The triangular elements in the mesh varied in size, starting from a fine mesh in and around the membranes and expanding in size as the system boundary was approached. The cell membrane, nuclear envelope, mitochondrion membrane, ER membrane and granule membrane had 296, 93, 37, 19 and 15 membrane points, respectively. This number of membrane points was the maximum number that could be implemented with the available computer resources.

Since the meshing algorithm utilized required that the node spacing for all membranes be the same, a smaller membrane node spacing would be required to model structures smaller than 400 nm (400 nm represents the largest granule size in chromaffin cells [88]) or the realistic irregular shape of the ER and hence a much higher number of points on the cell membrane, thus increasing the amount of computation and data storage beyond the capacity of computers available in our laboratory.

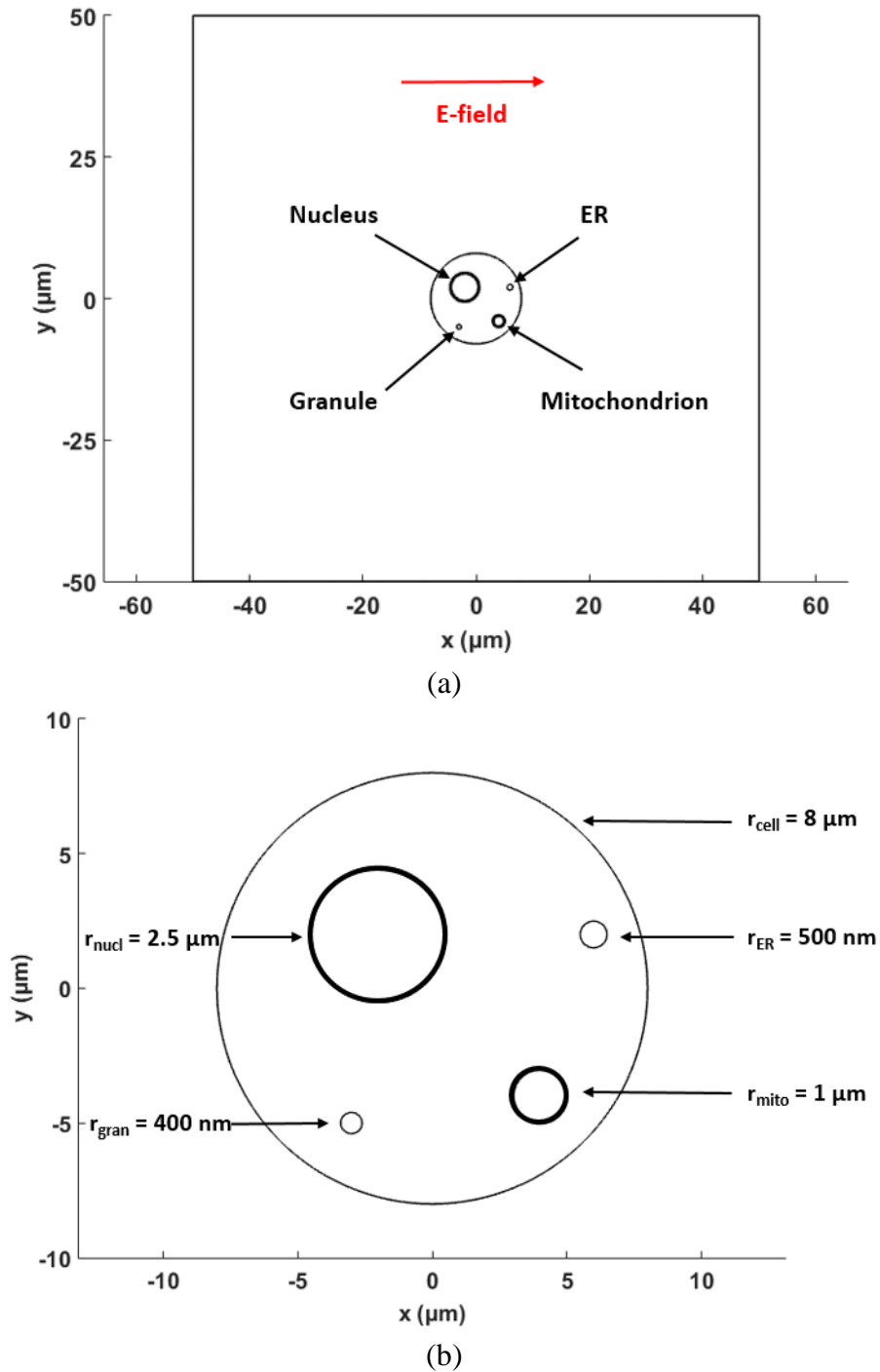


Fig. 3.4. Cell system geometry. (a) The cell was centered in a $100 \mu\text{m} \times 100 \mu\text{m}$ region. The anode was placed at $x = -50 \mu\text{m}$ and the cathode at $x = 50 \mu\text{m}$. (b) Cell and Ca^{2+} -storing organelle dimensions. A large structure representing the nucleus was placed at $(-2 \mu\text{m}, 2 \mu\text{m})$. Structures representing a mitochondrion, an ER and a large secretory granule were placed at $(4 \mu\text{m}, -4 \mu\text{m})$, $(6 \mu\text{m}, 2 \mu\text{m})$ and $(-3 \mu\text{m}, -5 \mu\text{m})$, respectively. Double-membrane structures are represented by thicker lines.

Table 3.1: Geometrical parameters used in the 2D cell model.

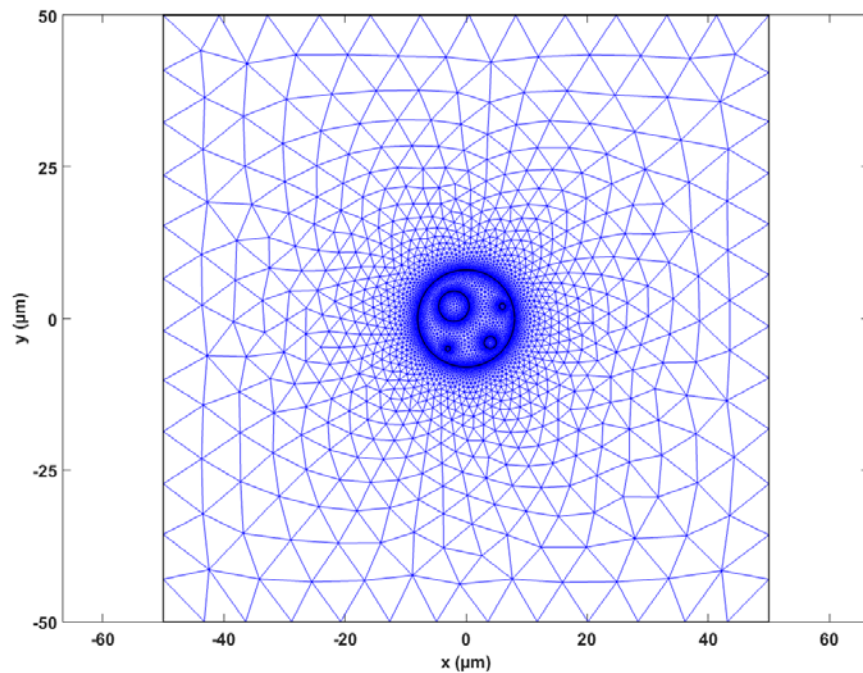
<u>Parameter</u>	<u>Size</u>
Cell radius ^a (r_{cell})	8 μm
Nucleus radius ^a (r_{nucl})	2.5 μm
Mitochondrion radius (r_{mito})	1 μm
ER radius (r_{ER})	500 nm
Secretory granule radius ^a (r_{gran})	400 nm
Membrane thickness (d_m)	5 nm
System depth (d)	10.67 μm

^a Specific for chromaffin cells [88]

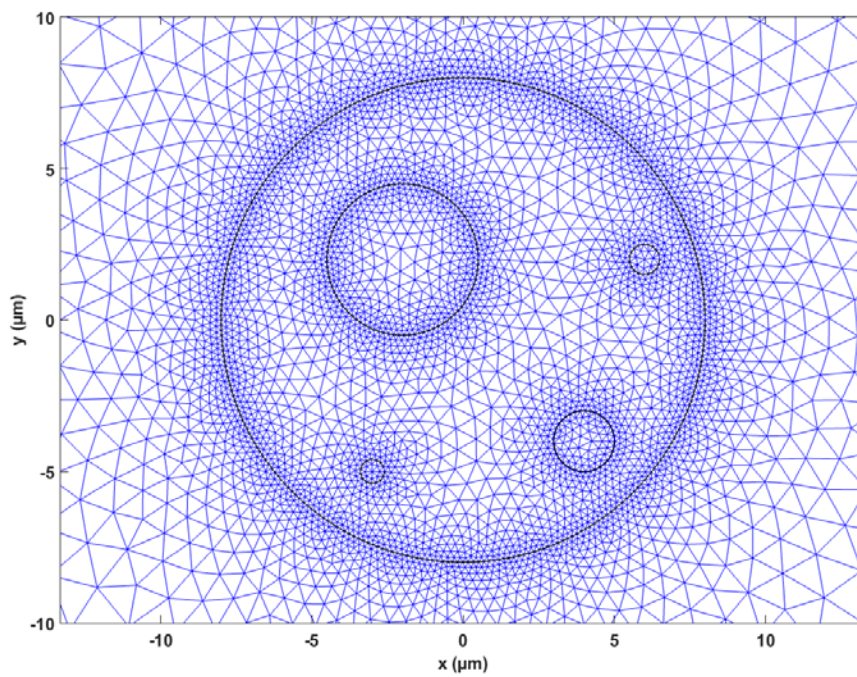
For times that are much smaller than the membrane charging time, equation (1) in Chapter 1 simplifies to:

$$V_m(t) = 1.5 E \cos\theta \frac{d_m}{\epsilon_m \epsilon_0} \left(\frac{1}{\rho_i + \rho_e/2} \right) t \quad (1)$$

where V_m is the TMP, E the amplitude of the external E-field, θ the angle between the normal to the membrane and the direction of the E-field, d_m the membrane thickness, ϵ_m the membrane permittivity, ϵ_0 the free space permittivity, ρ_i and ρ_e the resistivities of the intracellular and extracellular media, respectively. The TMP becomes independent of cell size and depends on the amplitude of the applied E-field and on the electrical properties used (assuming a fixed membrane thickness $d_m = 5$ nm). Although this equation was derived for a cylindrical cell, the size-independence also applies to irregular shaped cells and organelles [109]. Experiments conducted using NEPs also verified this assumption [70]. For the ultrashort 5-ns duration pulses used in this study, it was deemed adequate to represent the ER by a circle, neglecting the actual shape of the ER in chromaffin cells.



(a)



(b)

Fig. 3.5. Cell system mesh. The cell system mesh is shown at two scales (a,b). The mesh has 5238 nodes, 10452 triangles and 15689 edges, and a 170 nm membrane node spacing.

As described in Chapter 2, the VCs (Fig. 3.6) represented the small volumes into which the entire domain was discretized. Parallel RC circuits were placed between each pair of adjacent nodes in the geometry and the circuit nodes approximated the behavior of each VC with which they were associated. R and C values were computed based on the electrical properties assigned to each region (i.e. conductivity and permittivity) and on the geometrical parameters obtained from the mesh (i.e distance between nodes and length of VC edges).

Matlab was used to compute all geometrical parameters and circuit components (e.g. R and C), and create netlists containing all node elements and connections in the circuits. Netlists were then imported into a circuit simulation software package LT SPICE IV (Linear Technology, Milpitas, CA, USA) where the model was simulated. The generated data (i.e. node voltages and currents) were exported back into Matlab for plotting and analysis of the results.

3.2.7.3 *Electrical parameters of the 2D cell model*

Several chromaffin cell properties were obtained from pClamp software (version 8.2, Molecular Devices, Sunnyvale, CA). The seal resistance (R_m) and the cell capacitance (C_m) ranged between 5.5 and 10.8 G Ω (mean 7.4 ± 1.4 G Ω) and 3.7 and 8.2 pF (mean 5.4 ± 1.2 pF), respectively [91]. Cell membrane conductivity (σ_m) and permittivity (ϵ_m) were calculated from R_m and C_m values, respectively, as described below.

The plasma membrane conductivity (σ_m) was calculated by:

$$\sigma_m = \frac{1}{4\pi R_m} \left(\frac{1}{r_{\text{cell}} - d_m} - \frac{1}{r_{\text{cell}}} \right) = 8.3 \times 10^{-10} \text{ S/m} \quad (2)$$

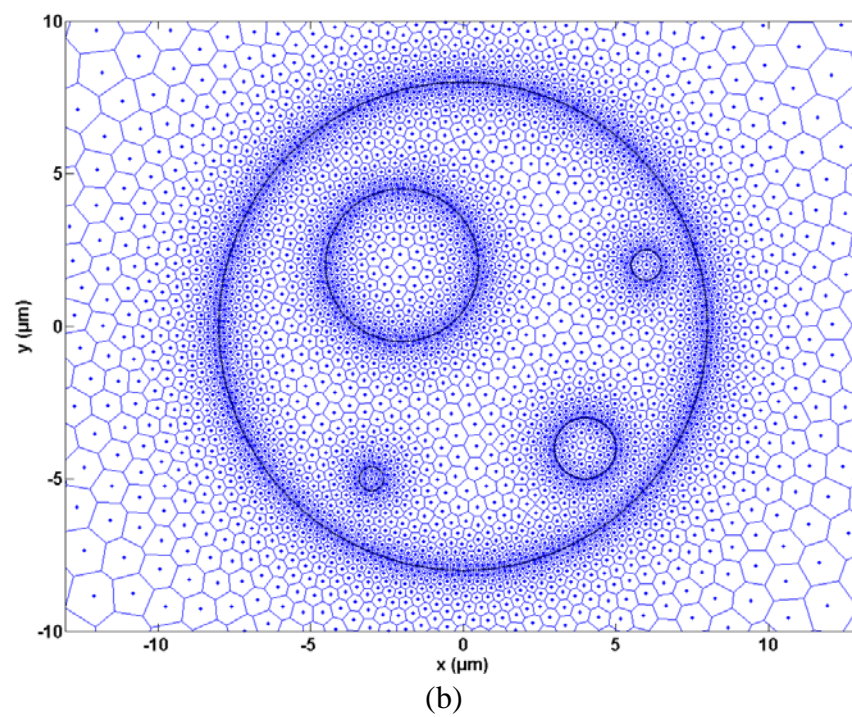
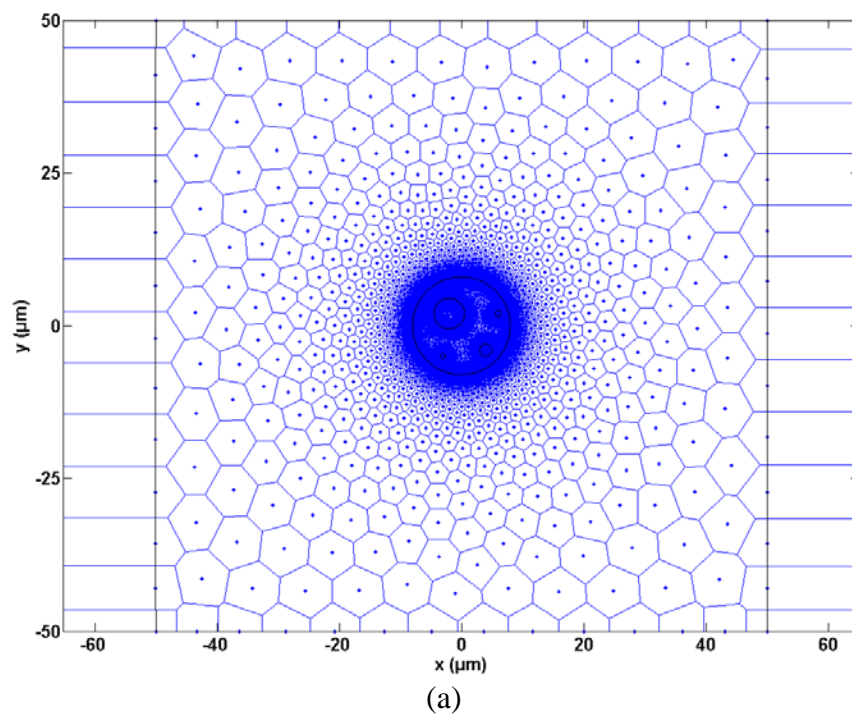


Fig. 3.6. Cell system Voronoi cells. The Voronoi diagram is shown at two scales (a,b). The relationship between the mesh and associated VCs is described in Chapter 2.

The plasma membrane permittivity (ϵ_m) was calculated by:

$$\epsilon_m = \frac{C_s d_m}{\epsilon_0} = 5 \quad (3)$$

where C_s is the specific membrane capacitance given by:

$$C_{sp} = \frac{C_m}{4\pi r_{cell}^2} \quad (4)$$

The calculated values for σ_m and ϵ_m were used in the cell model. All other electrical parameters were taken from the literature and are listed in Table 3.2.

3.2.7.4 *Asymptotic model of electroporation*

The electrical response of the cell subjected to the NEP was modeled using the asymptotic model of electroporation [34]. This model assumes that pores do not expand for nanosecond duration, high amplitude electric pulses [20]. The assumption of a constant pore size can safely be used in this study since the 5-ns duration pulse used in the experiments is too short to cause pore expansion.

Pore dynamics are defined in the simplified form of the Smoluchowski equation, which is an ordinary differential equation given by [93]:

$$\frac{dN(t)}{dt} = \alpha e^{\left(\frac{V_m(t)}{V_{ep}}\right)^2} \left(1 - \frac{N(t)}{N_0} e^{-q\left(\frac{V_m(t)}{V_{ep}}\right)^2} \right) \quad (5)$$

where N is the local pore density, α the pore creation rate coefficient, V_m the transmembrane potential, V_{ep} the characteristic voltage of electroporation, N_0 the

equilibrium pore density in the nonelectroporated membrane, and q an electroporation coefficient.

Table 3.2: Electrical parameters used in the 2D cell model [102,109,111].

<u>Conductivity (S.m⁻¹)</u>	<u>Value</u>
Extracellular medium ^a	1.3
Plasma membrane	8.3×10^{-10}
Nuclear envelope ^b	1×10^{-4}
ER membrane ^c	8.3×10^{-10}
Granule membrane ^c	8.3×10^{-10}
IMM	5×10^{-6}
OMM ^b	1×10^{-4}
Cytoplasm ^d	0.1-1.3
Nucleoplasm ^d	$2\sigma_{\text{cyto}}$
ER interior	0.5
Granule interior	0.5
Mitochondria interior	0.5
IMS	0.5
<u>Relative permittivity</u>	
Extracellular medium	80
Plasma membrane	5
Nuclear envelope	10
ER membrane	5
Granule membrane	5
IMM	5
OMM	5
Cytoplasm	80
Nucleoplasm	80
ER interior	80
Granule interior	80
Mitochondria interior	80
IMS	80

^a Conductivity was measured in our laboratory using an AR20 pH/Conductivity Meter (Hampton, NH, USA).

^b Conductivity was assumed higher than that of the plasma membrane because of the porous nature of the nuclear membrane and leaky nature of the OMM [17].

^c Conductivity was assumed to be the same as that of the plasma membrane.

^d Cytoplasmic conductivity was varied in the parametric study, and nucleoplasmic conductivity was varied accordingly.

Modeling the membranes required the incorporation of the nonlinear changes in membrane conductance due to electroporation. In addition to the passive RC circuit that exists between each pair of nodes that span the membrane, a current source i_p representing the current through pores was added to the membrane model (Fig. 3.7a). The current through pores in a small area A_m of the membrane was calculated from the conductance per pore G_m , the pore density N , and the TMP V_m by:

$$i_p(t) = G_p(V_m)N(t)A_m V_m(t) \quad (6)$$

The TMP was determined by the voltage difference across the membrane, and the conductance per pore, representing the increase in membrane conductivity due to electroporation, was calculated from:

$$G_p(V_m) = \sigma_p \frac{\pi r_m^2}{d_m} \frac{e^{v_m-1}}{\frac{\omega_0 e^{\omega_0 - \eta v_m - \eta v_m}}{\omega_0 - \eta v_m} e^{v_m} - \frac{\omega_0 e^{\omega_0 + \eta v_m + \eta v_m}}{\omega_0 + \eta v_m}} \quad (7)$$

where σ_p is the pore conductivity, r_m the fixed pore radius, d_m the membrane thickness, ω_0 the energy barrier inside a pore, η the relative entrance length of a pore, and v_m the dimensionless TMP given by:

$$v_m = \frac{V_m q_e}{kT} \quad (8)$$

$q_e = 1.6 \times 10^{-19}$ C is the charge of an electron, $k = 1.38 \times 10^{-23}$ J/K the Boltzmann constant, and T the absolute temperature.

The pore density N was calculated by solving equation (5) using the subcircuit shown in Fig. 3.7b. In this subcircuit, the voltage $N(t)$ across the capacitor C_N is given by:

$$\frac{dN(t)}{dt} = \frac{i_N(t)}{C_N} \quad (9)$$

where $C_N = 1/\alpha$ and i_N , representing the current flowing into the capacitor, is given by:

$$i_N(t) = e^{\left(\frac{V_m(t)}{V_{ep}}\right)^2} \left(1 - \frac{N(t)}{N_0} e^{-q\left(\frac{V_m(t)}{V_{ep}}\right)^2} \right) \quad (10)$$

When the sum of the currents flowing into the node is positive, a positive current flows into the capacitor, the capacitor charges and the voltage $N(t)$ at the node increases, thus creating pores. Otherwise, when the sum of the currents flowing into the node is negative, a negative current flows into the capacitor, the capacitor discharges and the voltage $N(t)$ at the node decreases, thus destroying pores [93]. The electroporation parameters used in equations (5)-(10) were taken from [93,96] and are defined in Table 3.3.

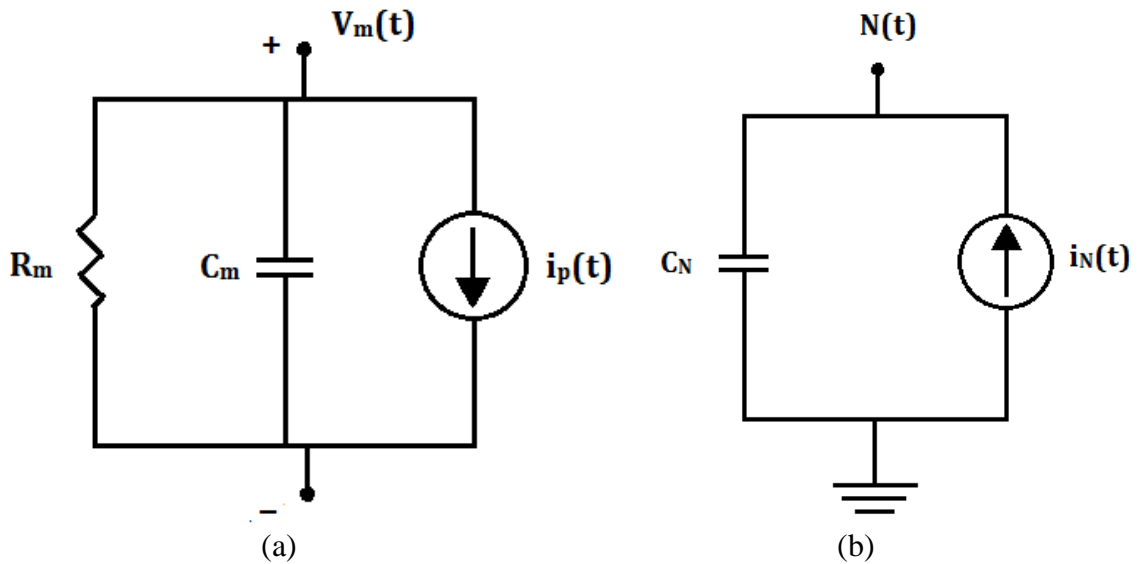


Fig. 3.7. Equivalent electrical circuit for the membrane. (a) Resistors R_m and capacitors C_m were placed between each pair of nodes spanning the membrane, in addition to the current i_p through pores. (b) The pore density subcircuit associated with each membrane circuit was used to solve the pore dynamics equation (5).

Table 3.3: Electroporation parameters used in the 2D cell model [93,96].

<u>Parameter</u>	<u>Value</u>
Pore creation rate coefficient (α)	$1 \times 10^9 \text{ m}^{-2} \text{ s}^{-1}$
Characteristic voltage of electroporation (V_{ep})	0.258 V
Electroporation coefficient (q)	2.46
Equilibrium pore density (N_0)	$1.5 \times 10^9 \text{ m}^{-2}$
Pore radius (r_m)	0.8 nm
Pore energy barrier (ω_0)	2.65 kT
Conductivity of aqueous solution in pores (σ_p)	1.3 S.m^{-1}
Pore relative entrance length (η)	0.15
Absolute temperature (T)	295 K

3.3. Results

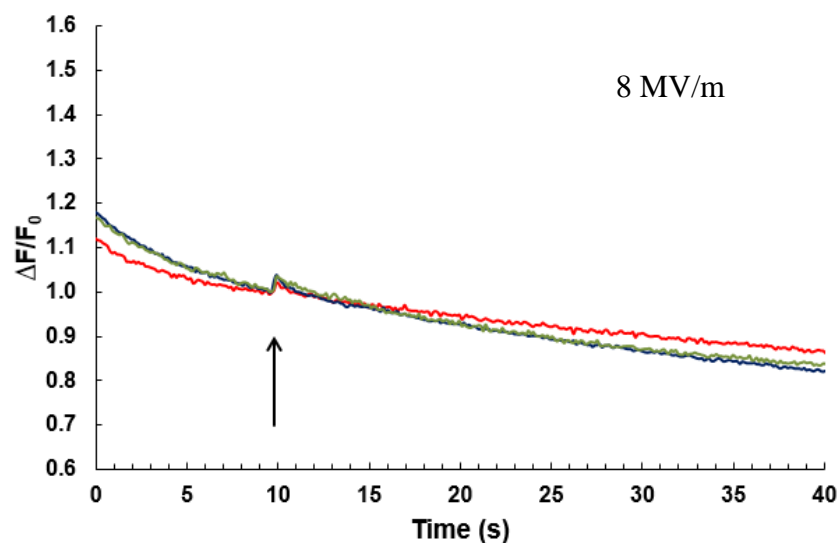
3.3.1 Experimental findings

3.3.1.1 *Ca²⁺ release from intracellular stores was first detectable at an E-field of 8 MV/m*

As previously reported [90,92], there is no evidence of Ca²⁺ being released from intracellular stores when adrenal chromaffin cells are exposed to up to ten, 5-ns duration pulses at an E-field amplitude of 5-6 MV/m. To determine whether higher E-field amplitudes can cause Ca²⁺ release from Ca²⁺-storing organelles, chromaffin cells were exposed to a single 5-6 ns duration pulse of increasing amplitude up to 21 MV/m, the highest achievable with our exposure setup. For these experiments, cells were exposed to an NEP in the absence of extracellular Ca²⁺. The threshold value of the E-field for causing Ca²⁺ release was defined as the E-field amplitude for which the first detectable increase in intracellular Ca²⁺ was observed.

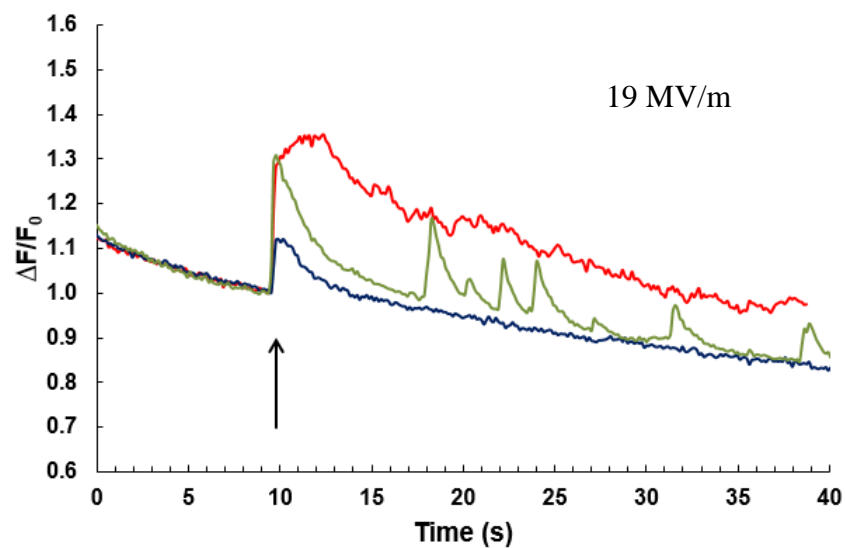
The fluorescence traces shown in Figs. 3.8a and 3.8b represent typical Ca²⁺ responses observed for chromaffin cells exposed to a single pulse applied at E-field amplitudes of 8 and 19 MV/m, respectively. At 8 MV/m, a small rise (~4%) in intracellular Ca²⁺ was

detectable. At 19 MV/m, the rise in intracellular Ca^{2+} was greater in magnitude. Fig. 3.8c represents the normalized Ca^{2+} release as a function of the applied E-field, calculated from the mean peak values \pm S.D. at the different E-field amplitudes. The results demonstrate that only half of the cells exposed to an E-field amplitude of 8 MV/m responded to the pulse but that the number of cells responding to a pulse increased with the applied E-field*. In addition, the rise in intracellular Ca^{2+} increased in magnitude with E-field amplitude as well. In general, cell responses were variable in magnitude from cell to cell or absent in some cells even at the highest E-field amplitudes applied. They also displayed either single Ca^{2+} transients or multiple Ca^{2+} transients (i.e., spiky Ca^{2+} activity). When spiky Ca^{2+} activity was observed, the spikes occurred at distinct regions in the cytoplasm.

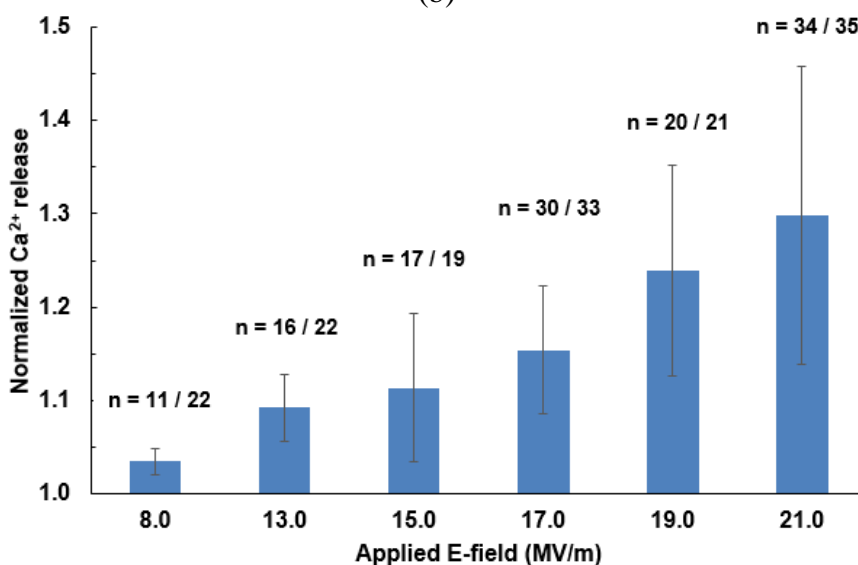


(a)

* Independent experiments performed by Dr. Nina Semenova, Frank Reidy Research Center for Bioelectrics, Old Dominion University, also confirmed that high E-field thresholds were required to cause Ca^{2+} release from intracellular stores in chromaffin cells (unpublished data).



(b)



(c)

Fig. 3.8. Release of Ca^{2+} from intracellular stores in chromaffin cells evoked by a 5-6 ns pulse. The traces shown in (a) and (b) are typical of responses observed in cells exposed to a single pulse applied at E-field amplitudes of 8 and 19 MV/m, respectively, in the absence of extracellular Ca^{2+} . $\Delta F/F_0$ was calculated by subtracting the background fluorescence from the fluorescence of the cells and normalizing it to the fluorescence intensity value at the time when the pulse was applied (arrow). Shown in (c) is the magnitude of the Ca^{2+} response as a function of the applied E-field. Normalized Ca^{2+} release represents the mean of the peak responses of the cells \pm S.D., where n represents the number of cells responding to the pulse out of the total number of cells tested at each E-field amplitude.

Even though the duration of the pulse is only 5-6 ns, increasing the E-field amplitude could cause heating that in turn could contribute to the graded cell response observed in Fig. 3.8c. To address this concern, the extent to which temperature was increased was calculated from the adiabatic heat equation given by equation (1) [112] using the local E-field values calculated from SEMCAD X:

$$\Delta T = \frac{\sigma \cdot |E|^2 \cdot \Delta t \cdot N}{c_{\text{water}} d_{\text{water}}} \quad (1)$$

where, $c_{\text{water}} = 4.184 \text{ Jg}^{-1}\text{K}^{-1}$ and $d_{\text{water}} = 0.997 \times 10^6 \text{ gm}^{-3}$ are the specific heat capacity and mass density of water, respectively, $\sigma = 1.3 \text{ Sm}^{-1}$ is the conductivity of BSS at room temperature, E the amplitude of the applied E-field, Δt the pulse duration and N the pulse number. The rise in temperature calculated at the center of the $100 \mu\text{m}$ gap between the electrodes for the different E-field amplitudes is shown in Table 3.4. Because the calculations did not take into account heat dissipation between the rods and the BSS, the value of 0.69°C calculated at the highest E-field amplitude of 21 MV/m represents the worst case scenario. Thus, this small heating effect by the NEP is very unlikely to be contributing to the graded intracellular Ca^{2+} release.

Table 3.4: Temperature increase as a function of E-field amplitude.

E-field (MV/m)	8	13	15	17	19	21
$\Delta T(^{\circ}\text{C})$	0.10	0.26	0.35	0.45	0.56	0.69

- a. *The higher E-field amplitudes required to cause release of Ca^{2+} from internal stores did not have any apparent adverse effects on the cells*

Possible adverse effects on cells exposed to a single 5-ns, 17 MV/m pulse were first explored by examining cell morphology. For this determination, bright field images of chromaffin cells were taken immediately before and then 2 min after a pulse. As shown in Fig. 3.9, there was no sign of swelling of the cells even at 17 MV/m. The lack of swelling was confirmed by comparing the mean cell area calculated before ($164.2 \pm 29.2 \mu\text{m}^2$, n = 56 cells) and after ($164.1 \pm 28.8 \mu\text{m}^2$, n = 56 cells) pulse application.

Previous experiments have shown that exposing chromaffin cells to a single 5-ns, 5-6 MV/m pulse does not permeabilize the plasma membrane to YO-PRO-1, a membrane impermeable dye that is used as an indicator of plasma membrane poration in other cell types [60]. To explore whether the high field amplitudes caused a permeability change in the plasma membrane, chromaffin cells were exposed to a single pulse applied at an E-field amplitude of 17 MV/m in the presence of YO-PRO-1. The cells did not take up the dye up to 12 min after pulse application, indicating that while the plasma membrane most likely was still permeable to small ions like Na^+ [91], it was not permeable to dyes such as YO-PRO-1.

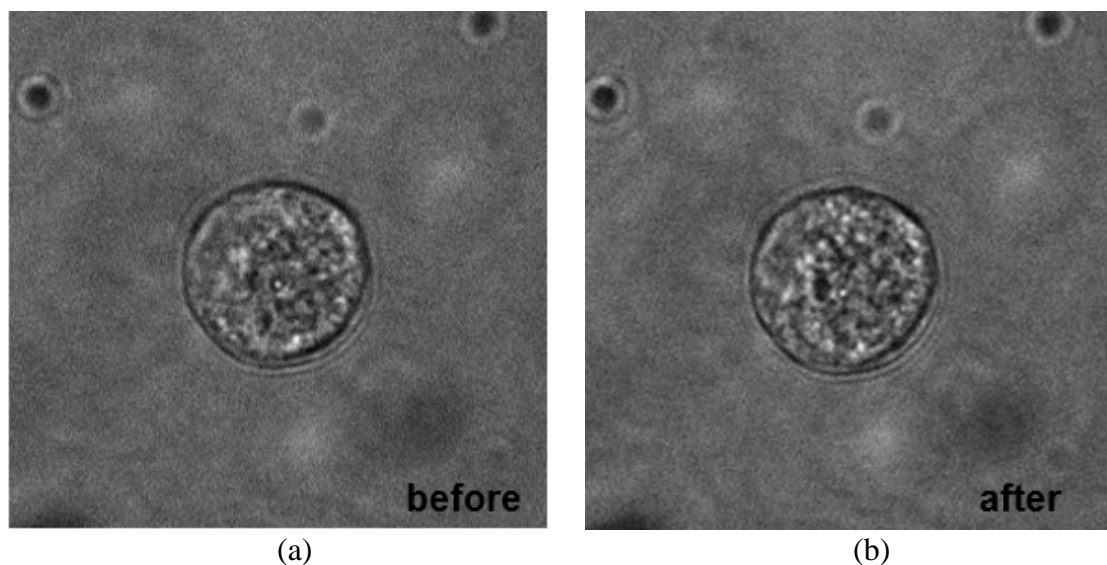


Fig. 3.9. Lack of effect of a 17 MV/m pulse on chromaffin cell morphology. The photomicrographs show the appearance of a chromaffin cell (a) before and (b) 2 min after exposure to a single 5-ns duration pulse. Images were obtained at 100X.

b. Ca^{2+} release evoked by a single pulse was immediate versus a delayed response evoked by a receptor agonist

The time for the onset of Ca^{2+} release evoked by a 5-ns pulse was compared to that evoked by the mixed nicotinic and muscarinic receptor agonist carbachol (100 μ M). When Ca^{2+} is present in the extracellular solution, carbachol activates both types of cholinergic receptors on the plasma membrane of chromaffin cells, causing Ca^{2+} influx through VGCCs and Ca^{2+} release from internal stores via activation of the PLC/IP₃ pathway [113]. The latter response can be investigated by application of the agonist in the absence of extracellular Ca^{2+} . When carbachol was applied to chromaffin cells in Ca^{2+} -free BSS, there was a delayed (up to 5 s) increase in intracellular Ca^{2+} levels (1.71 ± 0.51 S.D., $n = 6$ cells) (Fig. 3.10a), contrasting with the immediate and sharper Ca^{2+} response (1.61 ± 0.27 S.D., $n = 28$ cells) (Fig. 3.10b) in the presence of extracellular Ca^{2+} that involves both Ca^{2+} influx

and Ca^{2+} release mediated by IP_3 . The delayed rise in Ca^{2+} release following application of carbachol in the absence of extracellular Ca^{2+} is consistent with published data on receptor agonists acting through the breakdown of inositol lipids in chromaffin cells [114,115].

Compared to the delay in Ca^{2+} release evoked by carbachol, NEP-induced Ca^{2+} release was immediate, as previously shown in Figs. 3.8a and 3.8b. This suggests that a mechanism that is faster than the activation of the IP_3 pathway underlies NEP-induced Ca^{2+} mobilization from intracellular stores, and is consistent with Ca^{2+} being released from intracellular stores through nanopores that have formed in the membranes of Ca^{2+} -storing organelles.

3.3.1.2 Plasma membrane poration occurred at E-fields lower than those that caused intracellular membrane poration

As stated previously, the rapid release of Ca^{2+} from intracellular stores in chromaffin cells evoked by a single pulse is consistent with poration of membranes of intracellular Ca^{2+} -storing organelles rather than with activation of the PLC/ IP_3 signaling pathways. The poration of these membranes requires E-field amplitudes greater than 8 MV/m. The next goal was to directly compare the E-field threshold required to cause Ca^{2+} release from intracellular stores to that causing permeabilization of the plasma membrane. We have recently reported that a single 5-ns, 6 MV/m pulse applied to chromaffin cells permeabilizes the plasma membrane, causing an inward current in which Na^+ is a carrier [91].

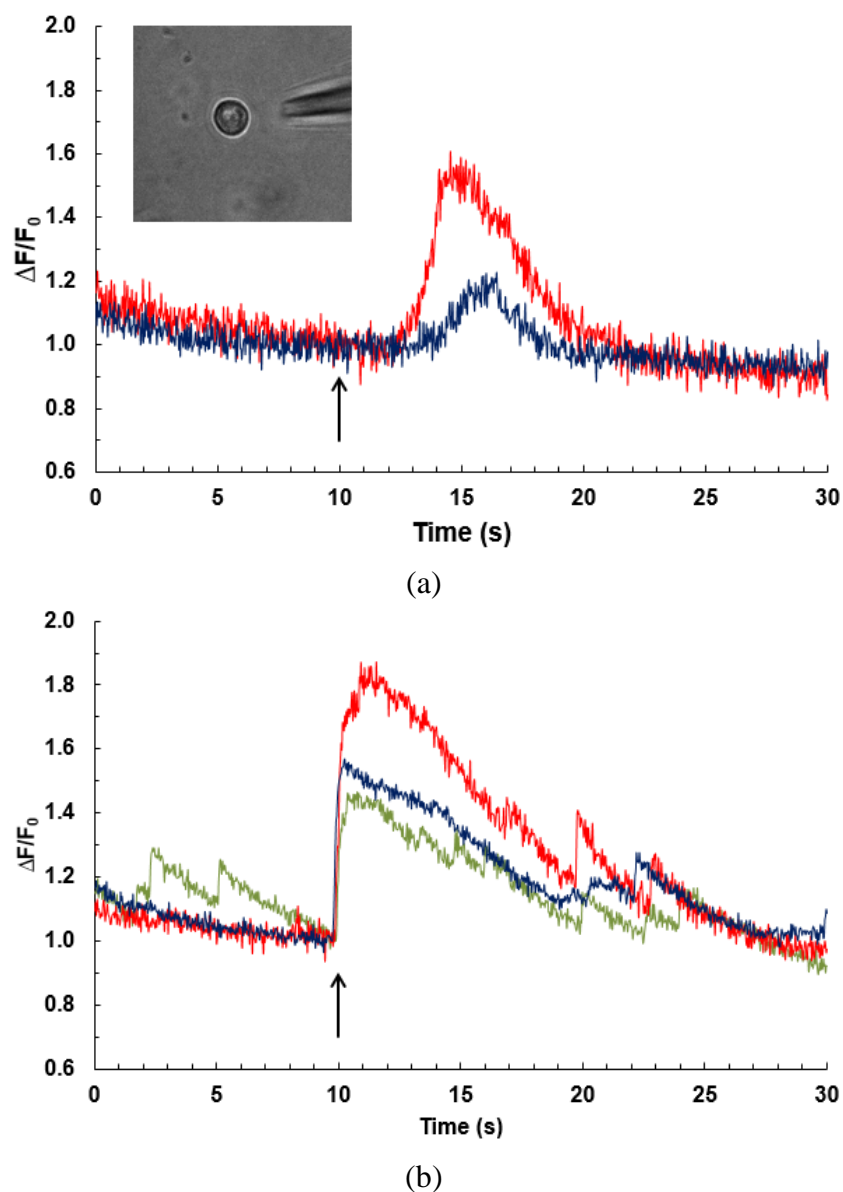
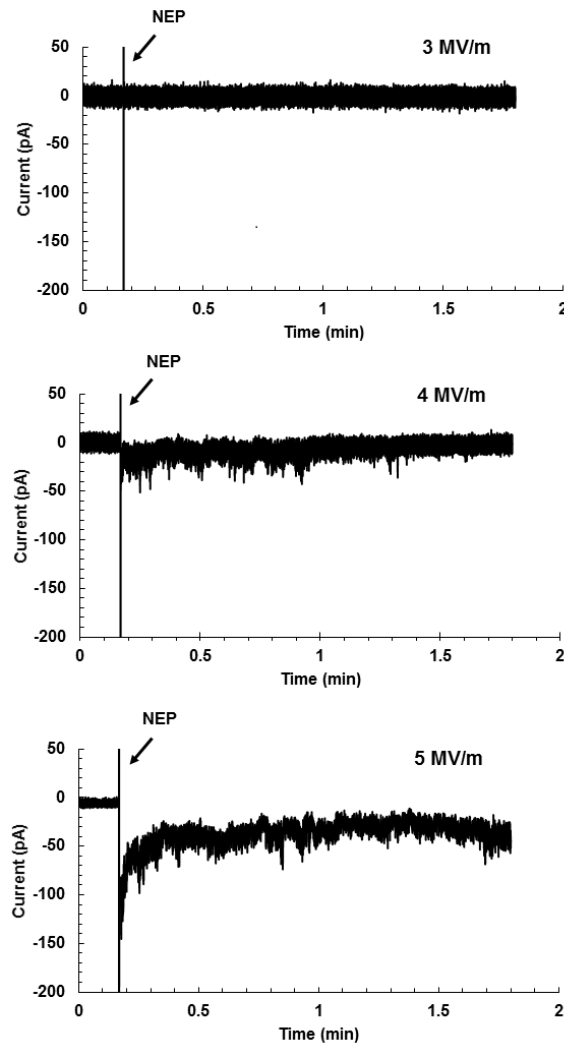


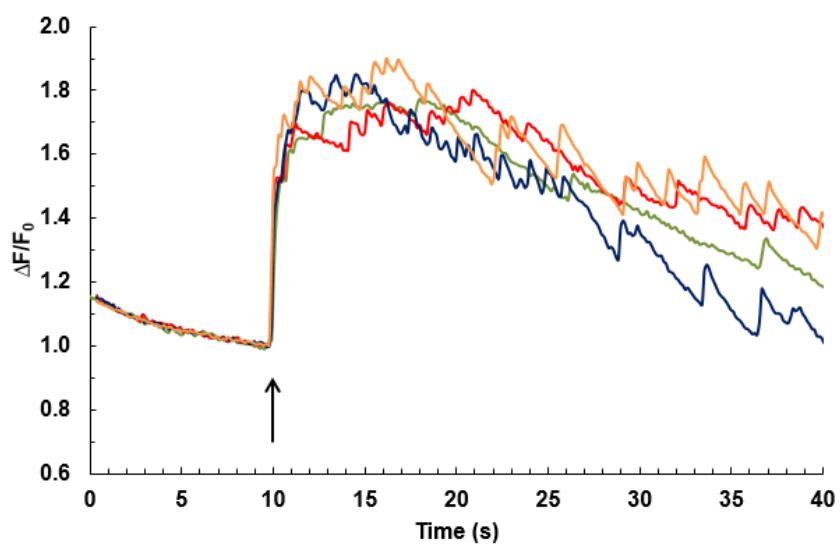
Fig. 3.10. Ca^{2+} transients evoked by carbachol. The traces shown in (a) and (b) are representative of Ca^{2+} responses in chromaffin cells stimulated by a brief (5 ms) application of carbachol (100 μM) via a pressure ejection pipette (shown in the inset) in the absence and presence of extracellular Ca^{2+} , respectively. $\Delta F/F_0$ was calculated by subtracting the background fluorescence from the fluorescence of the cells and normalizing it to the fluorescence intensity value at the time when carbachol was applied (arrow).

To determine the threshold E-field amplitude that causes plasma membrane permeabilization, patch-clamped cells were exposed to a single 5-6 ns pulse at E-field

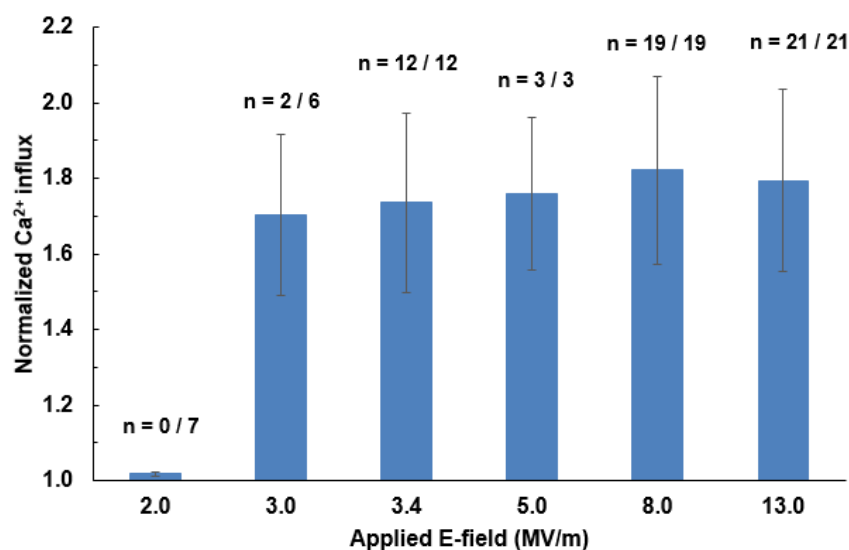
amplitudes ranging from 3 to 5 MV/m. The results showed that a single pulse evoked inward currents at a threshold E-field of 4 MV/m (Fig. 3.11a), for which the first detectable increase in inward current was observed, and a higher E-field amplitude caused a larger inward current. This threshold corresponded to a similar threshold of 3-4 MV/m for evoking Ca^{2+} influx as determined by fluorescence imaging experiments (Figs. 3.11b and 3.11c). The threshold E-field was defined in these experiments as the value of the E-field amplitude for which all the cells responded to the pulse.



(a)



(b)



(c)

Fig. 3.11. E-field thresholds for plasma membrane permeabilization and Ca²⁺ influx. The traces shown in (a) are representative inward current responses following exposure of a patch-clamped cell to a single pulse applied at E-field amplitudes of 3, 4 and 5 MV/m. The fluorescence traces in (b) are representative of Ca²⁺ responses in Calcium Green-1-loaded cells evoked by a single 5-6 ns duration pulse applied at an E-field amplitude of 3.4 MV/m in the presence of extracellular Ca²⁺. $\Delta F/F_0$ was calculated by subtracting the background fluorescence from the fluorescence of the cells and normalizing it to the fluorescence intensity value at the time when the pulse was applied (arrow). Shown in (c) is Ca²⁺ influx as a function of the applied E-field. Normalized Ca²⁺ influx represents the mean of the peak responses of the cells \pm S.D., where n represents the number of cells responding to the pulse out of the total number of cells tested at each E-field amplitude.

3.3.2 Numerical modeling results

The requirement for higher E-field amplitudes to porate intracellular membranes (i.e. > 8 MV/m) relative to those required to porate the plasma membrane (i.e. 4 MV/m) in chromaffin cells was addressed by conducting a parametric study using the 2D cell model. The cytoplasmic conductivity (σ_{cyto}) has been shown to affect the E-field thresholds required for electroporation of the plasma membrane as well as the membranes of the intracellular organelles [116]. In addition, secretory granules occupy $\sim 30\%$ of the volume of the cytosol in chromaffin cells [88], so we considered the possibility that their presence might affect the dielectric properties of the cytoplasm. For these reasons, σ_{cyto} was chosen as the parameter to be changed in the model and its value was changed from 0.1 to 1.3 S/m (the range was set between values reported in [102,116]).

To determine the numerical E-field threshold required to porate the plasma membrane as well as the membranes of intracellular organelles, the amplitude of the E-field was varied in the simulations from 1 to 21 MV/m. The threshold E-field for significant electroporation was defined as the E-field amplitude that results in a pore density of 10^{14} m^{-2} at the anodic pole of a membrane (see Chapter 2) [42,116].

3.3.2.1 *The E-field threshold for plasma membrane electroporation correlated with the experimentally determined E-field threshold for a low cytoplasmic conductivity*

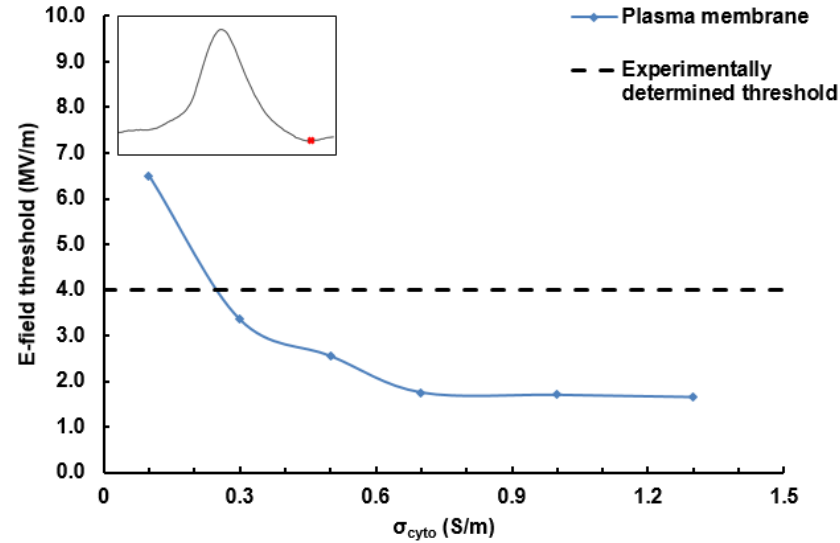
Because the plasma membrane is the first cellular membrane exposed to the external E-field, the effect of σ_{cyto} on the electroporation of the plasma membrane was studied first. For each value of σ_{cyto} , the E-field value that resulted in a pore density of 10^{14} m^{-2} at the anodic pole of the plasma membrane at the end of the pulse (indicated by a dot on the inset

plot in Fig. 3.12a) was considered to be the E-field threshold causing plasma membrane electroporation. When σ_{cyto} increased from 0.1 to 1.3 S/m, the E-field threshold required for electroporating the plasma membrane decreased from 7 to 1 MV/m, respectively (Fig. 3.12a). This decrease in the E-field threshold is attributed to the plasma membrane charging time (see equation (2), Chapter 1) that decreases at higher σ_{cyto} values, as shown in Fig. 3.12b. Because the membrane takes longer to charge when σ_{cyto} is low, it requires higher E-field thresholds to electroporate. These results are consistent with the results of Retelj et al. (2013) showing that for a 4-ns pulse the E-field threshold required to electroporate the plasma membrane decreased as σ_{cyto} increased [116].

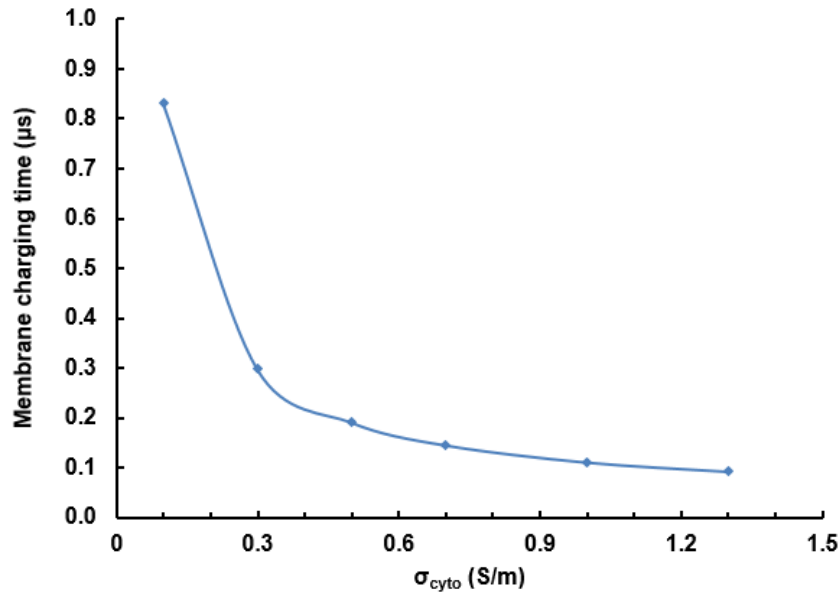
Of the values of σ_{cyto} tested, which as stated ranged from 0.1 to 1.3 S/m, $\sigma_{\text{cyto}} = 0.3$ S/m gave an E-field threshold for plasma membrane electroporation close to the experimental E-field threshold of 4 MV/m found to cause plasma membrane permeabilization in chromaffin cells (Fig. 3.11a). Therefore, a value of 0.3 S/m for the cytoplasmic conductivity was adopted in further simulations and was assumed to be the one possibly representing the conductivity of the cytoplasm in chromaffin cells.

3.3.2.2 Intracellular organelle membranes electroporated at E-field amplitudes lower than the experimentally determined thresholds when a low cytoplasmic conductivity was used

Although the source of the Ca^{2+} that was experimentally being released in chromaffin cells in response to a 5-6 ns electric pulse is not yet known, the ER, which has been shown to be the target of NEPs in other cell types [52-54], is the likely source of released Ca^{2+} in chromaffin cells as well. However, other potential targets of nanosecond pulses in chromaffin cells are the Ca^{2+} -storing secretory granules and mitochondria.



(a)



(b)

Fig. 3.12. Influence of σ_{cyto} on the electroporation of the plasma membrane. (a) Influence of σ_{cyto} on the E-field threshold amplitudes required for plasma membrane electroporation. The black dashed horizontal line on the plot indicates the 4 MV/m E-field threshold found experimentally to permeabilize the plasma membrane. The red point (inset) on the applied electric pulse represents the time point at the end of the pulse when a pore density of 10^{14} m^{-2} was computed. (b) Influence of σ_{cyto} on the plasma membrane charging time. The charging time (indicated by the dots) was calculated for each σ_{cyto} value using equation (2) in Chapter 1.

To study the effect of pulse amplitude on the electroporation of the intracellular membranes of the ER, secretory granule and mitochondrion, the amplitude of the applied E-field was increased from 1 to 14 MV/m, and the TMP (Fig. 3.13a) and pore density (Fig. 3.13b) were computed at the anodic pole of each membrane. Simulation results showed that increasing the amplitude of the applied E-field increased the TMP and the pore density on all membranes. The results also showed that the plasma membrane required the lowest E-field amplitudes (3 MV/m) to electroporate, whereas the IMM required the highest E-field amplitudes (13 MV/m) to electroporate because of the increased membrane capacitance assigned to the IMM, as previously explained in the Methods section. Furthermore, the E-field threshold found to electroporate the ER and secretory granule membranes was 4 MV/m, much lower than the experimental threshold of 8 MV/m that was required to cause Ca^{2+} release from intracellular stores.

The saturation effect observed in the TMP (and consequently the pore density) is due to the high conductance of the membranes, which in turn is due to electroporation. This high conductance state decreases the voltage drop across the membranes thus limiting the TMP from increasing beyond 1.6 V [93]. However, such saturation effect was not observed experimentally since Ca^{2+} release from intracellular stores kept increasing after reaching threshold, as shown in Fig. 3.8c.

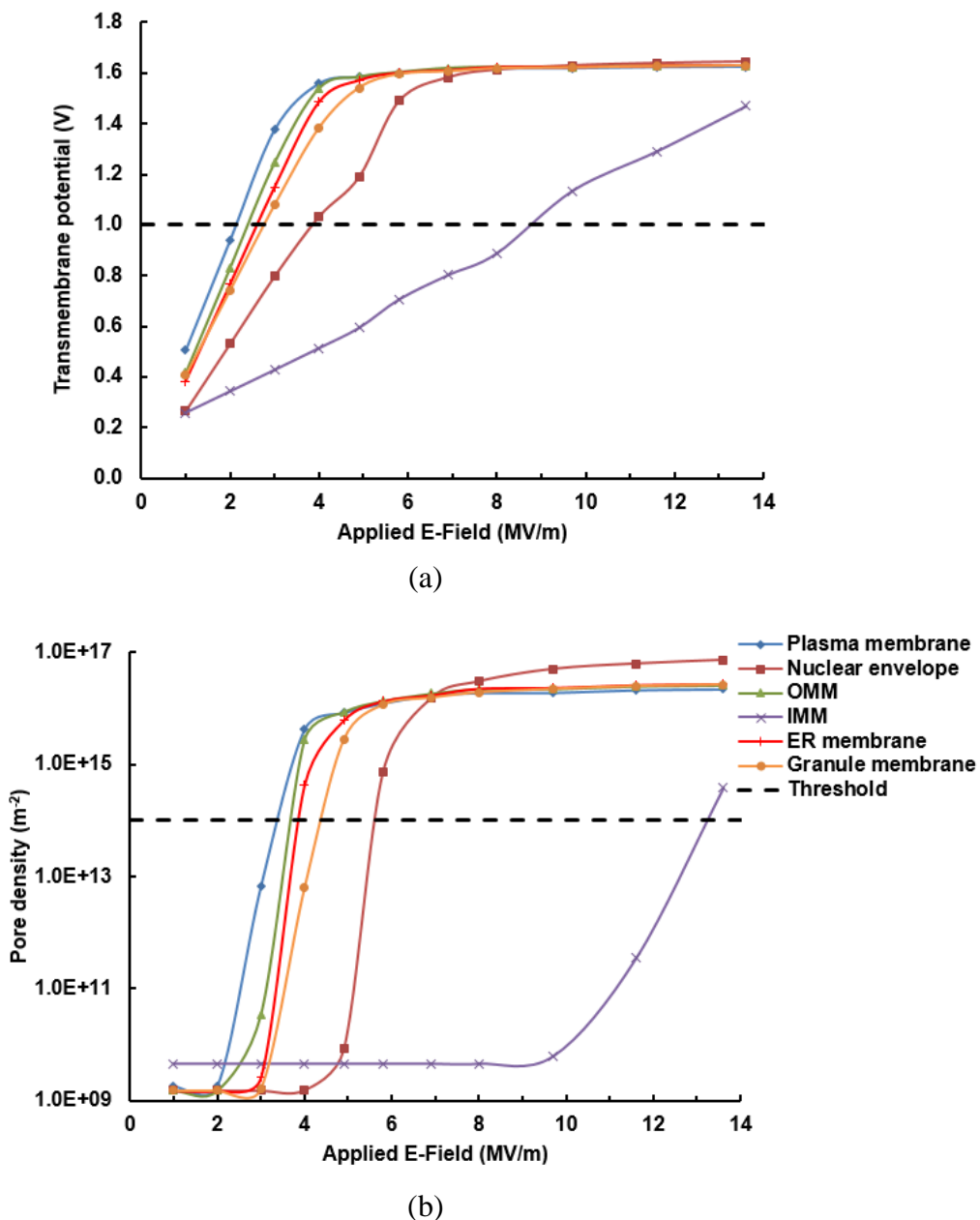


Fig. 3.13. Transmembrane potential (TMP) and pore density as a function of E-field amplitude. (a) TMP and (b) pore density computed at the anodic pole of all membranes at the end of the pulse for a range of E-field amplitudes from 1 to 14 MV/m. The black dashed horizontal line in (a) indicates the threshold for REB (~ 1 V), and in (b) indicates the threshold for a pore density of $10^{14} m^{-2}$.

To correlate the time course of pore formation obtained from the model with the immediate Ca^{2+} release observed during experiments (Figs. 3.8a and 3.8b), the temporal evolution of the pore density at the anodic pole of all membranes was computed for a cell exposed to a pulse applied at an E-field amplitude of 4 MV/m (Fig. 3.14). Simulation results showed that pores form in the plasma membrane, OMM, ER and granule membranes within a few nanoseconds as observed by the increase in pore density around 15 ns. These results are in agreement with the experimental findings showing immediate Ca^{2+} release from the internal stores, thus supporting the hypothesis that the immediate NEP-induced Ca^{2+} release from intracellular stores in chromaffin cells is due to pores that have formed in the membranes of intracellular Ca^{2+} -storing organelles.

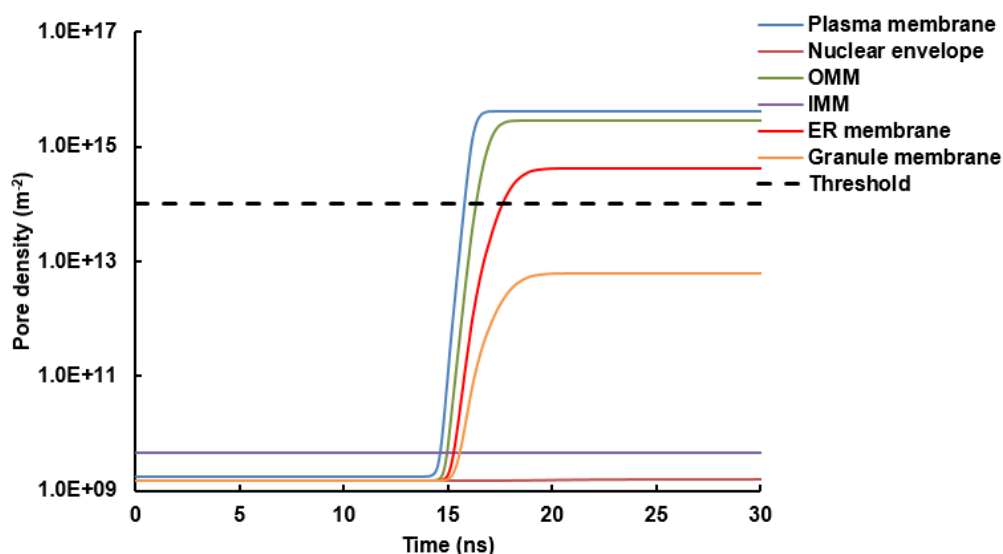


Fig. 3.14. Temporal evolution of pore density computed at the anodic pole of the different cellular membranes in response to a pulse applied at an E-field amplitude of 4 MV/m. The black dashed horizontal line on the plot indicates the threshold for a pore density of 10^{14} m^{-2} .

3.3.2.3 *Changing the cytoplasmic conductivity did not affect the E-field threshold amplitudes required to electroporate the ER and granule membranes and OMM*

When the value of σ_{cyto} was set to 0.3 S/m in the simulations, the ER and granule membranes as well as the OMM electroporated at E-field thresholds of 4 MV/m, lower than the experimental threshold value of 8 MV/m. The IMM, on the other hand, electroporated at an E-field threshold of 13 MV/m because of its increased membrane capacitance.

To determine whether changing the cytoplasmic conductivity would affect the E-field thresholds required to porate the ER and granule membranes and the OMM, σ_{cyto} was varied in the model from 0.1 to 1.3 S/m. Fig. 3.15 shows that for any value of σ_{cyto} , the E-field thresholds required for electroporating the membranes of the ER and secretory granule and the OMM did not exceed 6 MV/m, a value that was still lower than the 8 MV/m observed experimentally.

3.3.3 **Reducing the electrical conductivity of the secretory granule interior increased the E-field threshold required for electroporating the granule membrane**

Clearly, changing the cytoplasmic conductivity alone was not sufficient to explain the two-fold difference in the experimentally determined and numerically computed E-field thresholds necessary to electroporate the plasma membrane and the membranes of the ER and secretory granule, potential targets of NEPs in chromaffin cells.

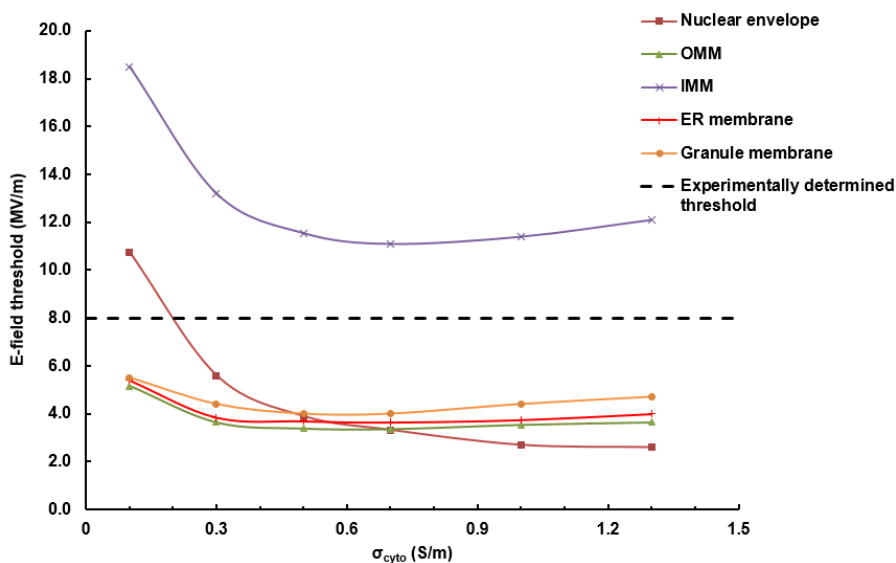


Fig. 3.15. Influence of σ_{cyto} on the E-field threshold amplitudes required for electroporation of the nuclear envelope, OMM, IMM, ER and secretory granule membranes. The black dashed horizontal line on the plot indicates the 4 MV/m E-field threshold found experimentally to cause Ca^{2+} release from intracellular stores.

According to equation (1), for ultrashort (< 10 ns) electric pulses the TMP becomes independent of organelle size and dependent on the electrical properties of the organelle, more specifically, on the permittivity of the organelle membrane and conductivity of the organelle interior. The model was therefore taken a step further and a change in the parameters that were specific to the individual intracellular Ca^{2+} -storing organelles was considered. A low conductivity value of 0.01 S/m was chosen arbitrarily for the granule interior because the contents of the granules are locked in a chromogranin A protein matrix [89]. Thus, the granule can be modeled as a solid mass of protein with a low intragranular conductivity [117].

Modeling results showed that decreasing the conductivity of the granule interior from 0.5 to 0.01 S/m increased the E-field threshold amplitude required to electroporate the

granule membrane from 4 to 9 MV/m, respectively (Fig. 3.16), a value that agreed better with the experimental E-field thresholds required to cause Ca^{2+} release from intracellular organelles. The effect of the organelle interior conductivity on the E-field threshold amplitude required to electroporate the organelle membrane was also predicted in another modeling study using a 4-ns electric pulse. In that study, the E-field threshold required to electroporate liposome membranes increased when the conductivity of the liposome interior decreased [116].

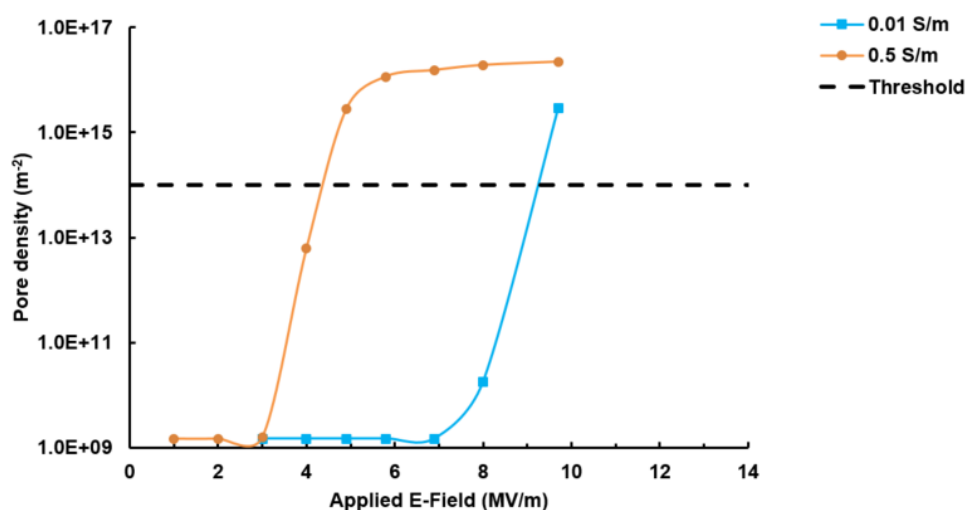


Fig. 3.16. Pore density computed at the anodic pole of the granule membrane, at the end of the pulse, for the different conductivities of the granule interior. The black dashed horizontal line indicates the threshold for a pore density of 10^{14} m^{-2} .

3.4. Discussion

The goal of the present study was to investigate whether Ca^{2+} release from intracellular Ca^{2+} stores occurs when chromaffin cells are exposed to 5-ns pulses applied at higher E-field amplitudes. A distinguishing feature of NEPs is that their duration is shorter than the charging time of the plasma membrane and hence they would be expected to penetrate into

cells and affect membranes of intracellular organelles, by causing for example, Ca^{2+} release from internal stores [52-57]. But in excitable adrenal chromaffin cells exposed to up to ten 5-ns, 5-6 MV/m electric pulses, the only response observed is influx of Ca^{2+} through VGCCs. No evidence of Ca^{2+} release from intracellular stores was apparent [92]. Using a combination of experimental and numerical modeling approaches, we were able to determine the E-field threshold amplitudes required to permeabilize the plasma membrane and those required to cause Ca^{2+} release from intracellular stores.

3.4.1 Plasma membrane permeabilization

3.4.1.1 *Experimental E-field threshold*

In this study, whole-cell recordings obtained from patch-clamped chromaffin cells determined that the E-field threshold for a 5-6 ns pulse to permeabilize the plasma membrane was 4 MV/m. In addition, fluorescence imaging of Calcium Green-1 loaded cells demonstrated that a single 5-6 ns pulse triggered Ca^{2+} influx into cells at an E-field threshold amplitude of 3.4 MV/m, matching well with the E-field threshold value of 4 MV/m that caused plasma membrane permeabilization to Na^+ . These findings support the hypothesis that Na^+ influx via nanopores causes transient plasma membrane depolarization that underlies activation of VGCCs and Ca^{2+} influx [92].

3.4.1.2 *Computed E-field threshold*

Results obtained using the 2D numerical cell model of a chromaffin cell showed that nanopores form in the plasma membrane at an E-field threshold amplitude of 4 MV/m, for

a value of $\sigma_{\text{cyto}} = 0.3 \text{ S/m}$, thus correlating with the experimental findings. Because chromaffin granules form a condensed protein matrix that occupies ~30% of the volume of the cytosol in chromaffin cells [88,89], a small value (0.3 S/m) of σ_{cyto} is reasonable. This value falls well within the reported values of σ_{cyto} measured in other cell types (values reported in Table 2.3) and is therefore assumed to be representative of the conductivity of the cytoplasm in chromaffin cells.

On the other hand, we have reported in Chapter 2 that the measured σ_{cyto} of a chromaffin cell was 1.3 S/m. However, this value represents the cytosol conductivity excluding the presence of the secretory granules. Preliminary calculations of the effective value of σ_{cyto} (i.e. including the secretory granules) estimated σ_{cyto} to be between 0.4 and 0.5 S/m (manuscript in preparation). A conductivity value lower than 1.3 S/m is expected because of the condensed protein matrix occupying the cytosol. These calculations agree well with the value of $\sigma_{\text{cyto}} = 0.3 \text{ S/m}$ obtained from the model constructed in this work, which resulted in a good agreement between the simulated and experimental results.

3.4.2 Permeabilization of the membranes of intracellular Ca^{2+} -storing organelles

3.4.2.1 *Experimental E-field threshold*

Experiments conducted in the absence of extracellular Ca^{2+} indicate that chromaffin cells exposed to a single 5-6 ns pulse require E-field amplitudes greater than 8 MV/m to cause Ca^{2+} release from internal stores. Thus, a twofold difference in the E-field threshold amplitude was observed for permeabilizing the plasma membrane and the membranes of intracellular organelles. A similar difference was reported by Iurii et al. (2013) showing that a single 60-ns electric pulse triggers Ca^{2+} efflux from the ER in CHO cells at an E-

field threshold amplitude of 19 kV/cm (1.9 MV/m) and Ca^{2+} influx into cells directly across the cell membrane, which is indicative of membrane permeabilization, at an E-field threshold amplitude of 9 kV/cm (0.9 MV/m) [54]. However, our findings disagree with those reported by Scarlett et al. (2009) showing that 60-ns pulses cause Ca^{2+} release from the ER in Jurkat cells at E-field amplitudes of 25-50 kV/cm (2.5-5 MV/m), while the threshold required to cause Ca^{2+} influx directly across the plasma membrane into cells is 100 KV/cm (10 MV/m) [52]. The differences in the cell responses observed could be attributed to the variables that exist between laboratories, such as the cell type used, exposure setup, experimental conditions, pulse duration, etc.

3.4.2.2 Computed E-field threshold

When the value of $\sigma_{\text{cyto}} = 0.3 \text{ S/m}$ was used in the model, the E-field threshold amplitude required to electroporate the ER and granule membranes and the OMM was 4 MV/m, a value lower than the 8 MV/m determined experimentally. However, when the conductivity of the granule interior in the model was changed from 0.5 to 0.01 S/m, simulation results showed the E-field threshold amplitudes required to electroporate the granule membrane increased from 4 to 9 MV/m, a value that agreed closely with that observed in the experiments.

The effect of the organelle interior conductivity on the E-field threshold amplitude required to electroporate the organelle membrane was also predicted in another modeling study using a 4-ns pulse [116]. In that study, the conductivity of the liposome interior was varied and the E-field threshold required to electroporate the liposome membrane was determined. It was shown that a decrease in the conductivity of the liposome interior lead

to an increase in the threshold E-field amplitude required to porate the liposome membrane [116]. Together, these and our results highlight the importance of knowing accurately the dielectric properties of the different intracellular organelles in the model since changing their values affects the computed results tremendously.

As stated previously in Chapter 1, the ER, secretory granules and mitochondria represent the major Ca^{2+} sources in chromaffin cells. While NEPs have been shown to cause Ca^{2+} release from the ER in Jurkat, CHO and HL-60 cells [52-56], direct poration to Ca^{2+} has not been shown in the mitochondria [50,51]. Napotnik et al. (2012) reported that at least five 4-ns pulses applied at E-field amplitudes of 10 MV/m were required to cause inner mitochondrial membrane permeabilization in Jurkat cells as evidenced by a loss in mitochondrial membrane potential [50]. In addition, our modeling results predicted threshold E-field amplitudes greater than the experimentally determined threshold of 8 MV/m to cause electroporation of the IMM (Fig. 3.15). Because of the high E-field amplitudes required to electroporate mitochondrial membranes, we eliminated the possibility that NEPs permeabilize mitochondrial membranes to Ca^{2+} in chromaffin cells, and assumed that the remaining potential targets of NEPs were the ER and secretory granules.

3.4.2.3 Identifying the mechanism responsible for intracellular Ca^{2+} release

Several studies reported NEP-induced effects on intracellular membranes [52,53,56]. For example, one study reported that 60-ns pulses cause Ca^{2+} release from the ER through pores that form in the ER membrane in Jurkat cells as evidenced by an instantaneous increase in intracellular Ca^{2+} levels initiating from the poles side of the ER [52]. Another

study showed that exposing HL-60 cells to 60-ns duration pulses evoked rapid Ca^{2+} mobilization from the ER, which had similar kinetics to Ca^{2+} mobilization evoked by the purinergic agonist UTP. The authors suggested that the pulse and the agonist utilized the same Ca^{2+} channels (i.e. IP_3Rs and RyRs) present in intracellular membranes that caused Ca^{2+} release from internal stores [56]. Nevertheless, the authors did not exclude the possibility that Ca^{2+} could have been released through transient pores that formed in the intracellular membranes [56]. On the other hand, Tolstykh et al. (2013) reported activation of lipid signaling pathways inside the cell originating from effects on the plasma membrane evoked by a 600-ns pulse [58].

In chromaffin cells, we distinguished between these two possibilities by comparing the time course of the Ca^{2+} response evoked by an agonist to that evoked by a single 5-ns pulse. It was found that a brief application of the mixed nicotinic-muscarinic receptor agonist carbachol in the absence of extracellular Ca^{2+} caused Ca^{2+} release from the ER that was delayed by a few seconds (up to 5 s) from the time of application of the agonist (Fig. 3.10a). As stated previously, the lag in the cell response following application of carbachol was reported in other studies in chromaffin cells using agonists that acted through the breakdown of inositol lipids and was attributed to a requirement for the generation of a threshold level of IP_3 that would elicit Ca^{2+} release from intracellular stores [114,115]. On the other hand, when chromaffin cells were exposed to a single 5-ns pulse, at E-field amplitudes greater than 8 MV/m, the rise in intracellular Ca^{2+} was immediate and small in amplitude (Figs. 3.8a and 3.8b) compared to the one evoked by carbachol. These observations have led to the conclusion that a mechanism other than the activation of IP_3 pathways inside the cells is responsible for the NEP-induced Ca^{2+} release. We attributed

Ca²⁺ release to through nanopores that formed in the membranes of intracellular Ca²⁺-storing organelles.

In addition, an immediate increase in intracellular Ca²⁺ levels due to poration of internal membranes has been predicted by simulation studies in which release of intracellular Ca²⁺ from the ER was found to be instantaneous [118]. Our modeling results also indicated that nanopores form in intracellular membranes within a few nanoseconds during pulse application. Taken together, our modeling and experimental results support the reasoning that Ca²⁺ can be released immediately through nanopores that form in internal membranes.

3.4.2.4 Assessing the efficiency of intracellular membrane poration to increase intracellular Ca²⁺ levels

It was determined experimentally that the magnitude of intracellular Ca²⁺ release increases with E-field amplitude (Fig. 3.8c), consistent with the findings reported in other studies [54,55]. Iurii et al. (2013a) showed that when CHO cells were exposed to a single 60-ns pulse in the absence of extracellular Ca²⁺, intracellular Ca²⁺ levels increased linearly with increased E-field amplitude. When a critical level between 200 and 300 nM of Ca²⁺ was reached intracellularly, CICR occurred [54]. However, in chromaffin cells, even at double the E-field threshold amplitude found to cause intracellular membrane poration, the NEP was not efficient at causing a large Ca²⁺ release from internal stores.

In addition, we attribute the increase in intracellular Ca²⁺ levels with E-field amplitude to the increase in the number of pores formed in the membrane of intracellular organelles during pulse application. Our numerical modeling results correlate with this observation as

evidenced by the increase in the pore density when the amplitude of the applied E-field was increased (Fig. 3.13).

While the numerical model exhibited a saturation effect in the TMP and pore density once the E-field threshold amplitude causing significant electroporation was reached (Fig. 3.13), such a saturation effect was not observed experimentally (Fig 3.8c). On the contrary, Ca^{2+} release kept increasing up to 21 MV/m. The saturation obtained in the model was observed at the anodic pole of the membrane, however regions away from the poles could still not be sufficiently electroporated, and require higher E-field amplitudes to electroporate. Because 21 MV/m was the highest E-field amplitude achievable with our experimental setup, we could not verify whether a saturation effect will be observed at higher E-field amplitudes. These observations further confirm the inability of a single 5-ns pulse to efficiently porate the membranes of intracellular organelles.

3.5. Conclusions

The numerical and experimental work described in this chapter demonstrated that application of a single 5-6 ns electric pulse caused plasma membrane permeabilization at an E-field threshold of 4 MV/m, but twice this E-field amplitude was required to cause Ca^{2+} release from intracellular stores as a result of poration of intracellular membranes. Knowledge of these thresholds is essential for verifying that NEPs can alter neural cell excitability and cause Ca^{2+} influx that triggers exocytosis and catecholamine release without resulting in additional, unwanted effects on intracellular structures such as poration of intracellular membranes leading to Ca^{2+} release from internal stores.

While the modeling results agreed with the experimental findings with respect to the E-field threshold amplitudes required to permeabilize the plasma membrane, they disagreed with the experiments that demonstrated the need for high E-field amplitudes to cause Ca^{2+} release from intracellular stores. This discrepancy is addressed further in the next chapter.

In addition, this study has shown that Ca^{2+} release from intracellular stores is complex, as evidenced by the variability in the cell responses observed. The Ca^{2+} responses varied from small, single Ca^{2+} transients to spiky Ca^{2+} release that was localized to distinct regions of the cell. To our knowledge, these observations are novel and have not been reported in other cell types [54]. To follow up on these observations, more studies are needed, such as identifying the source from which intracellular Ca^{2+} is being released.

The following chapter is dedicated to identifying the internal organelle targeted by the NEP and to refining the numerical model by using, where possible, measured dielectric properties specific to chromaffin cells in order to obtain better agreement between the simulated and experimental results.

CHAPTER 4. Exposing Adrenal Chromaffin Cells to High Intensity, 5-ns Electric Pulses Causes Electroporation of the ER Membrane

4.1. Introduction

In the previous chapter it was shown that Ca^{2+} was released from intracellular stores in chromaffin cells following application of a single 5-6 ns pulse with an amplitude greater than 8 MV/m. This chapter focuses on identifying the source(s) of the Ca^{2+} that was being released using experimentation and further validation with numerical modeling. Since the ER is the primary target of NEPs in other cell types, we hypothesized that it is the primary target of NEPs in chromaffin cells as well. However, another potential target of NEPs in chromaffin cells is the secretory granules.

The experimental approach aimed at identifying the source of intracellular Ca^{2+} consisted of using pharmacological agents to deplete Ca^{2+} from the ER and assessing the effect of depletion on the Ca^{2+} responses following pulse application. To validate the experimental findings relative to the source(s) of intracellular Ca^{2+} , the 2D numerical cell model was refined by modeling a local region inside the cell, in addition to using realistic sizes for the chromaffin granules as well as their measured dielectric properties. The model was also used to further understand the requirement for high E-field amplitudes to electroporate the membranes of intracellular organelles.

4.2. Materials and methods

4.2.1 Chromaffin cell isolation, culturing and dissociation

Bovine chromaffin cells were isolated from the medulla of fresh adrenal glands using the method described by Waymire et al. (1993) [107]. Briefly, fresh adrenal glands were obtained from a local abattoir (Wolf Pack Meats, Reno, NV, USA). The outer cortex was removed by dissection and a perfusion catheter inserted in the adreno-lumbar vein of the medulla. To flush out red blood cells, the tissue was perfused with a $\text{Ca}^{2+}/\text{Mg}^{2+}$ -free Hank's balanced salt solution (HBSS) of the following composition: 137 mM NaCl, 5.37 mM KCl, 0.44 mM KH_2PO_4 , 0.54 mM Na_2HPO_4 , 4.17 mM NaHCO_3 , 5.55 mM D-Glucose, 5 mM HEPES, phenol red (0.001%) and 0.02% bovine serum albumin (BSA), pH 7.2. The medulla was then digested by perfusing it via the adreno-lumbar vein with HBSS containing collagenase B (0.05%) and CaCl_2 (50 μM). Once digestion was complete, the swollen tissue was gently agitated to obtain single cells, which were subjected to a sequence of four centrifugation steps to remove debris and any remaining red blood cells. After the final centrifugation step, the cells were diluted to a final concentration of 4×10^5 cells/ml in Ham's F-12 medium supplemented with 10 % bovine calf serum, 100 U/ml penicillin, 100 $\mu\text{g}/\text{ml}$ streptomycin, 0.25 $\mu\text{g}/\text{ml}$ fungizone, and 6 $\mu\text{g}/\text{ml}$ cytosine arabinoside, placed into tissue culture flasks and incubated for 5.5 hours at 36.5°C under a humidified atmosphere of 5% CO_2 . During this incubation, non-chromaffin cells present in the cell mixture adhered to the bottom of the tissue culture flask whereas the chromaffin cells remained in suspension. At the end of the differential plating step, the cells were collected from each flask, distributed into 60 mm Petri dishes at a density of 1×10^5 cells/ml

and maintained in suspension culture in the supplemented Hams' F12 medium at 36.5°C under a humidified atmosphere of 5% CO₂. Cells were used up until 3 weeks in culture.

For all experiments, the large aggregates of cells that form in suspension culture were dissociated into single isolated cells with the protease dispase [108]. Briefly, the enzyme was added directly to a dish of cells for a minimum of 6 hours. After collecting the cells by centrifugation, cells were incubated at 37°C in Ca²⁺/Mg²⁺-free HBSS lacking KH₂PO₄, NaHCO₃ and phenol red. After 10 min, the incubation was interrupted and the cells were gently triturated to facilitate dissociation. The incubation/trituration steps were repeated 4 times. Once cell aggregates were fully dissociated, the cells were plated onto fibronectin-coated 35 mm glass bottom dishes (inner glass diameter: 20 mm). Cells were used for a period not exceeding 2 days after attachment. All experiments were carried out at room temperature (22-25°C).

4.2.2 Fluorescence imaging of intracellular Ca²⁺ levels

Cells were incubated with a cell permeant Ca²⁺-sensitive fluorescent indicator Calcium Green-1-AM (1 μM; 480/535 nm) for 45 min at 37°C in a balanced salt solution (BSS) with the following composition: 145 mM NaCl, 5 mM KCl, 1.2 mM NaH₂PO₄, 2 mM CaCl₂, 1.3 mM MgCl₂, 10 mM glucose, 15 mM HEPES and 0.1% BSA, pH 7.4. After incubation, cells were washed twice with BSS lacking BSA and placed on the stage of a Nikon TE2000 epifluorescence microscope equipped with a 100X objective. For experiments conducted in the absence of extracellular Ca²⁺, the BSS lacked Ca²⁺ and contained 1 mM EGTA. Fluorescence images of the cells, which were obtained before, during and after stimulus application, were captured by an iXonEM + DU-897 EMCCD

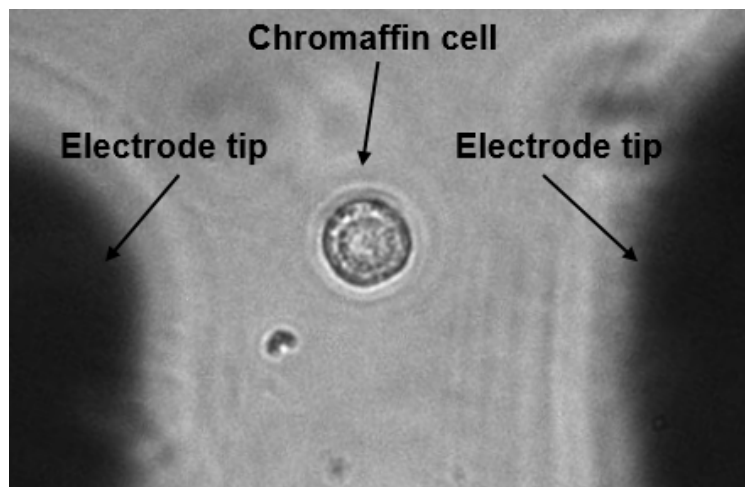
camera (Andor Technology Ltd., Belfast, UK) using the open source microscopy software Micro-Manager (version 1.4). The exposure time of the camera was set to 100 ms. Continuous baseline Ca^{2+} fluorescence of the cells was monitored 10 s prior to stimulus application and continued for 20-30 s after the stimulus. Sequences were analyzed using the public-domain image processing program ImageJ. The change in fluorescence intensity (ΔF) of the cells was calculated by subtracting the background fluorescence from the fluorescence of the cell ($\Delta F = F_{\text{cell}} - F_{\text{background}}$). ΔF was then normalized to the fluorescence intensity value (F_0) at the time when the stimulus was applied ($\Delta F/F_0$). Bright field images were obtained before and after the applied stimulus.

For experiments in which drugs were applied by perfusion, cells were attached to the inner well (diameter of 10 mm) of glass bottom dishes and the various agonists and blockers, dissolved in BSS, were continuously delivered to the cells using a six-channel perfusion valve control system (Warner Instruments, Hamden, CT). A silicone Petri dish insert (Bioscience Tools, San Diego, CA, USA) that was adhered to the bottom of the dish provided solution exchange inside the area where the cells were located within 30 to 60 s. Cells were perfused at a rate of 0.7-0.9 ml/min.

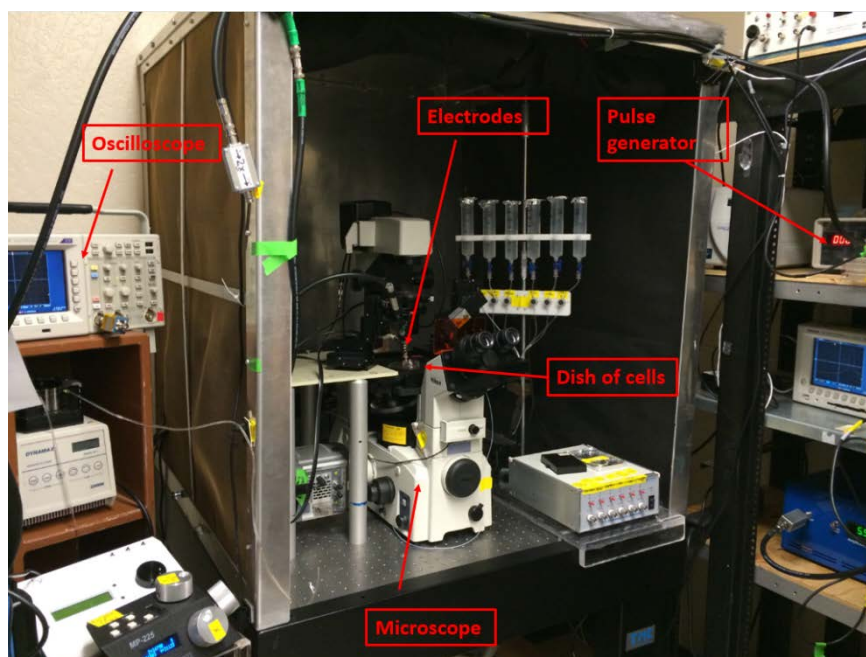
Continuous baseline Ca^{2+} fluorescence of the cells was monitored during perfusion of the stimulus and continued up to 5 min afterwards. Caffeine, ryanodine, CPA and carbachol were used at concentrations of 50 mM, 1 μM , 30 μM and 500 μM , respectively. Because of the high caffeine concentration, the caffeine solution was prepared in NaCl-reduced Ca^{2+} -free BSS containing 1 mM EGTA to maintain isotonicity and avoid any osmotic effect on the cells. Solutions of ryanodine, CPA and carbachol were prepared in Ca^{2+} -free BSS containing 1 mM EGTA.

4.2.3 NEP exposure

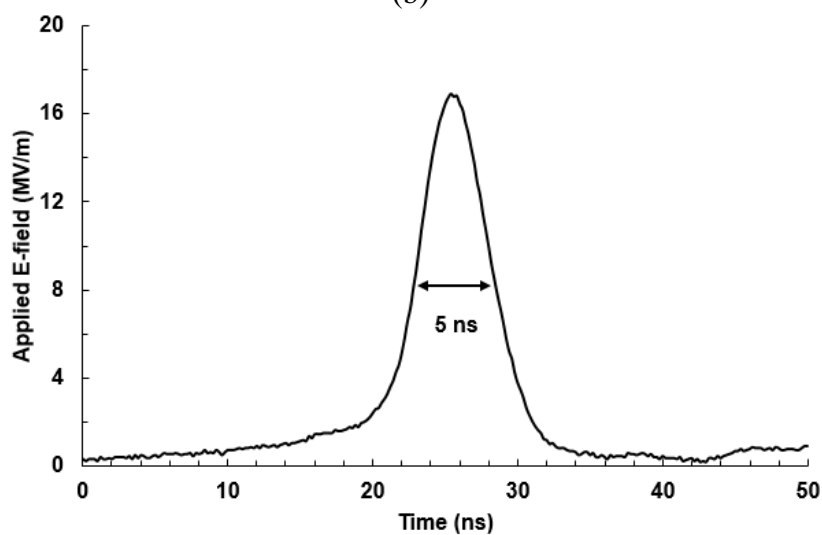
A 5-ns pulse was applied to a cell by means of two cylindrical gold-plated tungsten rod electrodes (127 μm diameter) spaced 100 μm apart. The tips of the electrodes were immersed in the BSS bathing the cells and placed 40 μm above the bottom of the dish, with the imaged cell located at the center of the gap between the electrode tips (Fig. 4.1a). The entire experimental setup is shown in Fig. 4.1b. Single pulses with amplitudes that produced electric fields (E-fields) of 17 MV/m (see the subsection below for the E-field calculation) at the location of the cell were generated by a custom-fabricated nanosecond pulse generator (Transient Plasma Systems, Torrance, CA). Delivery of pulses was triggered externally by a program written in LabVIEW, and pulse traces (Fig. 4.1c) captured with a TDS 3102C oscilloscope (Tektronix, Beaverton, OR, USA). In all experiments, a cell was exposed to the E-field only once.



(a)



(b)



(c)

Fig. 4.1. Details of the NEP exposure system. (a) Photomicrograph of an attached cell showing the electrode tips which are positioned $40\ \mu\text{m}$ above the bottom of the dish. (b) Photograph of the actual experimental setup used in fluorescence imaging experiments. (c) Representative waveform of a 5-ns pulse applied in experiments to chromaffin cells. The pulse duration corresponds to the width at half maximum.

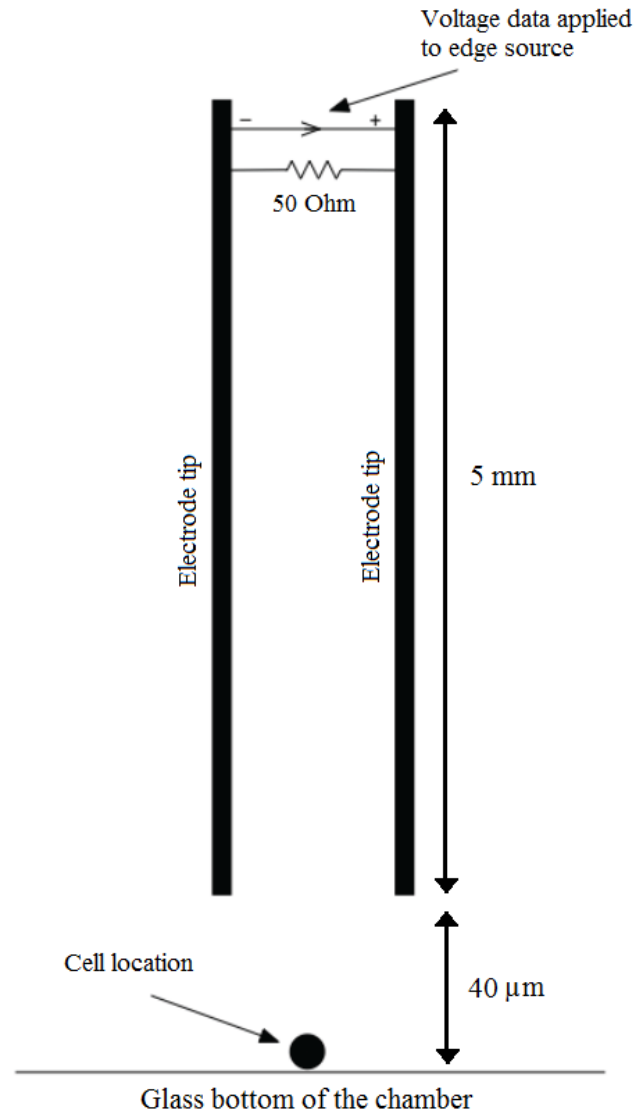
4.2.3.1 *Numerical computation of the E-field distribution in the vicinity and at the location of the cell*

The E-field distribution in the vicinity and at the location of the cell were computed using the commercially available Finite-Difference Time-Domain software package SEMCAD X (version 14.8.5, SPEAG, Zurich, Switzerland). Briefly, experimental voltage trace data, recorded on an oscilloscope, were collected from several NEP traces, averaged together and then used as input excitation in SEMCAD X to compute the E-field distribution as follows: A three-dimensional (3D) geometric model was created in SEMCAD X to represent the portion of the exposure system that included the exposed ends of the electrode tips, the 50 Ω matching resistance (matching the characteristic impedance of the electrodes to that of the cabling and pulse delivery system), the BSS, and the glass chamber representing the glass bottom dish onto which the cells are attached (Fig. 4.2a). The entire exposure system was not modeled because of computational limitations. The electrode tips were positioned 40 μm above the chamber floor and were surrounded by BSS, as in actual experiments.

A SEMCAD simulation* was then performed wherein the averaged voltage data of the pulse was fed to the edge source which supplies the pulse, located at the top of the electrodes as shown in Fig. 4.2a. The E-field at the location of the cell (Fig. 4.2b) was computed and detected by a point sensor placed at the cell location.

* SEMCAD X simulations were performed by Dr. Jihwan Yoon and Robert Terhune, Department of Pharmacology, University of Nevada Reno, and the results were used in this dissertation to calculate the E-field amplitudes applied to cell during experiments.

A conversion factor was obtained by dividing the peak E-field detected by the point sensor by the peak voltage applied to the edge source. This conversion factor was used to calculate the E-field amplitude delivered to the cells, by multiplying the peak voltage measured during experiments by the conversion factor obtained from the simulations.



(a)

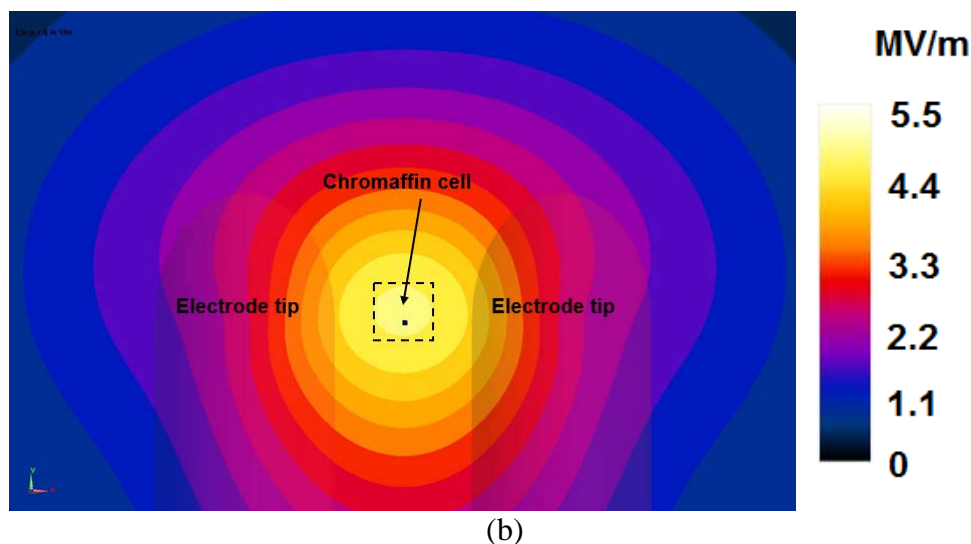


Fig. 4.2. Details of the SEMCAD X FDTD simulations. (a) Schematic showing the geometry used in the FDTD simulations. The point sensor used to detect the E-field computed in the simulations is placed at the cell location. (b) E-field distribution in the vicinity and at the location of the cell when a voltage of 2700 V was applied. The dotted box represents the region over which a cell can be located in experiments.

4.2.4 Reagents

Calcium Green-1-AM was purchased from Molecular Probes (Eugene, OR, USA), Ham's F-12, dispase II and the antibiotic-antimycotic were purchased from Gibco Laboratories (Grand Island, NY, USA), bovine calf serum was purchased from Gemini Bio-products (West Sacramento, CA, USA), collagenase B was purchased from Roche Diagnostics (Indianapolis, IN, USA), carbachol, caffeine and CPA were purchased from Sigma-Aldrich (St. Louis, MO, USA), and ryanodine was purchased from AG Scientific Inc. (San Diego, CA, USA). All other chemicals and reagents were reagent grade and purchased from standard commercial sources.

4.2.5 2D model of chromaffin cell organelles

A localized 2D geometric model of intracellular Ca^{2+} -storing organelles in chromaffin cells exposed to a single 5-ns pulse was constructed in Matlab (2015a, Mathworks). Computations were performed based on the meshed transport network method (MTNM) developed by Smith and Weaver (2008) [40]. The electrical response of the organelles was based on the asymptotic model of electroporation developed by Neu and Krassowska (1999) [34]. Below is a description of the geometry and parameters used in the model.

4.2.5.1 Model geometry and simulation

As previously stated, it is hypothesized that the ER is the primary target of NEPs in chromaffin cells. However, secretory granules also represent another potential target. Modeling realistic granule sizes around the ER required the use of a localized 2D model in which only intracellular organelles were considered.

The localized model geometry (Fig. 4.3) consisted of a circular structure of radius $r_{\text{ER}} = 300$ nm representing the ER, surrounded by 6 secretory granules of realistic radius $r_{\text{gran}} = 150$ nm each [88]. All organelles were placed inside a bounding box (i.e. system boundary) of dimensions $15 \mu\text{m} \times 15 \mu\text{m}$ and were represented by single membrane structures that had a thickness of $d_m = 5$ nm. The secretory granule membranes were assigned a resting potential of -70 mV, a value typical for chromaffin granules [119]. The pulse was applied by means of idealized planar electrodes placed at $x = -7.5 \mu\text{m}$ (anode) and $x = 7.5 \mu\text{m}$ (cathode). The E-field was calculated by dividing the potential difference between the electrodes by the distance between the electrodes. The averaged voltage traces of the pulse captured during experiments were implemented in the model.

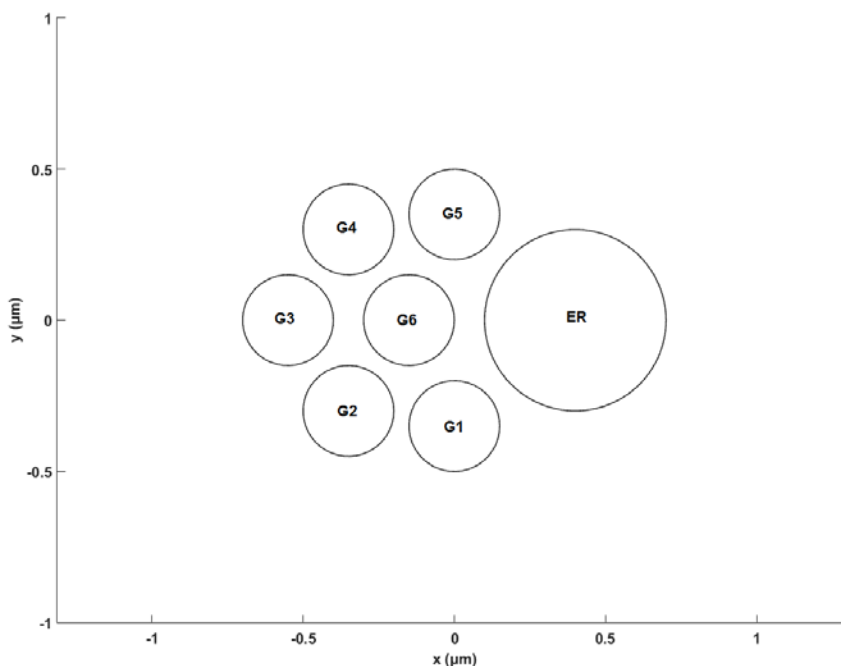


Fig. 4.3. Zoomed-in view of the model geometry illustrating the different organelles. A circular structure representing the ER ($r_{ER} = 300$ nm) was placed at $(0.4 \mu\text{m}, 0)$ and six secretory granules (G1 to G6; $r_{gran} = 150$ nm) were placed around the ER at $(0, -0.35 \mu\text{m})$, $(-0.35 \mu\text{m}, -0.3 \mu\text{m})$, $(-0.55 \mu\text{m}, 0)$, $(-0.35 \mu\text{m}, 0.3 \mu\text{m})$, $(0, 0.35 \mu\text{m})$ and $(-0.15 \mu\text{m}, 0)$, respectively.

After constructing the geometry, a triangular mesh (Fig. 4.4a) was generated using the mesh generation algorithm developed by Persson and Strang [94]. During mesh generation, nodes were fixed along the membranes. The triangular elements in the mesh varied in size, starting from a fine mesh in and around the membranes and expanding in size as the system boundary was approached. The ER membrane and each secretory granule membrane had 90 and 45 membrane points, respectively. The meshing algorithm required that the node spacing for all membranes be the same. Because of the small size of the granules, the cell was not added to the geometry because it would require an extremely large number of points on its membrane, thus increasing the amount of computation and data storage

beyond the capacity of computers available in our laboratory. For this reason only the intracellular Ca^{2+} -storing organelles that are targets of NEPs were modeled.

For times that are much smaller than the membrane charging time, equation (1) in Chapter 1 simplifies to:

$$V_m(t) = 1.5 E \cos\theta \frac{d_m}{\epsilon_m \epsilon_0} \left(\frac{1}{\rho_i + \rho_e/2} \right) t \quad (1)$$

where V_m is the TMP, E the amplitude of the external E-field, θ the angle between the normal to the membrane and the direction of the E-field, d_m the membrane thickness, ϵ_m the membrane permittivity, ϵ_0 the free space permittivity, ρ_i and ρ_e the resistivities of the intracellular and extracellular media, respectively. The TMP becomes independent of cell size and depends on the amplitude of the applied E-field and on the electrical properties used (assuming a fixed membrane thickness $d_m = 5$ nm). Although this equation was derived for a cylindrical cell, the size-independence also applies to irregular shaped cells and organelles [109]. Experiments conducted using NEPs also verified this assumption [70]. For the ultrashort 5-ns duration pulses used in this study, it was deemed adequate to represent the ER by a circle, neglecting the irregular shape of the ER in chromaffin cells.

As described in Chapter 2, the VCs (Fig. 4.4b) represented the small volumes into which the entire domain was discretized. Parallel RC circuits were placed between each pair of adjacent nodes in the geometry and the circuit nodes approximated the behavior of each VC with which they were associated. R and C values were computed based on the electrical properties assigned to each region (i.e. conductivity and permittivity) and on the geometrical parameters obtained from the mesh (i.e distance between nodes and length of VC edges).

Matlab was used to compute all geometrical parameters and circuit components (e.g. R and C), and create netlists containing all node elements and connections in the circuits. Netlists were then imported into a circuit simulation software package LT SPICE IV (Linear Technology, Milpitas, CA, USA) where the model was simulated. The generated data (i.e. node voltages and currents) were exported back into Matlab for plotting and analysis of the results.

4.2.5.2 *Model electrical parameters*

We have shown in the previous chapter that depending on the electrical parameters used in the 2D cell model, the simulation results varied significantly and affected the interpretation and validation of the experimental findings. To obtain better agreement between the experimental and modeling results with respect to the high E-field threshold amplitudes required to porate intracellular membranes, it was essential to use, where possible, electrical parameters that were specific to chromaffin cells. As mentioned in Chapter 2, chromaffin granule dielectric properties (i.e. granule interior conductivity and granule membrane permittivity) were measured using microfluidic impedance spectroscopy (manuscript in preparation). These measured dielectric properties were incorporated into the current numerical model and a parametric study was conducted for the conductivity of the ER interior (σ_{ERin}). This parameter was chosen to be changed since σ_{ERin} is unknown and modeling studies conducted by Retelj et al. (2013) and Kotnik and Miklavčič (2006) showed that depending on the conductivity of the organelle interior, the E-field threshold amplitude required to porate the organelle membrane varies significantly [26,116]. The electrical parameters used in the model are defined in Table 4.1.

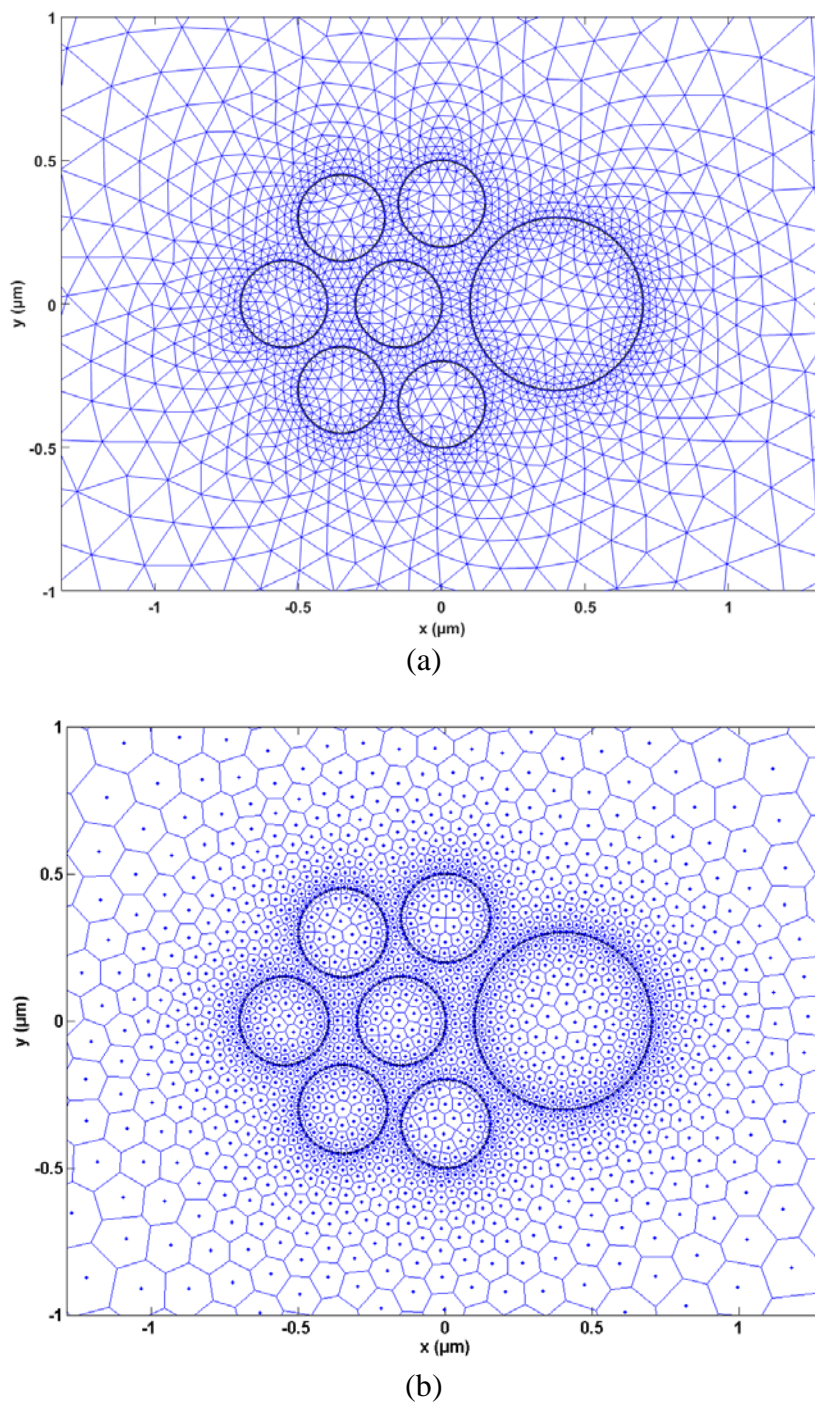


Fig. 4.4. Mesh and VCs of the localized 2D geometric model. The mesh is shown in (a) and the VCs in (b). The mesh had 2707 nodes, 5400 triangles and 8106 edges, and a 21 nm membrane node spacing. The relationship between the mesh and associated VCs is described in Chapter 2.

Table 4.1: Electrical parameters used in the 2D model of chromaffin cell organelles.

<u>Conductivity (S.m⁻¹)</u>	<u>Value</u>
Cytoplasm ^a	0.3
ER membrane ^a	8.3 x 10 ⁻¹⁰
Granule membrane ^a	8.3 x 10 ⁻¹⁰
ER interior ^b	0.01-0.5
Granule interior ^c	0.3
<u>Relative permittivity</u>	
Cytoplasm ^a	80
ER membrane ^a	5
Granule membrane ^c	30
ER interior ^a	80
Granule interior ^a	80

^a Same values used as in Chapter 3.

^b Conductivity of the ER interior was varied in the parametric study.

^c Granule interior conductivity and granule membrane permittivity were determined by microfluidic impedance spectroscopy (Chapter 2).

4.2.5.3 *Asymptotic model of electroporation*

The electrical response of the cell subjected to the NEP was modeled using the asymptotic model of electroporation [34]. This model assumes that pores do not expand for nanosecond duration, high amplitude electric pulses [20]. The assumption of a constant pore size can safely be used in this study since the 5-ns duration pulse used in the experiments is too short to cause pore expansion.

Pore dynamics are defined in the simplified form of the Smoluchowski equation, which is an ordinary differential equation given by [93]:

$$\frac{dN(t)}{dt} = \alpha e^{\left(\frac{V_m(t)}{V_{ep}}\right)^2} \left(1 - \frac{N(t)}{N_0} e^{-q\left(\frac{V_m(t)}{V_{ep}}\right)^2} \right) \quad (2)$$

where N is the local pore density, α the pore creation rate coefficient, V_m the transmembrane potential, V_{ep} the characteristic voltage of electroporation, N_0 the

equilibrium pore density in the nonelectroporated membrane, and q an electroporation coefficient.

Modeling the membranes required the incorporation of the nonlinear changes in membrane conductance due to electroporation. In addition to the passive RC circuit that exists between each pair of nodes that span the membrane, a current source i_p representing the current through pores was added to the membrane model (Fig. 4.5a). The current through pores in a small area A_m of the membrane was calculated from the conductance per pore G_p , the pore density N , and the TMP V_m by:

$$i_p(t) = G_p(V_m)N(t)A_m V_m(t) \quad (3)$$

The TMP was determined by the voltage difference across the membrane, and the conductance per pore, representing the increase in membrane conductivity due to electroporation, was calculated from:

$$G_p(V_m) = \sigma_p \frac{\pi r_m^2}{d_m} \frac{e^{v_m-1}}{\frac{\omega_0 e^{\omega_0 - \eta v_m - \eta v_m}}{\omega_0 - \eta v_m} e^{v_m} - \frac{\omega_0 e^{\omega_0 + \eta v_m + \eta v_m}}{\omega_0 + \eta v_m}} \quad (4)$$

where σ_p is the pore conductivity, r_m the fixed pore radius, d_m the membrane thickness, ω_0 the energy barrier inside a pore, η the relative entrance length of a pore, and v_m the dimensionless TMP given by:

$$v_m = \frac{V_m q e}{kT} \quad (5)$$

$q_e = 1.6 \times 10^{-19}$ C is the charge of an electron, $k = 1.38 \times 10^{-23}$ J/K the Boltzmann constant, and T the absolute temperature.

The pore density N was calculated by solving equation (5) using the subcircuit shown in Fig. 4.5b. In this subcircuit, the voltage $N(t)$ across the capacitor C_N is given by:

$$\frac{dN(t)}{dt} = \frac{i_N(t)}{C_N} \quad (6)$$

where $C_N = 1/\alpha$ and i_N , representing the current flowing into the capacitor, is given by:

$$i_N(t) = e^{\left(\frac{V_m(t)}{V_{ep}}\right)^2} \left(1 - \frac{N(t)}{N_0} e^{-q\left(\frac{V_m(t)}{V_{ep}}\right)^2} \right) \quad (7)$$

When the sum of the currents flowing into the node is positive, a positive current flows into the capacitor, the capacitor charges and the voltage $N(t)$ at the node increases, thus creating pores. Otherwise, when the sum of the currents flowing into the node is negative, a negative current flows into the capacitor, the capacitor discharges and the voltage $N(t)$ at the node decreases, thus destroying pores [93]. The electroporation parameters used in equations (2)-(7) were taken from [93,96] and are defined in Table 4.2.

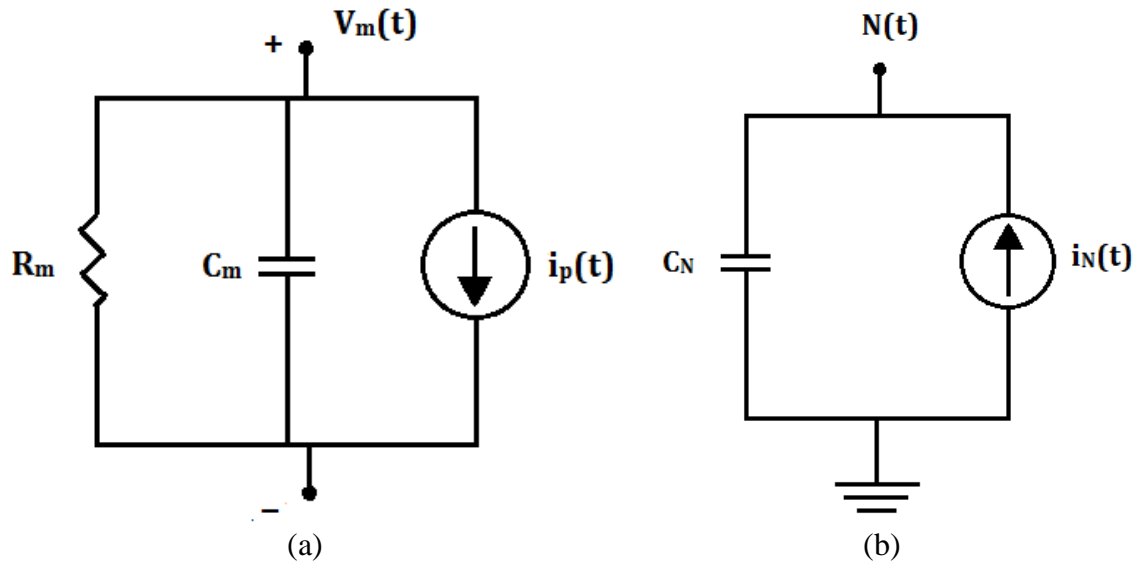


Fig. 4.5. Equivalent electrical circuit for the membrane. (a) Resistors R_m and capacitors C_m were placed between each pair of nodes spanning the membrane, in addition to the current i_p through pores. (b) The pore density subcircuit associated with each membrane circuit was used to solve the pore dynamics equation (2).

Table 4.2: Electroporation parameters used in the 2D model of chromaffin cell organelles [93,96].

<u>Parameter</u>	<u>Value</u>
Pore creation rate coefficient (α)	$1 \times 10^9 \text{ m}^{-2} \text{ s}^{-1}$
Characteristic voltage of electroporation (V_{ep})	0.258 V
Electroporation coefficient (q)	2.46
Equilibrium pore density (N_0)	$1.5 \times 10^9 \text{ m}^{-2}$
Pore radius (r_m)	0.8 nm
Pore energy barrier (ω_0)	2.65 kT
Conductivity of aqueous solution in pores (σ_p)	1.3 S.m^{-1}
Pore relative entrance length (η)	0.15
Absolute temperature (T)	295 K

4.3. Results

4.3.1 Experimental findings

Pharmacological approaches were used to identify the source of intracellular Ca^{2+} released in response to a single 5-ns pulse. For these experiments, the conditions for partially and fully depleting ER Ca^{2+} stores were established and the Ca^{2+} response to a pulse delivered at 17 MV/m was assessed under both conditions in the absence of extracellular Ca^{2+} . At this pulse amplitude, 91% of the cells tested responded to a pulse by undergoing a small but measurable rise in intracellular Ca^{2+} that varied in amplitude from cell to cell (Section 3.3.1.1).

4.3.1.1 *Spontaneous fluctuations in intracellular Ca^{2+} levels ($[\text{Ca}^{2+}]_i$) do not occur in chromaffin cells in the absence of extracellular Ca^{2+}*

Bovine chromaffin cells are known to undergo spontaneous action potential firing that causes Ca^{2+} influx through VGCCs [120,121]. Using fluorescence imaging of $[\text{Ca}^{2+}]_i$, previous studies by our research group also reported that spontaneous Ca^{2+} transients occur in chromaffin cells in the presence of extracellular Ca^{2+} [92]. However, in the absence of extracellular Ca^{2+} , spontaneous fluctuations in $[\text{Ca}^{2+}]_i$ have not been reported in cells derived from the bovine species, even though some studies reported that chromaffin cells derived from other species (e.g. mouse, rat and human) undergo spontaneous Ca^{2+} transients when Ca^{2+} was absent in the extracellular solution [122].

The need to distinguish between spontaneous intracellular Ca^{2+} activity from pulse-induced release of Ca^{2+} from intracellular stores prompted us to monitor $[\text{Ca}^{2+}]_i$ in resting cells in the absence of extracellular Ca^{2+} . For this determination, fluorescence intensity was

monitored continuously for 40 s in a total of thirty cells derived from two cell preparations. None of the cells showed any detectable alteration in $[Ca^{2+}]_i$ and a representative fluorescence trace is shown in Fig. 4.6. These results indicate that intracellular Ca^{2+} responses that occur following application of a pulse would be attributed to the pulse itself and not to spontaneous release of Ca^{2+} from intracellular stores.

4.3.1.2 *The characteristics of Ca^{2+} release from internal stores evoked by a 5-ns pulse differed from that evoked by a receptor agonist*

In Chapter 3 it was shown that exposing chromaffin cells to the receptor agonist carbachol in the absence of extracellular Ca^{2+} caused a delayed increase in $[Ca^{2+}]_i$, that was attributed to IP_3 generation. In the experiments described in this chapter, carbachol was therefore used as a control to test for IP_3 -sensitive store depletion.

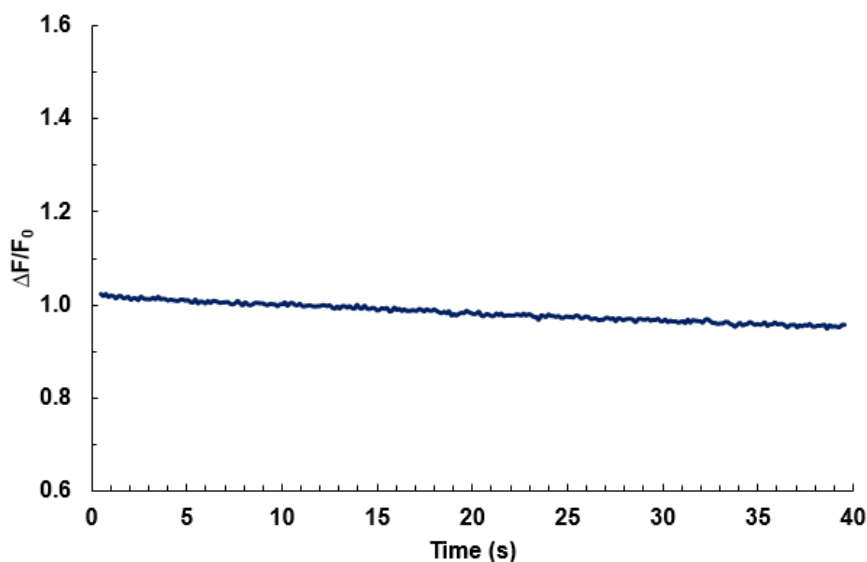


Fig. 4.6. Representative fluorescence Ca^{2+} trace in chromaffin cells at rest in the absence of extracellular Ca^{2+} .

When carbachol (500 μM) was applied to cells via perfusion in the absence of extracellular Ca^{2+} , Ca^{2+} release from intracellular stores occurred as a single peak (Fig. 4.7) which resembled that evoked by carbachol using a pressure ejection pipette (Fig. 3.7a), with the exception that the responses were greater in amplitude due to the longer presence of the agonist. The amplitudes of the Ca^{2+} transients varied from 1.6 to 2.6 (2.15 ± 0.48 S.D., $n = 4$ cells).

In contrast, exposing chromaffin cells in the absence of extracellular Ca^{2+} to a single 5-ns pulse at an E-field amplitude of 17 MV/m caused release of Ca^{2+} from intracellular stores that was characterized by three distinct patterns (Fig. 4.8). These patterns are similar to those shown in Fig. 3.8b for 19 MV/m. Out of a total of 30 cells, 17 cells exhibited a single short Ca^{2+} transient (< 10 s) (Fig. 4.8, red trace), 4 cells showed a single, longer-lived Ca^{2+} transient (> 10 s) (Fig. 4.8, blue trace), and the remaining 9 cells revealed Ca^{2+} responses that were spiky (Fig. 4.8, green and orange traces). Such spiking activity was not observed in any of the cells exposed to carbachol. The amplitudes of the Ca^{2+} transients, which were measured immediately when the pulse was applied, varied from 1.06 to 1.35 (1.15 ± 0.07 S.D., $n = 30$ cells).

4.3.1.3 *Depletion of ER Ca^{2+} stores with caffeine did not abolish pulse-induced Ca^{2+} release from intracellular stores*

As discussed in the Introduction, Ca^{2+} can be released from the ER either via the Ca^{2+} -gated Ca^{2+} channels, also known as ryanodine receptors (RyR), or via IP_3 -gated channels, also known as IP_3 -receptors (IP_3R) [123-126].

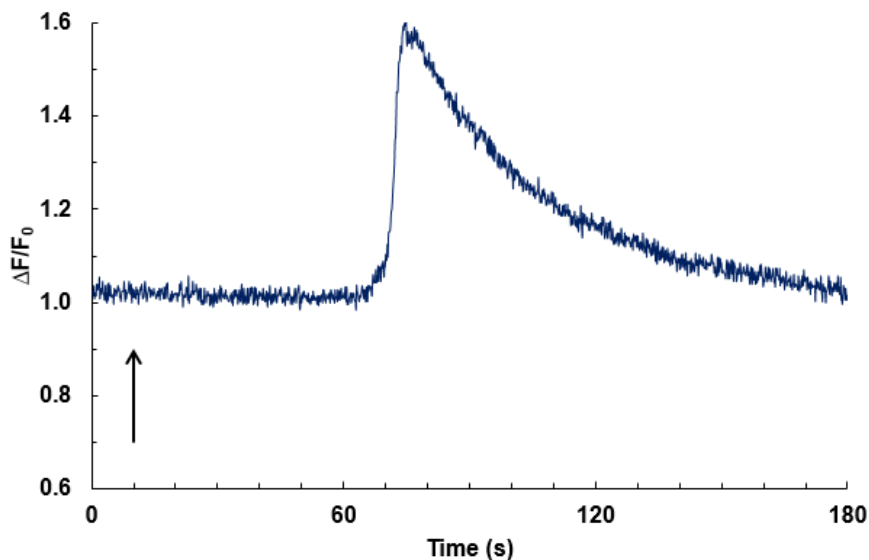


Fig. 4.7. Representative Ca^{2+} transient evoked by continuous application of carbachol via perfusion in the absence of extracellular Ca^{2+} . $\Delta F/F_0$ was calculated by subtracting the background fluorescence from the fluorescence of the cells and normalizing it to the fluorescence intensity value at the time when carbachol ($500 \mu\text{M}$) was applied. The arrow indicates when perfusion with carbachol was initiated.

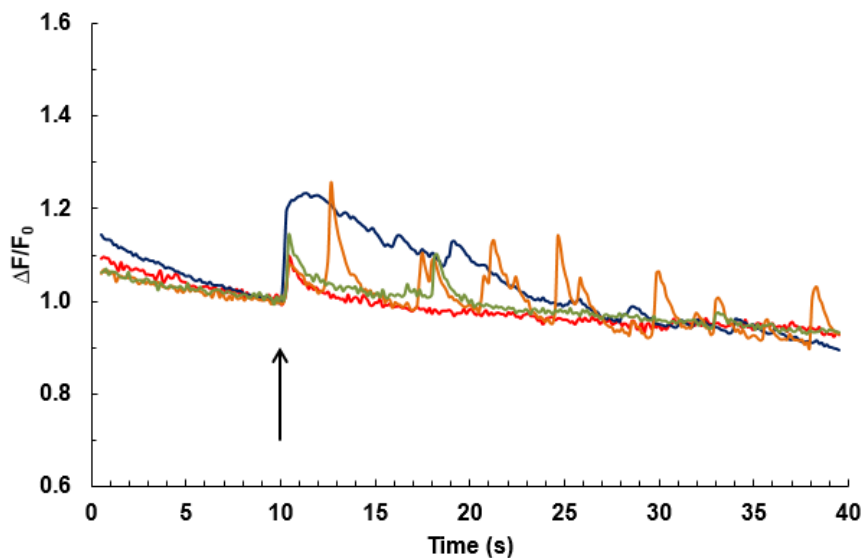
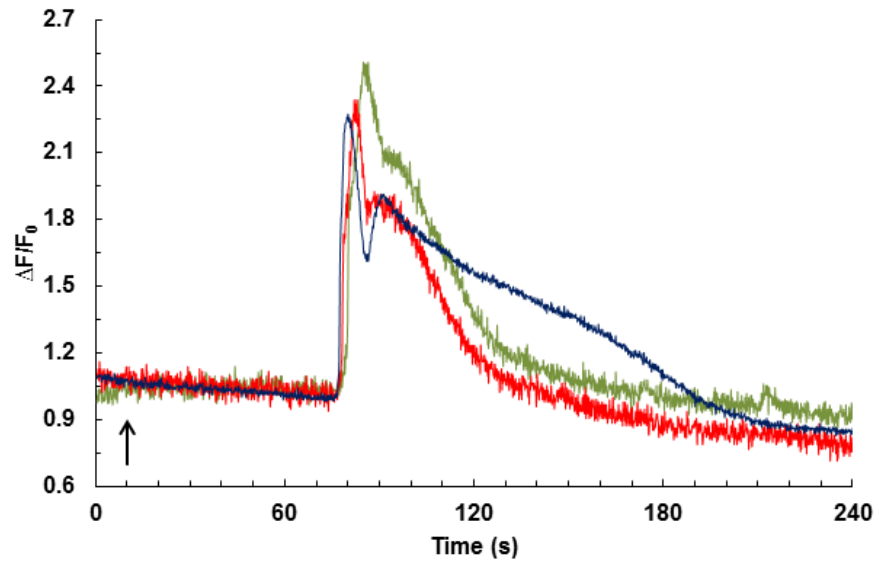


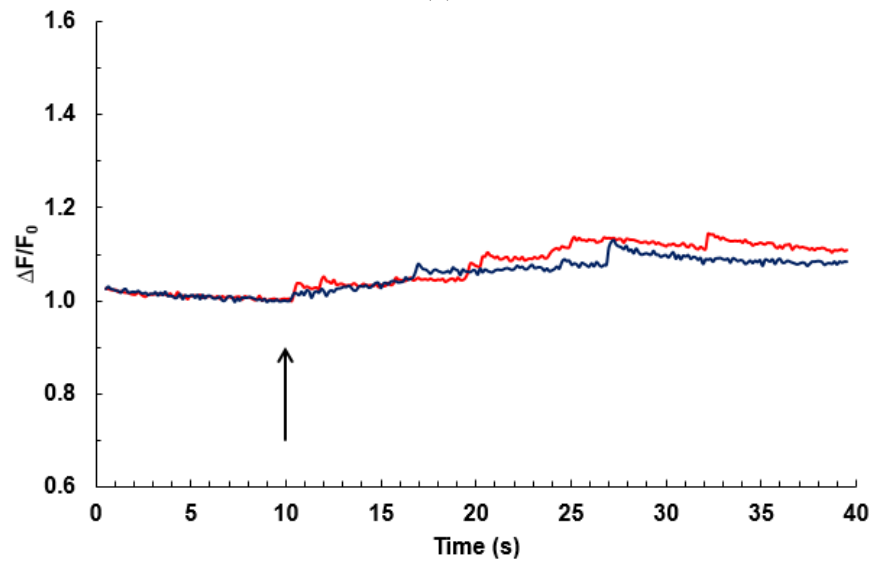
Fig. 4.8. Representative intracellular Ca^{2+} responses of chromaffin cells exposed to a single 5-ns pulse applied at an E-field amplitude of 17 MV/m in the absence of extracellular Ca^{2+} . $\Delta F/F_0$ was calculated by subtracting the background fluorescence from the fluorescence of the cells and normalizing it to the fluorescence intensity value at the time when the pulse was applied (arrow).

The first series of experiments examined the effect of depleting ryanodine-sensitive stores with caffeine, a RyR agonist. The concentration of caffeine that was used in these experiments, 50 mM, has been shown to be maximally effective at depleting these ER stores in chromaffin cells [127-129]. As shown in Fig. 4.9a, treating cells with 50 mM caffeine caused a rapid and transient increase in $[Ca^{2+}]_i$ that was due to Ca^{2+} release from the ER. Depending on the cell, the Ca^{2+} transients lasted from 45 to 90 s, and the amplitude of the rise in $[Ca^{2+}]_i$ varied from 1.3 to 2.5 (2.12 ± 0.37 S.D., $n = 10$ cells). Most of the cells (9 of 10 cells) showed two discernable peaks, which is consistent with the findings of Stauderman et al. (1991) [130]; only one cell showed a Ca^{2+} transient comprised of a single peak (not shown).

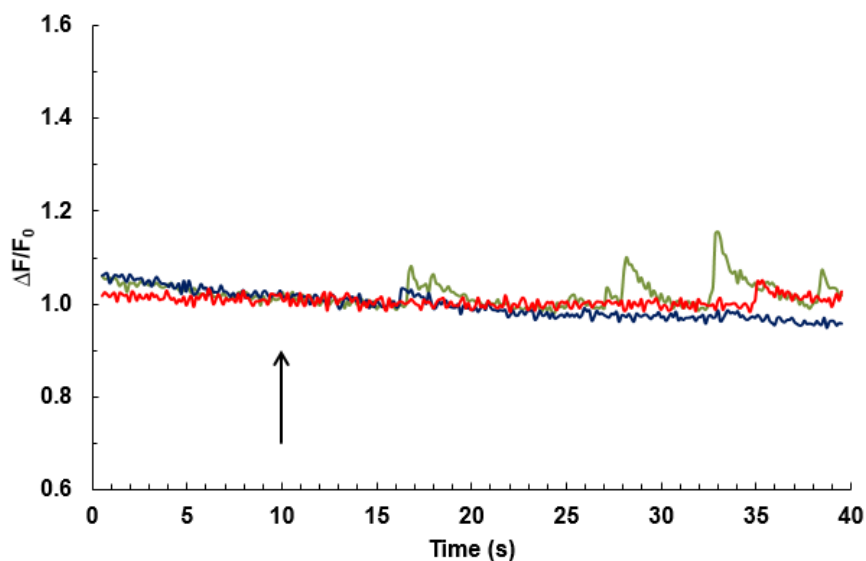
When chromaffin cells were exposed to a single 5-ns, 17 MV/m pulse following pretreatment with caffeine, Ca^{2+} responses were abolished in 20 out of 43 cells. Of the 23 cells that responded to the pulse, 7 cells showed an immediate release of Ca^{2+} that gradually increased in amplitude with time (Fig. 4.9b) and 16 cells showed a delayed release of Ca^{2+} (Fig. 4.9c) that varied from a single Ca^{2+} transient to multiple (i.e., spiky) Ca^{2+} transients. The later responses were attributed to a delayed effect of the pulse on the cells. Overall, the characteristics of these responses differed from those observed in cells in which ryanodine-sensitive ER stores were replete with Ca^{2+} .



(a)



(b)



(c)

Fig. 4.9. NEP-evoked Ca^{2+} responses in chromaffin cells in the presence of caffeine and absence of extracellular Ca^{2+} . (a) Representative Ca^{2+} transients following application of caffeine (50 mM) via perfusion. The arrow indicates the time when perfusion with caffeine was initiated. The traces shown in (b) and (c) are typical of immediate responses and delayed responses, respectively, observed in cells exposed to a single 5-ns duration pulse applied at E-field amplitudes of 17 MV/m. $\Delta F/F_0$ was calculated by subtracting the background fluorescence from the fluorescence of the cells and normalizing it to the fluorescence intensity value at the time when the pulse was applied (arrow).

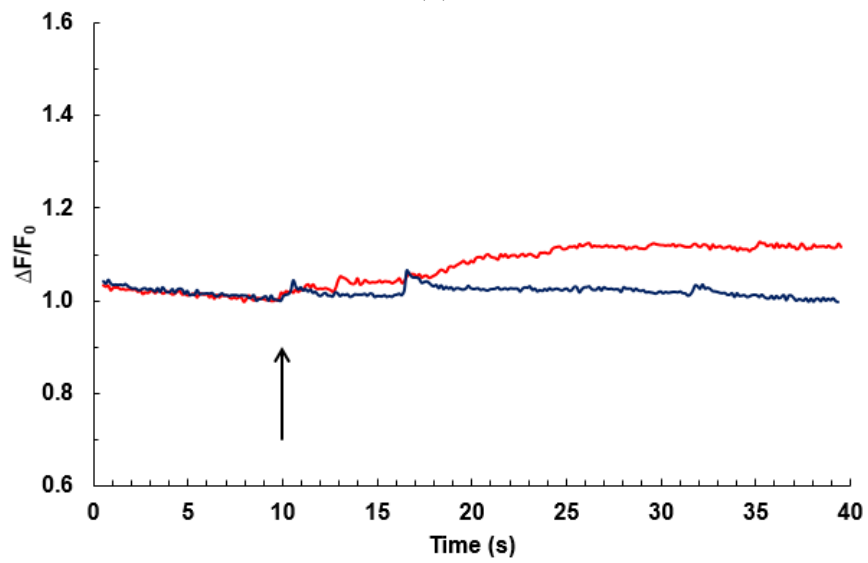
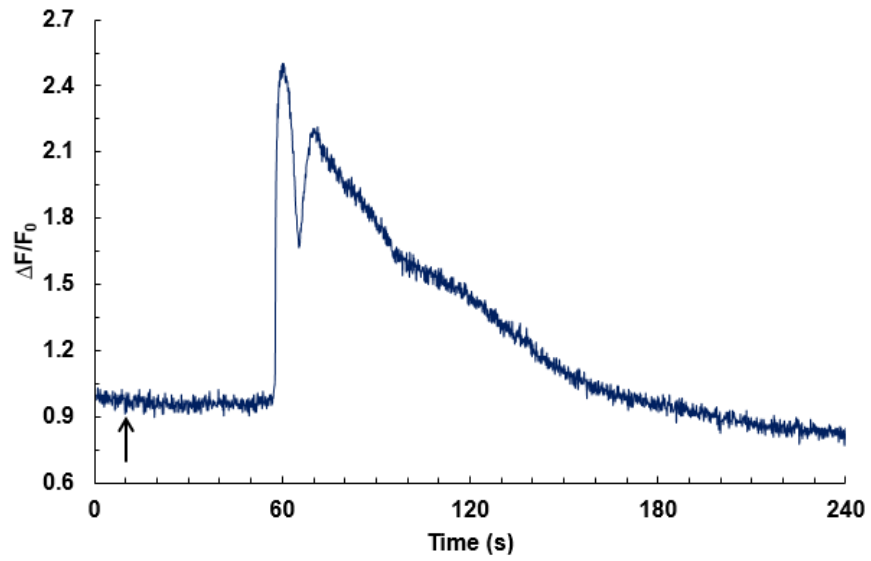
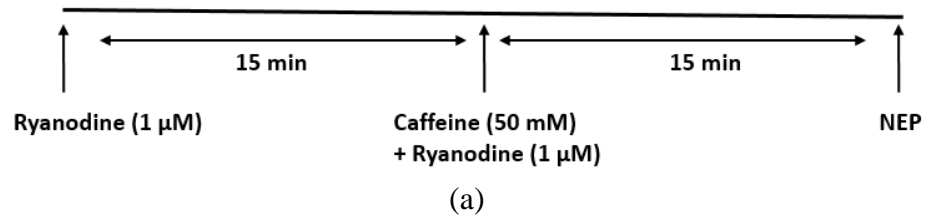
4.3.1.4 *Pretreating cells with both caffeine and ryanodine still did not eliminate the pulse-induced release of Ca^{2+} from intracellular stores*

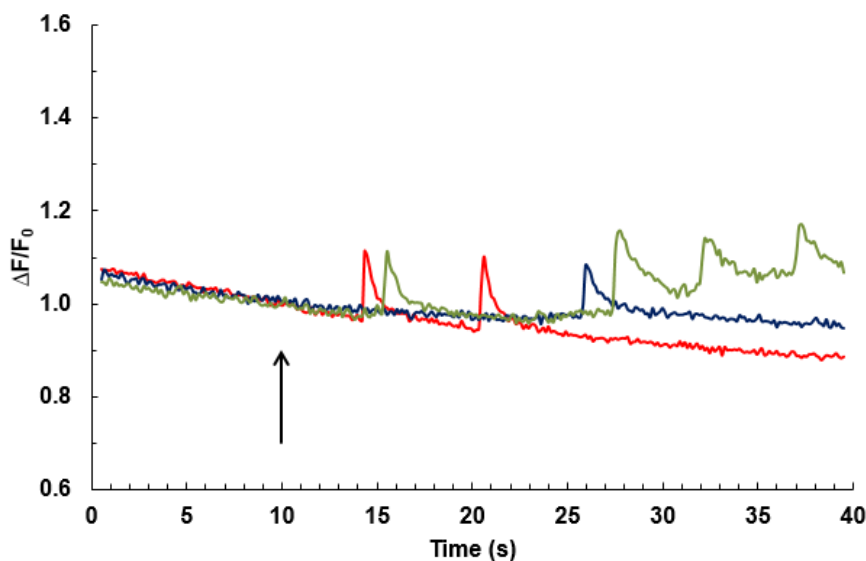
Some researchers have reported that a combination of caffeine and ryanodine was necessary to effectively deplete ryanodine-sensitive Ca^{2+} stores in the ER in chromaffin cells [124,127,128,131,132]. Since NEP-induced Ca^{2+} release was not completely abolished when cells were pretreated with caffeine alone, this suggested that the residual Ca^{2+} in the ER might not have been accessed by caffeine alone. To address this possibility, cells were pretreated with both ryanodine (1 μM) and caffeine (50 mM) prior to NEP exposure (diagram of Fig. 4.10a). Ryanodine, when used at this low concentration, locks

irreversibly the RyRs in an open sub-conductance state causing a slow Ca^{2+} release from the ER ($t_{1/2} \approx 25$ min) [128,133]. Due to its slow activity, ryanodine was added to the cells first. Fifteen minutes later, Ca^{2+} stores were further depleted with the combination of caffeine and ryanodine.

As shown in Fig. 4.10b, the Ca^{2+} transients obtained using both agonists were similar in shape and amplitude to the Ca^{2+} transients observed with caffeine alone, varying from 1.6 to 2.6 (2.26 ± 0.33 S.D., $n = 8$ cells). One noticeable difference, however, was that they were longer lasting (45-140 s) than the transients obtained with caffeine alone (45-90 s).

In cells pretreated with both caffeine and ryanodine, exposure to a single 5-ns, 17 MV/m pulse eliminated Ca^{2+} responses in 20 out of 34 cells. Compared with caffeine pretreatment alone, the percentage of cells that did not respond to the pulse was slightly higher (59 vs 47%, respectively), suggesting that the combination of the two depleting agents caused more Ca^{2+} to be released from the ER. Of the 14 cells that responded to the pulse, two cells showed an immediate Ca^{2+} release (Fig. 4.10c), one of which showed a gradual increase in $[\text{Ca}^{2+}]_i$. The remaining 12 cells showed delayed Ca^{2+} release (Fig. 4.10d) following pulse application, responses that were similar in characteristics to those observed when caffeine was used alone.





(d)

Fig. 4.10. NEP-evoked Ca^{2+} responses in chromaffin cells in the presence of caffeine and ryanodine and absence of extracellular Ca^{2+} . (a) Schematic diagram showing the order in which ryanodine and caffeine were applied to the cells. (b) Representative Ca^{2+} transients following application of caffeine (50 mM) and ryanodine (1 μM) via perfusion. The arrow indicates when perfusion with caffeine and ryanodine was initiated. The traces shown in (c) are typical of immediate responses observed in cells exposed to a single 5-ns duration pulse applied at E-field amplitudes of 17 MV/m. The traces shown in (d) are typical of delayed responses observed in cells exposed to a single 5-ns duration pulse applied at E-field amplitudes of 17 MV/m. $\Delta F/F_0$ was calculated by subtracting the background fluorescence from the fluorescence of the cells and normalizing it to the fluorescence intensity value at the time when the pulse was applied (arrow).

4.3.1.5 *Blocking the sarco/endoplasmic reticulum Ca^{2+} -ATPase (SERCA) pump did not fully abolish the NEP-induced Ca^{2+} release from intracellular stores*

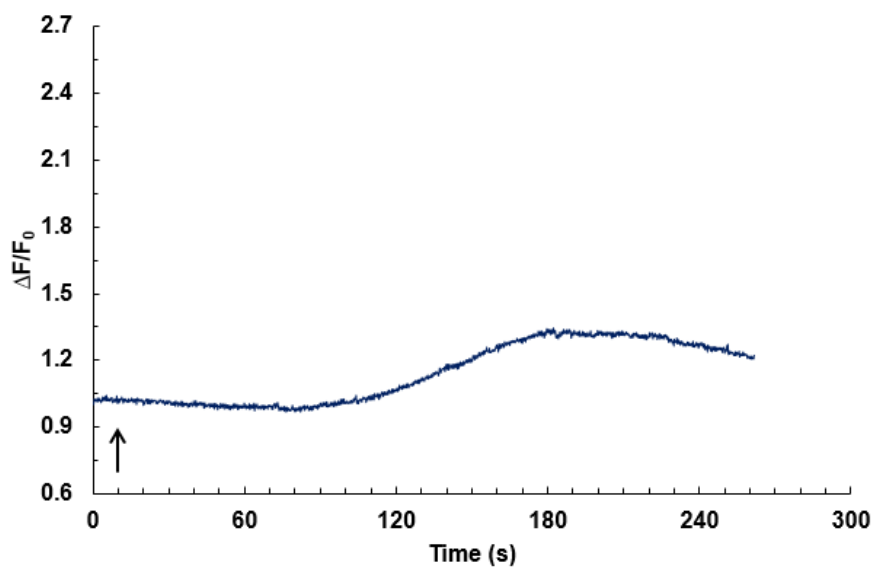
When cells were pretreated with a combination of caffeine and ryanodine, the observation that some cells still showed intracellular Ca^{2+} release following pulse application indicated that either the ryanodine-sensitive stores have not been fully depleted or that Ca^{2+} was coming from an IP_3 -sensitive store. To address this possibility, another strategy was used to deplete ER stores of Ca^{2+} . The strategy was to block the SERCA pump using thapsigargin (TG) or cyclopiazonic acid (CPA) that cause release of Ca^{2+} from both

the ryanodine- and IP₃-sensitive Ca²⁺ stores in the ER. The concentration of CPA that was used in these experiments, 30 μM, has been used to block the SERCA pump in chromaffin cells [134-137].

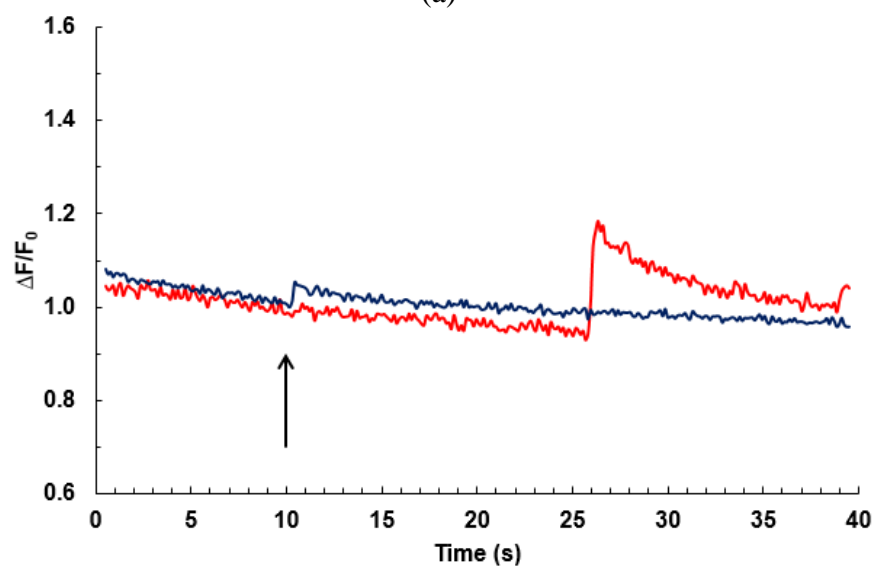
Compared with the rapid Ca²⁺ release evoked by activating the RyRs with caffeine and ryanodine, Ca²⁺ transients evoked by the SERCA inhibitor CPA were more gradual in onset (Fig. 4.11a), indicating that the loss of Ca²⁺ from the ER was a slower process. In fact, the CPA-induced Ca²⁺ transients varied in time from 150 to 270 s, and were 3 times longer than the caffeine-induced Ca²⁺ transients.

After the ryanodine- and IP₃-sensitive Ca²⁺ stores were depleted with CPA, cells were exposed to a single 5-ns, 17 MV/m pulse. The results showed that CPA completely eliminated Ca²⁺ responses in 17 out of 22 cells. The percentage of cells not responding to the pulse in the presence of CPA (77%) was higher than the percentage of cells not responding to the pulse in the presence of both caffeine and ryanodine (59%), indicating that CPA caused more Ca²⁺ to be released from the ER, as it depleted both the ryanodine- and IP₃-sensitive Ca²⁺ pools. Of the 4 cells that responded to the pulse, only one cell showed an immediate release of Ca²⁺ but the response was small in amplitude. The other 3 cells showed a delayed Ca²⁺ release (Fig. 4.11b) that appeared at least 15 s after the pulse. Similar results were obtained using TG (1 μM) to block the SERCA (data not shown).

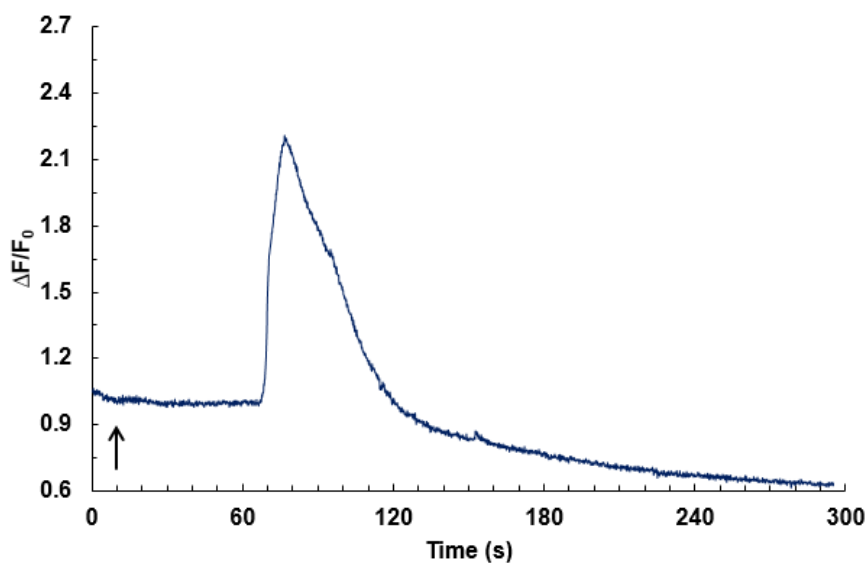
Because blocking SERCA did not completely abolish NEP-induced release of Ca²⁺ from intracellular stores, it was possible that the ryanodine- and/or IP₃-sensitive stores might still not have been fully depleted. Indeed, a subsequent application of caffeine (50 mM) caused additional Ca²⁺ to be released from the ER (Fig. 4.11c).



(a)



(b)



(c)

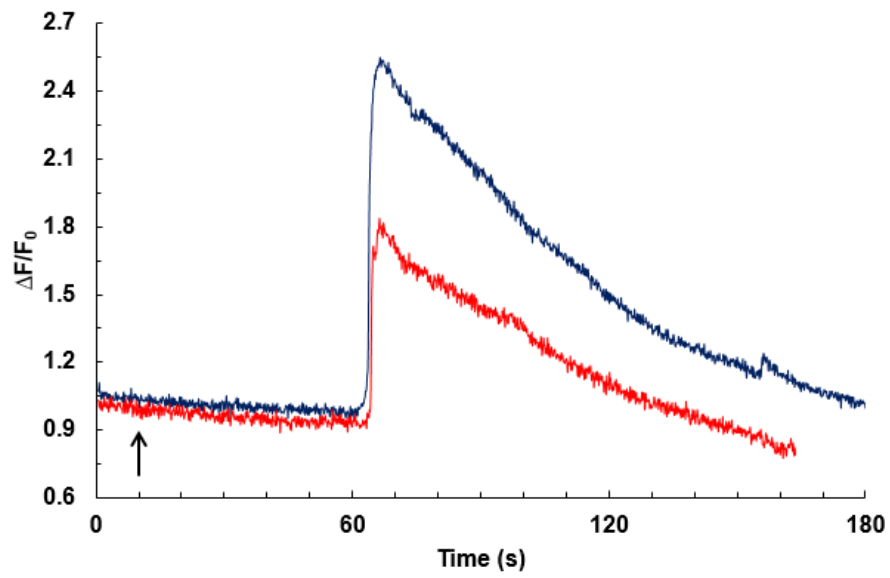
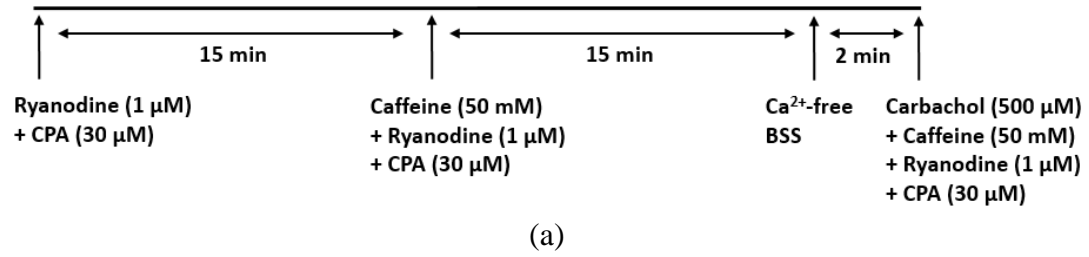
Fig. 4.11. NEP-evoked Ca^{2+} responses in chromaffin cells in the presence of CPA and absence of extracellular Ca^{2+} . (a) Representative Ca^{2+} transients following application of CPA (30 μM) via perfusion. The arrow indicates when perfusion with CPA was initiated. The traces shown in (b) are typical of responses observed in cells exposed to a single 5-ns duration pulse applied at E-field amplitudes of 17 MV/m. $\Delta\text{F}/\text{F}_0$ was calculated by subtracting the background fluorescence from the fluorescence of the cells and normalizing it to the fluorescence intensity value at the time when the pulse was applied (arrow). (c) Representative Ca^{2+} transients following a subsequent application of caffeine (50 mM) via perfusion. The arrow indicates when perfusion with caffeine was initiated.

4.3.1.6 *A combination of caffeine, ryanodine and CPA was required to completely abolish the pulse-induced Ca^{2+} release from intracellular stores in chromaffin cells*

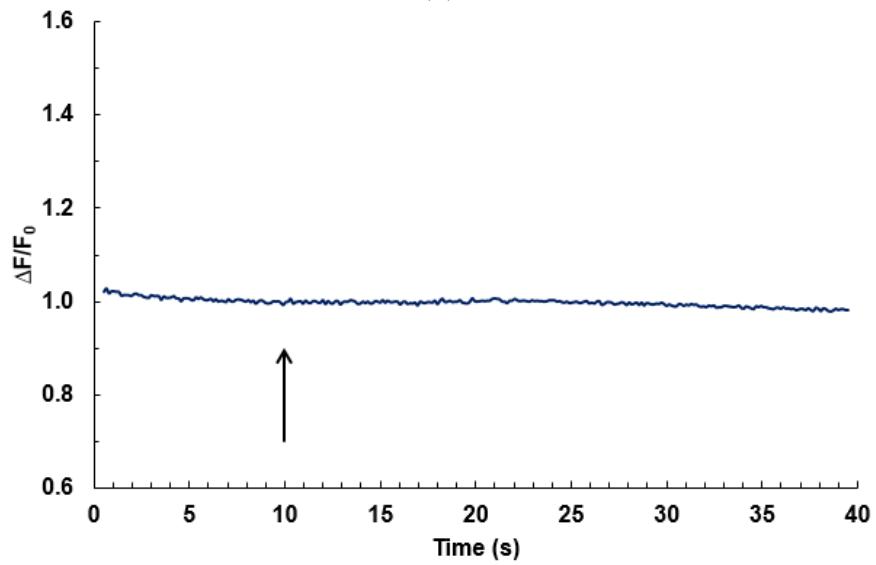
Because a combination of caffeine and ryanodine alone, or CPA alone, were not sufficient to fully deplete the Ca^{2+} stores in the ER of chromaffin cells, a series of additional experiments were conducted to determine whether a combination of all three agents was necessary to cause full depletion of the Ca^{2+} pools in the ER. The order in which the agents have been added to accomplish this depletion is shown in the schematic of Fig. 4.12a. Because of the slow activity of ryanodine and CPA compared to caffeine, ryanodine (1 μM)

and CPA (30 μM) were added to the cells first in the absence of extracellular Ca^{2+} . To minimize photobleaching, fluorescence of the cells was not monitored during this initial application. Fifteen minutes later, caffeine (50 mM) was added and the cells incubated with all three agents for 15 min. As shown in Fig. 4.12b, the Ca^{2+} transients obtained using all three depleting agents were similar in shape and amplitude to the transients obtained with the combination of caffeine and ryanodine, varying in amplitude from 1.7 to 2.8 (2.19 ± 0.39 S.D., $n = 8$ cells). In addition, Ca^{2+} transients lasted slightly longer (80-140 s) than the transients obtained with caffeine and ryanodine (45-140 s).

When a single 5-ns, 17 MV/m pulse was applied after ER Ca^{2+} stores were depleted with the combination of all three agents, NEP-induced Ca^{2+} release from intracellular stores was completely abolished (Fig. 4.12c). Forty six out of 46 cells obtained from different cell preparations showed no response to the pulse. To verify that the lack of response to the pulse was due to full depletion of the ryanodine- and IP_3 -sensitive stores in the ER, an application of carbachol (500 μM), caffeine (50 mM), ryanodine (1 μM) and CPA (30 μM) did not cause any additional Ca^{2+} release from the eight cells tested (Fig. 4.12d), indicating that all the Ca^{2+} pools in the ER were fully depleted. These results are in agreement with the hypothesis that the ER is the primary target of NEPs in chromaffin cells, and suggest that the secretory granules are not affected by the pulse.



(b)



(c)

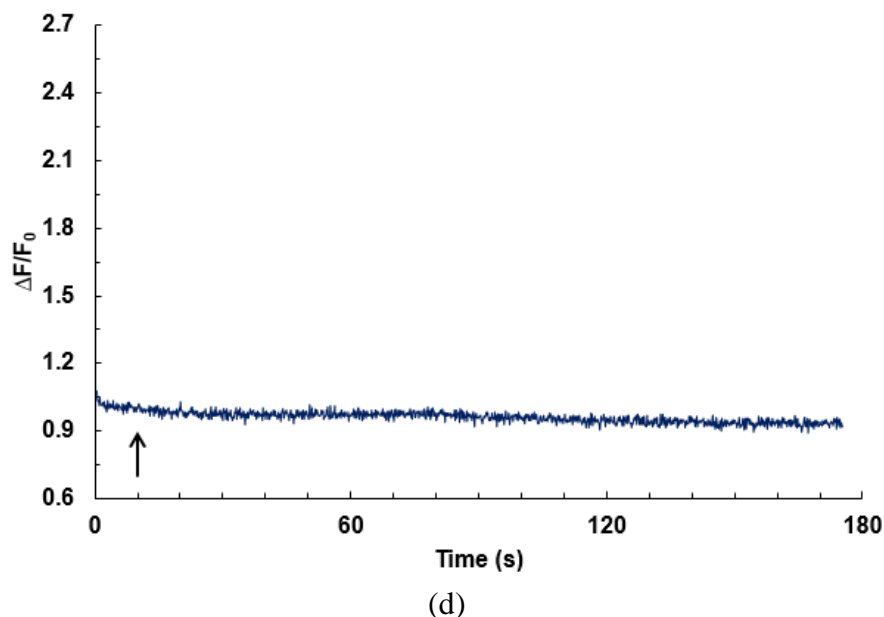


Fig. 4.12. NEP-evoked Ca^{2+} responses in chromaffin cells in the presence of caffeine, ryanodine and CPA and absence of extracellular Ca^{2+} . (a) Schematic diagram showing the order in which ryanodine, CPA and caffeine were applied to the cells. (b) Representative Ca^{2+} transients following application of caffeine (50 mM), CPA (30 μM) and ryanodine (1 μM) via perfusion. The arrow indicates when perfusion with caffeine, CPA and ryanodine was initiated. The trace shown in (c) is typical of responses observed in cells exposed to a single 5-ns duration pulse applied at E-field amplitudes of 17 MV/m. $\Delta F/F_0$ was calculated by subtracting the background fluorescence from the fluorescence of the cells and normalizing it to the fluorescence intensity value at the time when the pulse was applied (arrow). (d) Representative Ca^{2+} response following application of carbachol (500 μM) in cells pretreated with caffeine (50 mM), CPA (30 μM) and ryanodine (1 μM) via perfusion. The arrow indicates when perfusion with carbachol, caffeine, CPA and ryanodine was initiated.

4.3.2 Numerical modeling results

The experimental results point to the ER as the primary structure being porated. To investigate whether the ER is the primary target of NEPs in chromaffin cells, and also assess any possible electroporation of the secretory granules, a localized model of chromaffin cell organelles was constructed. The model was further used to understand why high E-field amplitudes are required to electroporate the ER membrane. To address these

points, a more realistic representation of the size of chromaffin granules and their measured dielectric properties were incorporated into the model in which structures representing six secretory granules were placed around the ER as represented in Fig. 4.3.

We have shown in the previous chapter that the electrical properties assigned to the different structures had an influence on the modeling results. Because of the lack of availability in the literature of specific values for the conductivity of the ER interior (σ_{ERin}), a parametric study was conducted based on σ_{ERin} to explore its influence on the threshold E-field required to electroporate the ER membrane. The values of σ_{ERin} tested in the model were 0.01, 0.1 and 0.5 S/m. The two latter values were chosen because they fall in the range of conductivities for intracellular organelles reported in the literature [26]. The value $\sigma_{ERin} = 0.01$ S/m was included in the parametric study because it gave good agreement between the experimental and numerical results for the threshold E-field necessary to electroporate the granule membrane (Section 3.3.3).

The amplitude of the applied E-field was varied in the simulations from 3 to 25 MV/m. As stated in Chapter 3, the threshold E-field for significant electroporation was defined as the E-field amplitude that results in a pore density of 10^{14} m⁻² at the anodic pole of a membrane [116].

4.3.2.1 *The threshold E-field amplitude required to electroporate the ER membrane correlated with the experimental threshold for $\sigma_{ERin} = 0.01$ S/m*

The effect of σ_{ERin} on the electroporation of the ER membrane was studied first. For each value of σ_{ERin} , the pore density at the anodic pole of the ER membrane was computed for E-field amplitudes ranging from 3 to 25 MV/m. The results in Fig. 4.13 indicated that

reducing the value of σ_{ERin} from 0.5 to 0.01 S/m increased the threshold E-field amplitude required to electroporate the ER membrane from 4 to 8 MV/m, respectively, thus giving a threshold E-field amplitude similar to the one found experimentally (8 MV/m).

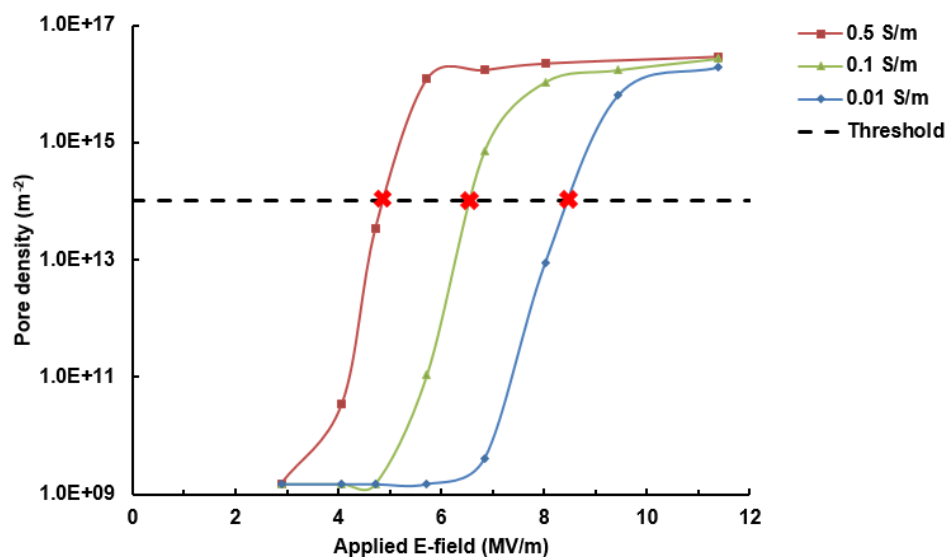


Fig. 4.13. Influence of σ_{ERin} on the E-field threshold amplitude required to electroporate the ER membrane. The pore density is plotted as a function of the applied E-field for each value of σ_{ERin} . The red “x” on the plot corresponds to the E-field threshold amplitude required to electroporate the ER membrane. The black dashed horizontal line on the plot indicates the threshold for a pore density of 10^{14} m^{-2} , referred to as significant electroporation. E-field amplitudes up to 12 MV/m are shown on the x-axis because the pore density saturates for E-fields greater than 12 MV/m.

4.3.2.2 *The presence of multiple secretory granules around the ER did not affect the E-field threshold amplitude required to electroporate the ER membrane*

The presence of the large number of secretory granules in the cytoplasm might be limiting the E-field from penetrating into the ER, which could be another explanation for why a high E-field threshold amplitude is required to electroporate the ER membrane. This possibility was investigated through the computation of the E-field with and without the

granules located around one side of the ER, and by the application of a pulse in the opposite direction, i.e., from the side of the ER not surrounded by the granules.

We first started by modeling the ER alone in the absence of secretory granules. This was accomplished by assigning cytoplasm properties to the secretory granules. A different geometry was not generated to model the ER alone because of the necessity to preserve the mesh of the modeled geometry (Fig. 4.4a) so that any changes observed in the E-field amplitudes would be only attributed to the influence of the granules around the ER. The E-field threshold amplitude required to electroporate the ER membrane in the absence of the secretory granules was determined by computing the pore density at the anodic pole of the ER membrane for amplitudes of the applied E-field ranging from 3 to 25 MV/m. As shown in Fig. 4.14, the results indicated that the ER membrane electroporated at 8 MV/m, a value similar to the E-field threshold amplitude obtained when the ER was surrounded by the granules (i.e. original pulse direction, Section 4.3.2.1).

Another control geometry was modeled in which secretory granules were placed around the ER, but with the pulse being applied in the opposite direction, i.e., from the side of the ER not surrounded by the granules. The results showed that the ER membrane electroporated at 8 MV/m (Fig. 4.14), a value similar to the E-field threshold amplitude obtained when a pulse was applied in the original direction. These overall results indicate that the presence of the secretory granules around the ER did not affect the electroporation of the ER membrane.

As an example, Fig. 4.15 shows that the electric potential around the ER was not affected by the presence of the granules. Thus, similar E-field amplitudes would be expected to electroporate the ER membrane in all cases considered.

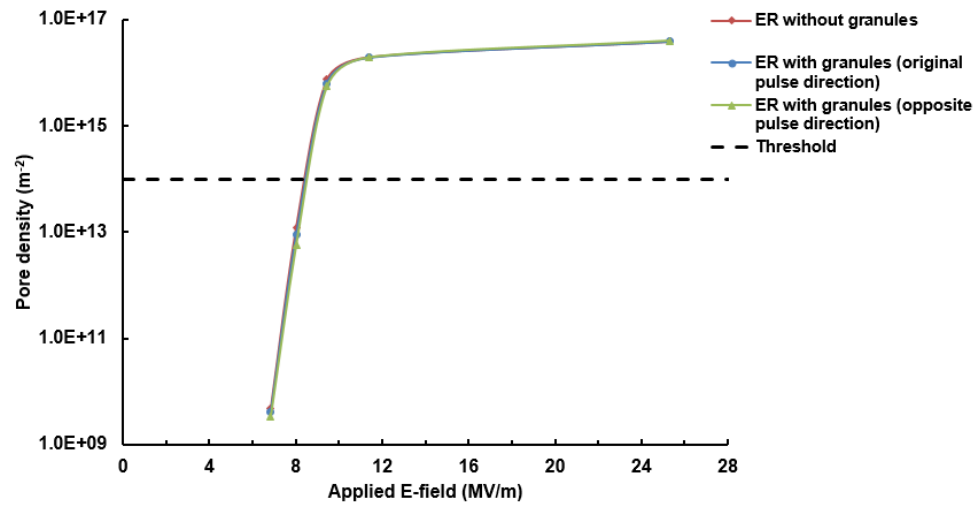
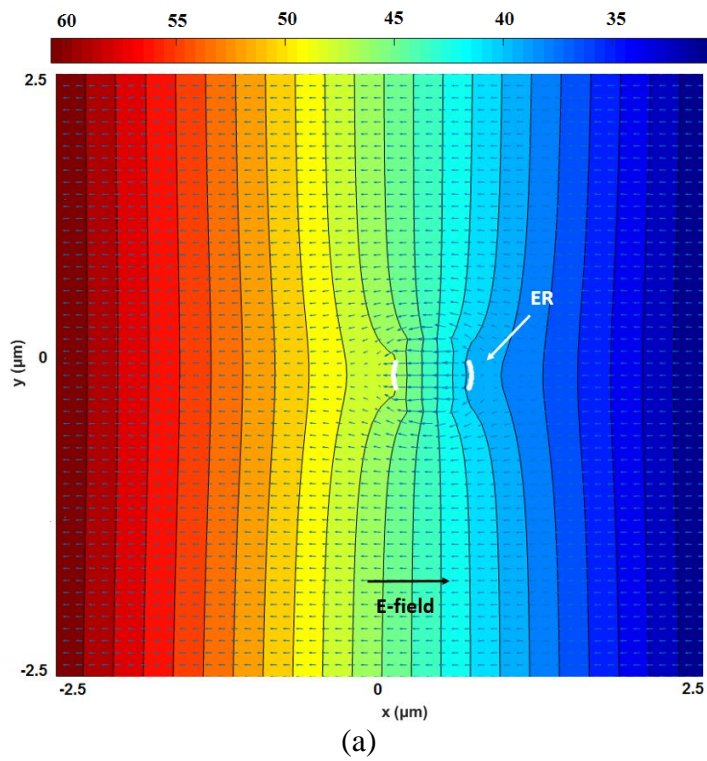


Fig. 4.14. Pore density calculated at the anodic pole of the ER membrane for $\sigma_{ERin} = 0.01$ S/m for the different configurations of the granules and electrodes. The black dashed horizontal line indicates the threshold for a pore density of 10^{14} m^{-2} .



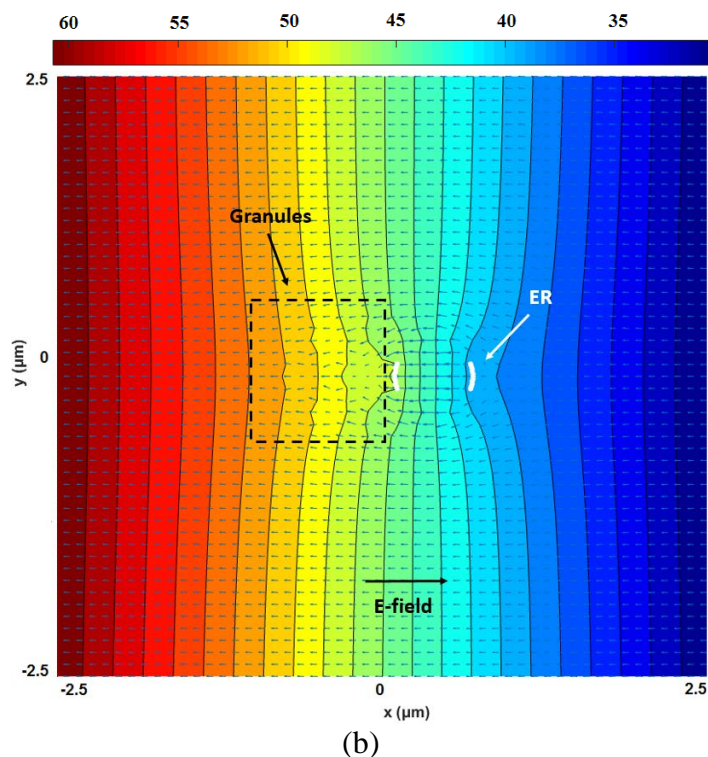


Fig. 4.15. Spatial distribution of the electric potential in and around the ER for an applied E-field of amplitude 9 MV/m. (a) The ER is modeled without granules surrounding it. (b) The ER is modeled with the granules surrounding it. The dashed square represents the location of the granules. The white areas in (a) and (b) represent a pore density greater than 10^{14} m^{-2} in the ER membrane. The color bars represent the electric potential in Volts (V).

4.3.2.3 *E-field amplitudes greater than 22 MV/m were required to electroporate the membranes of the secretory granules*

To validate further that the ER is the target of the NEPs in chromaffin cells and not the secretory granules, the E-field amplitude was increased from 3 to 25 MV/m and the pore density was computed at the anodic pole of the ER and granule membranes. Modeling results indicated that while for $\sigma_{ERin} = 0.01 \text{ S/m}$ the ER membrane electroporated at 8 MV/m, an E-field amplitude greater than 22 MV/m was required to electroporate the membranes of the secretory granules (Fig. 4.16). The requirement of a high E-field to electroporate the secretory granule membranes in the model is in agreement with the

experimental findings showing that the ER is the primary target of NEPs in chromaffin cells for E-field amplitudes up to 17 MV/m.

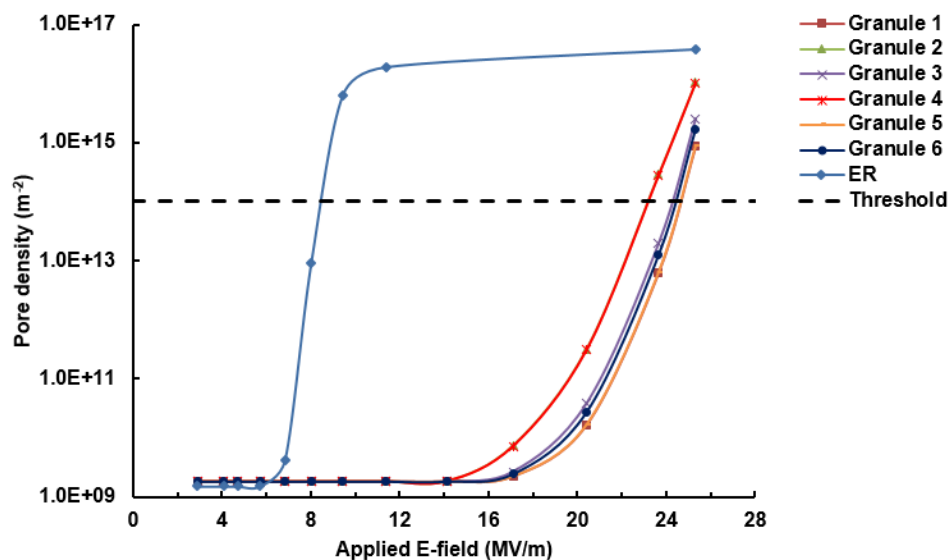


Fig. 4.16. Pore density computed at the anodic pole of the ER and granule membranes for a range of E-field amplitudes from 3 to 25 MV/m. The black dashed horizontal line indicates the threshold for a pore density of 10^{14} m^{-2} .

4.4. Discussion

The goal of the present study was to identify the source of intracellular Ca^{2+} released in response to a single 5-ns, 17 MV/m electric pulse using an experimental approach, and refine the numerical model to understand the basis for intracellular membrane permeabilization with respect to E-field amplitude. We have shown in the previous chapter that a single 5-6 ns electric pulse applied at E-field amplitudes greater than 8 MV/m was required to cause Ca^{2+} release from internal stores. The approach taken in this study to identify from where Ca^{2+} was being released was to deplete Ca^{2+} from the ER and assess the NEP-induced rise in $[\text{Ca}^{2+}]_i$ following ER depletion.

In conjunction with this effort, the dielectric properties of the secretory granules were obtained from microfluidic impedance spectroscopy measurements (manuscript in preparation) and used in the numerical model that was refined locally to represent realistic sizes of secretory granules. Both the experimental and modeling results pointed to the ER as the primary target of NEPs in chromaffin cells.

4.4.1 Characteristics of NEP-induced Ca^{2+} release from the ER

4.4.1.1 *Comparison with receptor agonist stimulation*

In the previous chapter, Ca^{2+} release from intracellular stores was attributed to direct permeabilization of the membranes by the NEP. In this study, the characteristics of Ca^{2+} release from internal stores were further investigated using the receptor agonist carbachol in which the cell responses obtained were compared to those evoked by a single 5-ns pulse applied at an E-field amplitude of 17 MV/m.

The Ca^{2+} transients obtained in response to carbachol differed from those obtained following pulse application. Carbachol evoked a smooth and large $[\text{Ca}^{2+}]_i$ rise (2.15 ± 0.48 S.D., $n = 4$ cells) (Fig. 4.7) while NEP-induced Ca^{2+} responses were mainly abrupt and small in amplitude (1.15 ± 0.07 S.D., $n = 30$ cells) (Fig. 4.8) even at the highest E-field amplitude investigated (21 MV/m). In addition, the rise in $[\text{Ca}^{2+}]_i$ evoked by the pulse was highly variable, varying from single Ca^{2+} transients to multiple Ca^{2+} transients (or spiky activity).

A similar study conducted by White et al. (2004) [56] using HL-60 cells compared Ca^{2+} mobilization from the ER evoked by an agonist to that evoked by 60-ns duration pulses. The results showed that Ca^{2+} mobilization from internal stores using a single 60-ns

pulse and the purinergic agonist UTP had similar kinetics. Both stimuli caused rapid Ca^{2+} mobilization from the ER, suggesting that the pulse and the agonist utilized the same Ca^{2+} channels (i.e. IP_3Rs and RyRs) present in intracellular membranes that caused Ca^{2+} release from internal stores [56]. Nevertheless, the authors did not exclude the possibility that Ca^{2+} could have been released through transient nanopores that formed in the intracellular membranes.

In chromaffin cells, the characteristics of Ca^{2+} release evoked by carbachol differed from those evoked by a single 5-ns pulse. Thus, we conclude that the agonist and the 5-ns pulse were affecting the ER membrane differently and that the mechanisms by which Ca^{2+} is being released from the ER does not involve activation of signaling pathways inside the cell as has been reported by Tolstykh et al. (2013) [58]. Rather Ca^{2+} is released through nanopores that formed in the membrane of the ER during pulse application.

4.4.1.2 Short time course of NEP-induced single Ca^{2+} transients

The single Ca^{2+} transients observed following NEP application were either short-lived (lasting less than 10 s after the pulse) or longer-lived (lasting more than 10 s after the pulse), with no sustained Ca^{2+} release being observed in any of the cells tested (Fig. 4.8). One possible explanation for the transient Ca^{2+} responses is the short lifetime of the nanopores that form in the intracellular membranes, not allowing continuous Ca^{2+} release from intracellular stores. The pore lifetime has been predicted by MD simulations to be of the order of nanoseconds [37], even though longer pore lifetimes of the order of seconds have been reported in some theoretical [36,42] and experimental studies [65,70]. Furthermore, the transient Ca^{2+} responses indicate that the Ca^{2+} that was released was either taken up by

the mitochondria, pumped back to the ER via the SERCA pump, or pumped out of the cell through the PMCA or $\text{Na}^+/\text{Ca}^{2+}$ exchanger system in the plasma membrane [82].

4.4.1.3 Possible basis for NEP-induced multiple Ca^{2+} transients

The spiky nature of the Ca^{2+} transient observed in some cells appeared to occur more frequently at the higher E-field amplitudes. For example, while none of the cells ($n = 44$ cells) exposed to a 5-ns pulse showed a spiky activity at E-field amplitudes ≤ 15 MV/m, 9 of 30 cells showed this type of activity at 17 MV/m (Fig. 4.8, green and orange traces). To our knowledge, the spiky Ca^{2+} activity observed in chromaffin cells has not been reported by other groups studying NEP-induced Ca^{2+} release from intracellular stores in different cell types [54]. The reason for this type of spiky response is not known. It could be that, in addition to creating pores, the NEP affected the Ca^{2+} release channels present in internal membranes, like the IP_3Rs or RyRs , inducing conformational changes in the proteins present in the receptors and triggering the channels to open [57]. If the channels are not activated at the same time, Ca^{2+} could then be released at different time points, explaining the observed multiple Ca^{2+} transients.

4.4.2 Identification of the source of Ca^{2+} released in response to a 5-ns pulse

4.4.2.1 Partial ER depletion of Ca^{2+}

When the ER was partially depleted by caffeine alone, caffeine and ryanodine, and CPA alone, a variety of cell responses were observed in response to a 5-ns pulse. Ten of

41 cells showed an immediate Ca^{2+} response. However, 31 cells showed a delayed release of Ca^{2+} .

a. Ca^{2+} release was immediate

Exposing chromaffin cells pretreated with caffeine, or with caffeine and ryanodine to a single 5-ns pulse caused an immediate Ca^{2+} release that was small in amplitude, and slowly increased over time. On the other hand, when the SERCA was blocked with CPA, only one cell showed an immediate and small Ca^{2+} transient.

The increase in $[\text{Ca}^{2+}]_i$ following depletion with caffeine, or with caffeine and ryanodine could be attributed to pores that have formed in the ER membrane that remained open after the pulse, thus causing the residual Ca^{2+} to leak from the ER into the cytoplasm down its concentration gradient. A second possibility is that the NEP could have initially triggered the residual Ca^{2+} to be released from the ER, and later when $[\text{Ca}^{2+}]_i$ reached a certain threshold, it caused CICR from the RyRs [124]. A third possible explanation is that the NEP could have activated a signaling pathway inside the cell starting from the plasma membrane, such as the PLC/ IP_3 pathway, which activates the IP_3 Rs and causes Ca^{2+} to be released from the IP_3 -sensitive Ca^{2+} pools present in the ER. Lastly, the possibility that Ca^{2+} could have been released from a Ca^{2+} store other than the ER, for example the secretory granules, cannot be excluded. This last possibility will be discussed more in a later section.

The immediate cell response observed when the cells were pretreated with CPA could be attributed to the residual Ca^{2+} being released through nanopores that formed in the ER membrane.

b. Ca²⁺ release was delayed

When the ER was partially depleted of Ca²⁺ using caffeine alone or caffeine and ryanodine, most of the cells (n = 31 of 41 cells) exhibited a delayed Ca²⁺ release that varied from single Ca²⁺ transients to a spiky Ca²⁺ activity (Figs. 4.9.c, 4.10.d and 4.11.b). The spiky Ca²⁺ release was not observed when cells were pretreated with CPA alone. Rather, delayed single Ca²⁺ transients were observed. Because chromaffin cells did not show any spontaneous activity in the absence of extracellular Ca²⁺, nor when the stores were partially depleted with caffeine (data not shown), these delayed responses were attributed to a delayed NEP-induced effect on the ER.

The mechanism by which these delayed responses occur has not been determined. It could be that the NEP is inducing signaling events in the cell that are causing a delayed Ca²⁺ release from the ER. For example, it has been reported that a single 600-ns pulse applied to CHO cells induces a plasma membrane perturbation resulting in activation of lipid signaling pathways inside the cell leading to accumulation of IP₃ in the cytoplasm [58]. Even though activation of such signaling pathways has not been demonstrated in chromaffin cells, it could be that application of a NEP at such high E-field amplitudes (17 MV/m) perturbed the plasma membrane causing activation of signaling pathways such as the PLC/IP₃. The time it takes to generate a threshold level of IP₃ in the cytoplasm that could elicit Ca²⁺ release from the ER could be one explanation for the delayed responses observed.

4.4.2.2 Complete ER depletion abolished NEP-evoked Ca^{2+} release

As assessed by application of carbachol, the combination of caffeine, ryanodine and CPA was maximally effective at fully depleting the ER of Ca^{2+} . When pretreating cells with all three agents, application of a 5-ns pulse after depletion completely abolished the pulse-induced $[Ca^{2+}]_i$ rise. These results led us to conclude that the ER is the primary target of NEPs in chromaffin cells.

4.4.2.3 Secretory granules do not appear to be a target of NEPs

Nanometer-size secretory granules occupy ~30% of the volume of the cytosol (20,000-30,000 granules/cell) and of all the Ca^{2+} stores contain the highest Ca^{2+} concentration (~40 mM), constituting more than 60% of the total Ca^{2+} content in chromaffin cells [138,139]. However, 99.9% of the granular Ca^{2+} is strongly bound to chromogranins A and B, which are high-capacity, low-affinity Ca^{2+} binding proteins, and only 0.1% of the intragranular Ca^{2+} is free (20-100 μ M) [89]. It has been reported that Ca^{2+} release from secretory granules can occur in a way similar to Ca^{2+} release from the ER, i.e., through the activation of IP_3 Rs and RyRs, or through inhibition of the SERCA pump [89,140,141]. However, there is still controversy about Ca^{2+} release from the secretory granules, which is not guaranteed to occur in response to stimulation with caffeine, ryanodine or CPA [142]. Therefore, the Ca^{2+} content inside the granules might have remained intact after pretreating the cells with caffeine, ryanodine and CPA.

In addition, secretory granules contain H^+ that creates an acidic medium inside the granules (pH \approx 5.5) that is maintained by the activity of a specific vesicular H^+ -ATPase (V-ATPase). Maintaining an acidic pH plays an important role in the dynamics of

intragranular Ca^{2+} and an increase in granule pH can significantly alter the Ca^{2+} binding property of chromogranins [89,143]. In fact, disruption of the intragranular pH can cause Ca^{2+} to be released from the granule into the cytosol, triggering granule motion and its own exocytosis [89,143,144].

Thus, exposing chromaffin cells to a NEP could cause pores to form in the granule membrane. Depending on how long the pores stay open, the granular pH might change due to exposure of the granule interior to the cytosol ($\text{pH} \approx 7.3$). In this case, the previously bound Ca^{2+} is freed, increasing the concentration of free Ca^{2+} and making Ca^{2+} available for release (personal communications with Dr. Seung Hyun Yoo, Incheon, Korea). However, breakdown of the matrix could take time because Ca^{2+} is strongly bound to the chromogranins. Since after complete ER depletion none of the cells tested responded to the NEP, we conclude that the secretory granules do not appear to be a target of NEPs.

4.4.3 Comparison between the modeling and experimental results

Having identified the ER as the source of Ca^{2+} released in response to a NEP, the 2D numerical model constructed in this study was used to address the requirement for high E-field amplitudes necessary for poration of this organelle and understand the basis for intracellular membrane permeabilization.

4.4.3.1 Basis for the requirement for a high E-field amplitude to porate the ER

To understand the requirement for a high E-field amplitude to porate the membrane of the ER, a parametric study was conducted for σ_{ERin} . Modeling results showed that when

σ_{ERin} decreased from 0.5 to 0.01 S/m, the E-field threshold amplitude required to electroporate the ER membrane increased from 4 to 8 MV/m, thus correlating with the experimental threshold required to cause Ca^{2+} release from the ER. The increase in the threshold E-field with a decrease in σ_{ERin} can be explained by considering the charging time of the ER membrane. According to equation (2) in Chapter 1, the charging time is inversely proportional to σ_{ERin} , indicating that the ER membrane charges more slowly for $\sigma_{ERin} = 0.01$ S/m compared to when $\sigma_{ERin} = 0.5$ S/m. This effect is also reflected in the values of the TMP. Fig. 4.17 shows that, for the same starting E-field amplitude of 3 MV/m, the initial TMP value was higher for the value of $\sigma_{ERin} = 0.5$ S/m when compared to that at the value of $\sigma_{ERin} = 0.01$ S/m. As the E-field amplitude was increased from 3 to 12 MV/m, the TMP reached the critical threshold voltage of ~ 1 V at lower E-field amplitudes for $\sigma_{ERin} = 0.5$ S/m compared to when $\sigma_{ERin} = 0.01$ S/m. Consequently, higher E-field amplitudes were required to electroporate the ER membrane when the value of σ_{ERin} was lower.

The dependence of the E-field threshold required to electroporate an organelle membrane on the conductivity of the organelle interior was reported in Retelj et al. (2013) where it was shown that electroporation of these membranes increased when the conductivity of the organelle interior decreased [116]. These and our results confirm that the conductivity value assigned to the ER interior has an effect on the electroporation of the ER membrane.

However, other parameters used in the model, such as the permittivity of the ER membrane and the critical voltage for electroporation (i.e. V_{ep}), might also have an influence on the electroporation of the ER membrane. For example, if the ER membrane requires higher threshold voltages to be electroporated, the E-field threshold amplitudes

determined from the model might be an underestimate [116]. This could be a reason why the model did not explain accurately the requirement for high E-field amplitudes to porate the ER membrane.

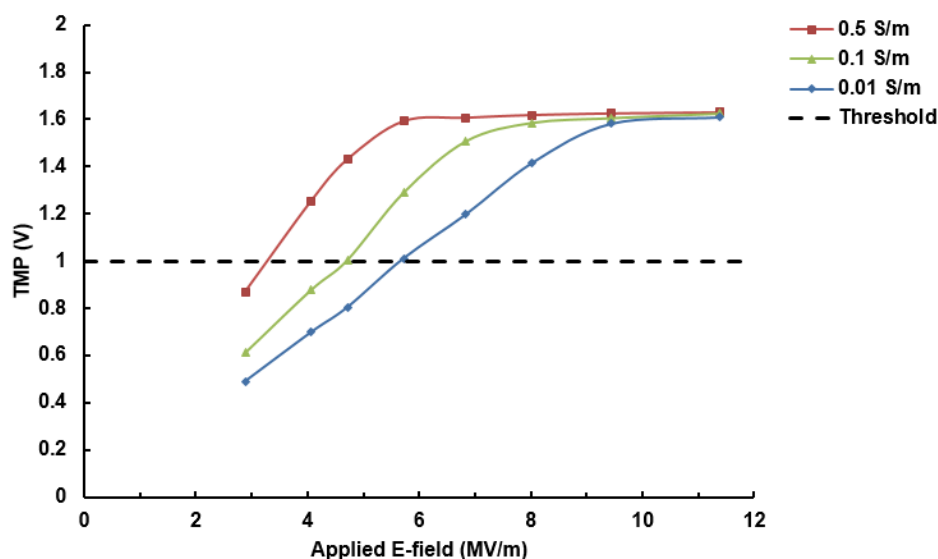


Fig. 4.17. TMP as a function of the applied E-field for different values of σ_{ERin} . The black dashed horizontal line on the plot indicates the critical threshold for reversible electrical breakdown (~ 1 V).

4.4.3.2 Secretory granules do not appear to exert a “shielding” effect on the ER

Another possible explanation of the requirement for a high E-field amplitude to cause significant poration of the ER membrane is the presence of a large number of secretory granules in the cytoplasm of a chromaffin cell, which might be limiting the E-field from penetrating into the ER. This possibility was investigated in the model by placing six secretory granules around the ER. Modeling results showed that the presence of the secretory granules did not have an effect on the electroporation of the ER membrane. This can be attributed to both the size of the individual granules (ratio of a single granule area

to the modeled area is 0.03%) as well as their total areas in the domain (ratio of sum of granules area to modeled area is 0.2%) being small relative to the entire modeled area.

4.4.3.3 *Basis for the requirement for a high E-field amplitude to porate secretory granules*

Since the secretory granules did not appear to be a target of NEPs when chromaffin cells were exposed to a single 5-ns pulse at 17 MV/m, the model was used to validate this observation. By using measured dielectric properties of chromaffin granules (i.e. granule interior conductivity of 0.3 S/m and granule membrane permittivity of 30) in the model, the results showed that E-fields greater than 22 MV/m were required to porate the granule membranes. This high E-field amplitude is attributed to the high capacitance of the granule membrane, since the voltage induced as a function of time is slow on a membrane with high dielectric permittivity [26]. Similar results were reported in Retelj et al. (2013) using a 4-ns electric pulse, showing that a higher E-field threshold was required to electroporate the membrane of intracellular organelles with higher membrane permittivity [116].

The model validated the source of intracellular Ca^{2+} release as the ER, leading to the conclusion that the ER is the primary structure porated in chromaffin cells for E-field amplitudes up to 17 MV/m, and that E-field amplitudes greater than 22 MV/m were required to electroporate the membrane of the secretory granules. The agreement obtained between the model and the experimental findings with respect to the threshold E-field amplitude required to porate the secretory granules point to the importance of knowing the dielectric properties of the different structures modeled since they can be so different from

the values reported in the literature, and thus affect the interpretation of the experimental observations.

4.5. Conclusions

The present study identified the ER as the intracellular structure porated in chromaffin cells for evoking Ca^{2+} release and showed how complex NEP-induced Ca^{2+} release could be. For instance, when the stores were partially depleted of Ca^{2+} , several cell responses were observed, which varied from immediate Ca^{2+} release to delayed single or multiple Ca^{2+} transients. The reason for these various cell responses has not yet been determined, and requires further investigation in order to have a better understanding of how NEPs interact with the cell and its organelles.

Furthermore, this study showed that for specific parameters chosen in the model, agreement was obtained between the modeling and experimental results with respect to the source of intracellular Ca^{2+} release and with respect to the requirement for a high E-field amplitude to electroporate the ER and secretory granule membranes. These results highlight the importance of knowing accurately the dielectric properties of the different intracellular organelles in the model since their real values might be different from what has been reported in the literature for other cell types, hence they could affect the computed results tremendously and the interpretation of the experimental observations.

CHAPTER 5. Conclusions and future work

Using a combination of experimental and numerical modeling approaches, the overall goal of this study was to understand how high intensity, 5-ns electric pulses affect the membranes of chromaffin cells. The main finding is that the ER is porated by a single 5-ns pulse at a threshold E-field amplitude significantly higher than that required to cause permeabilization of the plasma membrane. Whole-cell patch clamp recordings showed that a single 5-ns pulse applied at a threshold E-field amplitude of 4 MV/m causes plasma membrane permeabilization. However, twice this E-field amplitude was required to cause Ca^{2+} release from the ER, identified to be the primary intracellular structure porated in chromaffin cells.

Similar findings were reported by Iurri et al. (2013) showing that a single 60-ns electric pulse triggered Ca^{2+} efflux from the ER in CHO cells at a threshold E-field amplitude of 1.9 MV/m and Ca^{2+} influx into cells directly across the cell membrane, which is indicative of membrane permeabilization, at a threshold E-field amplitude of 0.9 MV/m [54]. However, the authors did not further speculate on the basis for this difference.

To our knowledge, we are the only group trying actively to understand the disparity between experimental and numerical modeling results with respect to the high E-field amplitude required to porate intracellular membranes compared to those required to permeabilize the plasma membrane. Therefore, in this study, numerical modeling of a 2D chromaffin cell model was carried out as an attempt to understand the requirement for a high E-field amplitude to cause electroporation of the ER membrane versus the plasma membrane.

Initial results obtained from the numerical model agreed with the experimental findings with respect to the threshold E-field amplitude required to electroporate the plasma membrane but not with respect to the threshold E-field required to electroporate the ER membrane. Modeling results showed that for a value of $\sigma_{\text{cyto}} = 0.3 \text{ S/m}$, nanopores form in the plasma membrane at an E-field threshold amplitude of 4 MV/m. As stated previously in Chapter 3, this value of σ_{cyto} matched well with the preliminary value calculated based on the measurements conducted to determine dielectric properties of chromaffin cells (Chapter 2) and was therefore assumed to be representative of the conductivity of the cytoplasm in chromaffin cells.

Furthermore, to obtain better agreement between the experimental and numerical modeling results and confirm that the granules were not porated at E-field amplitudes less than 17 MV/m, the dielectric properties of the secretory granules were obtained from microfluidic impedance spectroscopy measurements (Chapter 2) and used in the numerical model that was refined locally to represent realistic sizes of secretory granules. Results obtained from the localized model showed that for a specific value of the conductivity of the ER interior ($\sigma_{\text{ERin}} = 0.01 \text{ S/m}$), agreement was obtained between the model and experiments with respect to the requirement for a high E-field amplitude to porate the ER membrane. The model also confirmed the requirement for E-field amplitudes greater than 22 MV/m to cause electroporation of the granule membranes.

Knowing accurately the dielectric properties of the different structures modeled point to the importance of the parameters used in a numerical model, since their values could be different from those reported in the literature, thus affecting interpretation of the numerical results and explanation of the experimental observations. In this study, a lot of effort went

into creating a model that was specific to a chromaffin cell in order to understand the requirement for high E-field amplitudes required to electroporate the membranes of intracellular organelles.

Another major finding of this work is that NEP-induced Ca^{2+} release from intracellular stores was complex, and did not always occur as a single transient, as shown in the previous chapter (Sections 4.3.1.2-4.3.1.5). Rather various cell responses were obtained following single pulse application, especially when the ER was partially depleted of Ca^{2+} . To our knowledge, these types of responses are novel and are not reported in any other study that assessed Ca^{2+} release from the ER using NEPs in other cell types [54]. These observations point to the complexity of the mechanism by which the 5-ns pulse interacts with the intracellular membranes of chromaffin cells and indicate that factors other than electroporation, such as activation of signaling pathways inside the cell, might be responsible for the variable cell responses observed.

In conclusion, the overall findings of this work indicate that one general cell model cannot be used to explain NEP-induced effects in all cell types, and that outcomes from experiments conducted in one type of cell cannot be used to generalize NEP-induced responses, which can vary enormously between cells.

In this chapter, we propose some numerical modeling of a more realistic chromaffin cell and experimental ideas that might be helpful to further understand how a 5-ns electric pulse affects intracellular membranes of chromaffin cells in order to explain the experimental observations and obtain better agreement between the model and experiments, which is critical for understanding how NEPs affect the membranes of

intracellular organelles of chromaffin cells. These suggestions are outlined in the sections below for future extensions of the work described in this dissertation.

5.1 Further refinement of the numerical model: modeling a realistic shape of the ER

In the numerical models described in the previous chapters, the ER was represented by a circular structure because it was shown, theoretically [109] and experimentally [70], that for NEPs the TMP is independent of the organelle size and shape. However, because the models constructed in this study were unable to accurately explain the requirement for a high E-field amplitude to cause electroporation of the ER membrane, it is suggested here that a more realistic irregular shape of the ER be incorporated into the localized cell model and to investigate the influence on the electroporation of the ER membrane.

A numerical study conducted by Hao et al. (2014) in which an irregular shape of the inner mitochondrial membrane was considered in the model showed that only some of the mitochondrial membrane sites reached a TMP high enough to cause electroporation, while other areas of the membrane remained unelectroporated [111]. The difference in the electroporation at the different membrane locations was attributed to the high variations in the E-field associated with the large curvature of the mitochondrial membrane. Therefore, a numerical evaluation of the distribution of the TMP across an irregular membrane of the ER could determine whether any non-uniformities in the induced TMP, and thus pore density, occur. Outcomes from these simulations could be used to explain the requirement for high E-field amplitudes to cause sufficient membrane electroporation, leading to a detectable Ca^{2+} release from the ER.

5.2 Further exploration of a possible shielding effect

The localized model representing the ER surrounded by six secretory granules, which was described in Chapter 4, did not reveal any shielding effect of the granules on the ER membrane possibly because it was too simplistic compared to the crowded cytosol of a chromaffin cell that contains between 20,000 and 30,000 secretory granules/cell [88]. Further investigation is necessary to determine whether the presence of a large number of secretory granules affects the E-field distribution in the cytoplasm sufficiently to decrease the E-field amplitude and perhaps distribution at the location of the ER, thus requiring higher NEP amplitudes for porating the ER membrane.

The number of secretory granules that can be modeled using the 2D cell model constructed in this study is extremely limited due to the intensive computational resources needed. The use of a full wave electromagnetic field solver is being explored in our laboratory for modeling a chromaffin cell with many thousands of secretory granules.

5.3 Other possible mechanisms responsible for intracellular Ca^{2+} release

We have reported in the previous chapter that when the ER was partially depleted of Ca^{2+} , delayed Ca^{2+} responses were experimentally observed following pulse application. These responses were attributed to a delayed pulse effect on the cells. Even though we have convincing evidence that the 5-ns electric pulse is causing immediate poration of the ER membrane, leading to Ca^{2+} release from the ER, the delayed Ca^{2+} responses observed may be due to a delayed NEP-induced activation of the IP_3 - and/or ryanodine-receptors present in the ER membrane. The delay in the Ca^{2+} responses can be attributed to the time it takes

for a conformational change to occur in the protein present in the receptor, in other words, to the time it takes the receptor to go from a closed (inactive) to an open (active) state. In addition, if the receptors are not activated at the same time, Ca^{2+} could be released at different time points, which explains the multiple Ca^{2+} transients obtained.

Therefore, it is suggested that a possible NEP-induced activation of the receptors in the ER membrane be investigated. This can be accomplished by either blocking the IP_3Rs with 2-aminoethoxydiphenyl borate (2-APB) [145] or the RyRs with dantrolene [146]. Blocking the receptors could provide information about whether the delayed Ca^{2+} responses are truly due to a NEP-induced activation of the receptors, which is necessary for understanding the mechanism by which NEPs interact with intracellular membranes.

REFERENCES

- [1] J.C. Weaver and Y.A. Chizmadzhev. Theory of electroporation: A review. *Bioelectrochem. Bioenerg.*, 41: 135-160, 1996.
- [2] A. Barnett and J.C. Weaver. Electroporation: A unified, quantitative theory of reversible electrical breakdown and mechanical rupture in artificial planar bilayer membranes. *J. Electroanal. Chem.*, 320: 163-182, 1991.
- [3] M. Tarek. Membrane Electroporation: A Molecular Dynamics Simulation. *Biophys. J.*, 88: 4045-4053, 2005.
- [4] D.P. Tieleman. The molecular basis of electroporation. *BMC Biochem.*, 5: 10-21, 2004.
- [5] E. Neumann, S. Kakorin and K. Toensing. Fundamentals of electroporative delivery of drugs and genes. *Bioelectrochem. Bioenerg.*, 48: 3-16, 1999.
- [6] F. Andre and L.M. Mir. DNA electrotransfer: Its principles and an updated review of its therapeutic applications. *Gene Therapy*, 11: S33-S42, 2004.
- [7] S.I. Sukharev, V.A. Klenchin, S.M. Serov, L.V. Chernomordik and Y.A. Chizmadzhev. Electroporation and electrophoretic DNA transfer into cells - The effect of DNA interaction with electropores. *Biophys. J.*, 63: 1320-1327, 1992.
- [8] K.H. Schoenbach, A. Abou-Ghazala, T. Vithoulkas, R.W. Alden, R. Turner and S. Beebe. The effect of pulsed electrical fields on biological cells. *Pulsed Power Conf. Dig. Tech. Pap. 11th IEEE Int.*, 1: 73-78, 1997.
- [9] K.H. Schoenbach, S.J. Beebe and E.S. Buescher. Intracellular effect of ultrashort electrical pulses. *Bioelectromagnetics*, 22: 440-448, 2001.
- [10] K.S. Schoenbach, R. Joshi, J. Kolb, S. Buescher and S. Beebe. Subcellular effects of nanosecond electric pulses. *Conf. Proc. IEEE Eng. Med. Biol. Soc.*, 7: 5447-5450, 2004.
- [11] K.S. Schoenbach, B. Hargrave, R.P. Joshi, J. Kolb, C. Osgood, R. Nuccitelli, A.G. Pakhomov, J. Swanson, M. Stacey, J.A. White, S. Xiao and J. Zhang. Bioelectric effects of nanosecond pulses. *IEEE Trans. Dielectr. Electr. Insul.*, 14: 10881109, 2007.
- [12] S.J. Beebe, N.M. Sain and W. Ren. Induction of cell death mechanisms and apoptosis by nanosecond pulsed electric fields (nsPEFs). *Cells*, 2: 136-162, 2013.

- [13] S.J. Beebe, P.M. Fox, L.J. Rec, K. Somers, R.H. Stark and K.H. Schoenbach. Nanosecond pulsed electric field (nsPEF) effects on cells and tissues: Apoptosis induction and tumor growth inhibition. *IEEE Trans. Plasma Sci.*, 30: 286-292, 2002.
- [14] B.L. Ibey, A.G. Pakhomov, B.W. Gregory, V.A. Khorokhorina, C.C. Roth, M.A. Rassokhin, J.A. Bernhard, G.J. Wilmink and O.N. Pakhomova. Selective cytotoxicity of intense nanosecond-duration electric pulses in mammalian cells. *Biochim. Biophys. Acta*, 1800: 1210-1219, 2010.
- [15] A.T. Esser, K.C. Smith, T.R. Gowrishankar and J.C. Weaver. Towards solid tumor treatment by nanosecond pulsed electric fields. *Technol. Cancer Res. Treat.*, 8: 289-306, 2009.
- [16] K.J. Müller, V.L. Sukhorukov and U. Zimmermann. Reversible electropermeabilization of mammalian cells by high-intensity, ultra-short pulses of submicrosecond duration. *J. Membr. Biol.*, 184: 161-170, 2001.
- [17] T.R. Gowrishankar, A.T. Esser, Z. Vasilkoski, K.C. Smith and J.C. Weaver. Microdosimetry for conventional and supra-electroporation in cells with organelles. *Biochem. Biophys. Res. Commun.*, 341: 1266-1276, 2006.
- [18] D.A. Stewart, T.R. Gowrishankar and J.C. Weaver. Transport lattice approach to describing cell electroporation: Use of a local asymptotic model. *IEEE Trans. Plasma Sci.*, 32: 1696-1708, 2004.
- [19] K.C. Smith, T.R. Gowrishankar, A.T. Esser, D.A. Stewart and J.C. Weaver. The spatially distributed dynamic transmembrane voltage of cells and organelles due to 10-ns pulses: Meshed transport networks. *IEEE Trans. Plasma Sci.*, 34: 1394-1404, 2006.
- [20] Z. Vasilkoski, A.T. Esser, T.R. Gowrishankar and J.C. Weaver. Membrane electroporation: The absolute rate equation and nanosecond time scale pore creation. *Phys. Rev. E*, 74: 021904, 2006.
- [21] D.P. Tieleman, H. Leontiadou, A.E. Mark and S.J. Marrink. Molecular dynamics simulation of pore formation in phospholipid bilayers by mechanical force and electric fields. *J. Am. Chem. Soc.*, 125: 6382-6383, 2003.
- [22] P.T. Vernier, M.J. Ziegler, Y. Sun, W.V. Chang, M.A. Gundersen and D.P. Tieleman. Nanopore formation and phosphatidylserine externalization in a phospholipid bilayer at high transmembrane potential. *J. Am. Chem. Soc.*, 128:6288-6289, 2006.
- [23] U. Zimmermann. Electric field-mediated fusion and related electrical phenomena. *Biochim. Biophys. Acta*, 696: 227-277, 1982.

- [24] K. Kinoshita, I. Ashikawa, N. Saita, H. Yoshimura, H. Itoh, K. Nagayama and A. Ikegami. Electroporation of cell membrane visualized under pulsed-laser fluorescence microscope. *Biophys. J.*, 53: 1015-1019, 1988.
- [25] K.S. Cole. *Membranes, ions and impulses*. University of California Press, Berkeley, p. 569, 1972.
- [26] T. Kotnik and D. Miklavčič. Theoretical evaluation of voltage inducement on internal membranes of biological cells exposed to electric fields. *Biophys. J.*, 90: 480-491, 2006.
- [27] L.V. Chernomordik, S.I. Sukharev, I.G. Abidor and Y.A. Chizmadzhev. Breakdown of lipid bilayer membranes in an electric field. *Biochim. Biophys. Acta*, 736: 203-213, 1983.
- [28] R.W. Glaser, S.L. Leikin, L.V. Chernomordik, V.F. Pastushenko and A.I. Sokirko. Reversible electrical breakdown of lipid bilayers: Formation and evolution of pores. *Biochim. Biophys. Acta*, 940: 275-287, 1988.
- [29] R.P. Joshi, Q. Hu and K.H. Schoenbach. Modeling studies of cell response to ultrashort, high-intensity electric fields - Implications for intracellular manipulation. *IEEE Trans. Plasma Sci.*, 32: 1677-1686, 2004.
- [30] V.F. Pastushenko, Y.A. Chizmadzhev and V.B. Arakelyan. Electric breakdown of bilayer lipid membranes: II. Calculations of the membrane lifetime in the steady-state diffusion approximation. *Bioelectrochem. Bioenerg.*, 6: 53-62, 1979.
- [31] J.C. Weaver and R.A. Mintzer. Decreased bilayer stability due to transmembrane potential. *Phys. Lett. A.*, 86A: 57-59, 1981.
- [32] K.T. Powell and J.C. Weaver. Transient aqueous pores in bilayer membranes: A statistical theory. *Bioelectrochem. Bioenerg.*, 15: 211-227, 1986.
- [33] S.A. Freeman, M.A. Wang MA and J.C. Weaver. Theory of electroporation of planar bilayer membranes: predictions of the aqueous area, change in capacitance, and pore-pore separation. *Biophys. J.*, 67: 42-56: 1994.
- [34] J.C. Neu and W. Krassowska. Asymptotic model of electroporation. *Phys. Rev. E*, 59: 3471-3482, 1999.
- [35] J.C. Neu, K.C. Smith and W. Krassowska. Electrical energy required to form large conducting pores. *Bioelectrochem. Bioenerg.*, 60: 107-114, 2003.
- [36] R.S. Son, K.C. Smith, T.R. Gowrishankar, P.T. Vernier and J.C. Weaver. Basic features of a cell electroporation model: Illustrative behavior for two very different pulses. *J. Membrane Biol.*, 247: 1209-1228, 2014.

- [37] Z.A. Levine and P.T. Vernier. Life cycle of an electropore: Field-dependent and field-independent steps in pore creation and annihilation. *J. Memb. Biol.*, 236: 27-36, 2010.
- [38] K.C. Smith, R.S. Son, T.R. Gowrishankar and J.C. Weaver. Emergence of a large pore subpopulation during electroporating pulses. *Bioelectrochemistry*, 100: 3-10, 2014.
- [39] K.C. Smith. A unified model of electroporation and molecular transport. Ph.D. Thesis, Massachusetts Institute of Technology, 2011.
- [40] K.C. Smith and J.C. Weaver. Transmembrane molecular transport during versus after extremely large, nanosecond electric pulses. *Biochim. Biophys. Res. Commun.*, 412: 8-12, 2011.
- [41] A.T. Esser, K.C. Smith, T.R. Gowrishankar, Z. Vasilkoski and J.C. Weaver. Mechanisms for the intracellular manipulation of organelles by conventional electroporation. *Biophys. J.*, 98: 2506-2514, 2010.
- [42] K.C. Smith and J.C. Weaver. Active mechanisms are needed to describe cell responses to submicrosecond, megavolt-per-meter pulses: Cell models for ultrashort pulses. *Biophys. J.*, 95: 1547-1563, 2008.
- [43] Z.A. Levine and P.T. Vernier. Calcium and phosphatidylserine inhibit lipid electropore formation and reduce pore lifetime. *J. Membr. Biol.*, 245: 599-610, 2012.
- [44] M.C. Ho, M. Casciola, Z.A. Levine and P.T. Vernier. Molecular dynamics simulations of ion conductance in field-stabilized nanoscale lipid electropores. *J. Phys. Chem. B.*, 117: 11633-11640, 2013.
- [45] M.L. Fernández, M. Risk, R. Reigada and P.T. Vernier. Size-controlled nanopores in lipid membranes with stabilizing electric fields. *Biochem. Biophys. Res. Commun.*, 423: 325-330, 2012.
- [46] J.F. Kolb, S. Kono and K.H. Schoenbach. Nanosecond pulsed electric field generators for the study of subcellular effects. *Bioelectromagnetics* 27: 172-187, 2006.
- [47] A. Kuthi, P. Gabrielsson, M. Behrend, P.T. Vernier and M.A. Gundersen. Nanosecond pulse generator using fast recovery diodes for cell electromanipulation. *IEEE Trans. Plasma Sci.*, 33: 1192-1197, 2005.
- [48] T.B. Napotnik, M. Reberšek, T. Kotnik, E. Lebrasseur, G. Cabodevila, D. Miklavčič, Electroporation of endocytotic vesicles in B16 F1 mouse melanoma cells. *Med. Biol. Eng. Comput.*, 48: 407-413, 2010.

- [49] N. Chen, K.H. Schoenbach, J.F. Kolb, R.J. Swanson, A.L. Garner, J. Yang, R.P. Joshi and S.J. Beebe. Leukemic cell intracellular responses to nanosecond electric fields. *Biochem. Biophys. Res. Commun.*, 317: 421-427, 2004.
- [50] B. Napotnik, Y.H. Wu, M.A. Gundersen, D. Miklavčič and P.T. Vernier. Nanosecond electric pulses cause mitochondrial membrane permeabilization in Jurkat cells. *Bioelectromagnetics*, 33: 257-264, 2012.
- [51] S.J. Beebe, P.M. Fox, L.J. Rec, E.L. Willis and K.H. Schoenbach. Nanosecond, high-intensity pulsed electric fields induce apoptosis in human cells. *FASEB J.*, 17: 1493-1495, 2003.
- [52] S.S. Scarlett, J.A. White, P.F. Blackmore, K.H. Schoenbach and J.F. Kolb. Regulation of intracellular calcium concentration by nanosecond pulsed electric fields. *Biochim. Biophys. Acta Biomembr.*, 1788: 1168-1175, 2009.
- [53] P.T. Vernier, Y. Sun, L. Marcu, S. Salemi, C.M. Craft and M.A. Gundersen. Calcium bursts induced by nanosecond electric pulses. *Biochem. Biophys. Res. Commun.*, 310: 286-295, 2003.
- [54] I. Semenov, S. Xiao and A.G. Pakhomov. Primary pathways of intracellular Ca^{2+} mobilization by nanosecond pulsed electric field. *Biochim. Biophys. Acta Biomembr.*, 1828: 981-989, 2013a.
- [55] I. Semenov, S. Xiao, O.N. Pakhomova and A.G. Pakhomov. Recruitment of the intracellular Ca^{2+} by ultrashort electric stimuli: The impact of pulse duration. *Cell Calcium*, 54: 145-150, 2013b.
- [56] J.A. White, P.F. Blackmore, K.H. Schoenbach and S.J. Beebe. Stimulation of capacitative calcium entry in HL-60 cells by nanosecond pulsed electric fields. *J. Biol. Chem.*, 279: 22964-22972, 2004.
- [57] S.J. Beebe, P.F. Blackmore, J. White, R. Joshi and K.H. Schoenbach. Nanosecond pulsed electric fields modulate cell function through intracellular signal transduction mechanisms. *Physiol. Meas.*, 25: 1077-1093, 2004.
- [58] G.P. Tolstykh, H.T. Beier, C.C. Roth, G.L. Thompson, J.A. Payne, M.A. Kuipers and B.L. Ibey. Activation of intracellular phosphoinositide signaling after a single 600 nanosecond electric pulse. *Bioelectromagnetics*, 94: 23-29, 2013.
- [59] P.T. Vernier, Y. Sun, L. Marcu, C.M. Craft, M.A. Gundersen. Nanoelectropulse-induced phosphatidylserine translocation. *Biophys. J.*, 86: 4040-4048, 2004.
- [60] P.T. Vernier, Y. Sun and M.A. Gundersen. Nanoelectropulse-driven membrane perturbation and small molecule permeabilization. *BMC Cell Biol.*, 7: 37-52, 2006.

- [61] S. Romeo, Y.H. Wu, Z.A. Levine, M.A. Gundersen and P.T. Vernier. Water influx and cell swelling after nanosecond electropermeabilization. *Biochim. Biophys. Acta Biomembr.*, 1828: 1715-1722, 2013.
- [62] O.M. Nesin, O.N. Pakhomova, S. Xiao, A.G. Pakhomov: Manipulation of cell volume and membrane pore comparison following single cell permeabilization with 60- and 600-ns electric pulses. *Biochim. Biophys. Acta*, 1808: 792-801, 2011.
- [63] O.M. Nesin, A.M. Bowman, S. Xiao and A.G. Pakhomov. Cell permeabilization and inhibition of voltage-gated Ca^{2+} and Na^{+} channel currents by nanosecond pulsed electric fields. *Bioelectromagnetics*, 33: 394-404, 2012.
- [64] A. Silve, I. Leray and L.M. Mir. Demonstration of Cell Membrane Permeabilization to Medium-Sized Molecules Caused by a Single 10 ns Electric Pulse. *Int. Symp. Bioelectrochemistry Bioenerg.*, 21st BES 2011, 87: 260-264, 2012.
- [65] A.G. Pakhomov, J.F. Kolb, J.A. White, R.P. Joshi, S. Xiao and K.H. Schoenbach. Long-lasting plasma membrane permeabilization in mammalian cells by nanosecond pulsed electric field (nsPEF). *Bioelectromagnetics*, 28: 655-663, 2007a.
- [66] A.G. Pakhomov, R. Shevin, J.A. White, J.F. Kolb, O.N. Pakhomova, R.P. Joshi and K.H. Schoenbach. Membrane permeabilization and cell damage by ultrashort electric field shocks. *Arch. Biochem. Biophys.*, 465: 108-118, 2007b.
- [67] A.G. Pakhomov, A.M. Bowman, B.L. Ibey, F.M. Andre, O.N. Pakhomova and K.H. Schoenbach. Lipid nanopores can form a stable, ion channel-like conduction pathway in cell membrane. *Biochem. Biophys. Res. Commun.*, 385: 181-186, 2009a.
- [68] A.G. Pakhomov, B.L. Ibey, A.M. Bowman, F.M. Andre and O.N. Pakhomova. Nanosecond-duration electric pulses open nanometer-size pores in cell plasma membrane. *World Congr. Med. Phys. Biomed. Eng.*, Munich Ger. Springer Verlag., pp. 17-20, 2009b.
- [69] B.L. Ibey, S. Xiao, K.H. Schoenbach, M.R. Murphy and A.G. Pakhomov. Plasma membrane permeabilization by 60- and 600-ns electric pulses is determined by the absorbed dose. *Bioelectromagnetics*, 30: 92-99, 2009.
- [70] A.M. Bowman, O.M. Nesin, O.N. Pakhomova and A.G. Pakhomov. Analysis of plasma membrane integrity by fluorescent detection of Tl^{+} uptake. *J. Membr. Biol.*, 236: 15-26, 2010.
- [71] S. Wang, J. Chen, M.T. Chen, P.T. Vernier, M.A. Gundersen and M. Valderrábano. Cardiac Myocyte Excitation by Ultrashort High-Field Pulses. *Biophys. J.*, 96: 1640-1648, 2009.

- [72] C.C. Roth, G.P. Tolstykh, J.A. Payne, M.A. Kuipers, G.L. Thompson, M.N. DeSilva and B.L. Ibey. Nanosecond pulsed electric field thresholds for nanopore formation in neural cells. *J. Biomed. Opt.*, 3: 035005, 2013.
- [73] G.L. Craviso, P. Chatterjee, G. Maalouf, A. Cerjanic, J. Yoon, I. Chatterjee and P.T. Vernier. Nanosecond electric pulse-induced increase in intracellular calcium in adrenal chromaffin cells triggers calcium-dependent catecholamine release. *IEEE Trans. Dielectr. Electr. Insul.*, 16: 1294-1301, 2009.
- [74] G.L. Craviso, S. Choe, P. Chatterjee, I. Chatterjee and P.T. Vernier. Nanosecond electric pulses: A novel stimulus for triggering Ca^{2+} influx into chromaffin cells via voltage-gated Ca^{2+} channels. *Cell. Mol. Neurobiol.*, 30: 1259-1265, 2010.
- [75] A.S. Gorgey and G.A. Dudley. The role of pulse duration and stimulation duration in maximizing the normalized torque during neuromuscular electrical stimulation. *J. Orthop. Sports Phys. Ther.*, 38: 508-516, 2008.
- [76] J. Rozman, M. Bunc and B. Zorko. Modulation of hormone secretion by functional electrical stimulation of the intact and incompletely dysfunctional dog pancreas. *Braz. J. Med. Biol. Res.*, 37: 363-370, 2004.
- [77] E. Adeghate, A.S. Ponery and A. Wahab. Effect of Electrical Field Stimulation on Insulin and Glucagon Secretion from the Pancreas of Normal and Diabetic Rats. *Horm. Metab. Res.*, 33: 281-289, 2001.
- [78] H.S. Mayberg, A.M. Lozano, V. Voon, H.E. McNeely, D. Seminowicz, C. Hamani, J.M. Schwalb and S.H. Kennedy. Deep brain stimulation for treatment-resistant depression. *Neuron*, 45: 651-660, 2005.
- [79] J.F. Kerrigan, B. Litt, R.S. Fisher, S. Cranstoun, J.A. French, D.E. Blum, M. Dichter, A. Shetter, G. Baltuch, J. Jaggi, S. Krone, M. Brodie, M. Rise and N. Graves. Electrical stimulation of the anterior nucleus of the thalamus for the treatment of intractable epilepsy. *Epilepsia*, 45: 346-354, 2004.
- [80] G.L. Craviso, C. Fisher, I. Chatterjee and P.T. Vernier. Adrenal chromaffin cells do not swell when exposed to nanosecond electric pulses. *Bioelectrochemistry*, 103: 98-102, 2015.
- [81] A.G. García, A.M. García-De-Diego, L. Gandía, R. Borges and J. García-Sancho. Calcium Signaling and Exocytosis in Adrenal Chromaffin Cells. *Physiol. Rev.*, 86: 1093-1131, 2006.
- [82] J. García-Sancho and A. Verkhratsky. Cytoplasmic organelles determine complexity and specificity of calcium signalling in adrenal chromaffin cells. *Acta Physiol.*, 192: 263-271, 2008.

- [83] M. Montero, M.T. Alonso, E. Carnicero, I. Cuchillo-Ibáñez, A. Albillos, A.G. García, J. García-Sancho and J. Alvarez. Chromaffin-cell stimulation triggers fast millimolar mitochondrial Ca^{2+} transients that modulate secretion. *Nat. Cell Biol.*, 2: 57-61, 2000.
- [84] K. Mikoshiba. The InsP_3 receptor and intracellular Ca^{2+} signaling. *Curr. Opin. Neurobiol.*, 7: 339-345, 1997.
- [85] M.J. Berridge. Inositol triphosphate and diacylglycerol: Two interacting second messengers. *Annu. Rev. Biochem.*, 56: 159-193, 1987.
- [86] J. Meldolesi and T. Pozzan. The endoplasmic reticulum Ca^{2+} store: A view from the lumen. *Trends Biochem. Sci.*, 23: 10-14, 1998.
- [87] T. Pozzan, R. Rizzuto, P. Volpe and J. Meldolesi. Molecular and cellular physiology of intracellular calcium stores. *Physiol. Rev.*, 74: 595-636, 1994.
- [88] H. Plattner, A.R. Artalejo and E. Neher. Ultrastructural organization of bovine chromaffin cell cortex-analysis by cryofixation and morphometry of aspects pertinent to exocytosis. *J. Cell Biol.*, 139: 1709-1717, 1997.
- [89] S.H. Yoo and J.P. Albanesi. High capacity, low affinity Ca^{2+} binding of chromogranin A. Relationship between the pH-induced conformational change and Ca^{2+} binding property. *J. Biol. Chem.*, 266: 7740-7745, 1991.
- [90] P.T. Vernier, Y. Sun, M.T. Chen, M.A. Gundersen and G.L. Craviso. Nanosecond electric pulse-induced calcium entry into chromaffin cells. *Bioelectrochemistry*, 73: 1-4, 2008.
- [91] J. Yoon, N. Leblanc, J. Zaklit, P.T. Vernier, I. Chatterjee and G.L. Craviso. Enhanced monitoring of nanosecond electric pulse-evoked membrane conductance changes in whole-cell patch clamp experiments. *J. Membr. Biol.*, 249: 1-12, 2016.
- [92] G.L. Craviso, S. Chloe, I. Chatterjee and P.T. Vernier. Modulation of intracellular Ca^{2+} levels in chromaffin cells by nanoelectropulses. *Bioelectrochemistry*, 87: 244-252, 2012.
- [93] K.C. Smith. Modeling cell and tissue electroporation. MS thesis, Massachusetts Institute of Technology, 2006.
- [94] P.O. Persson and G. Strang. A simple mesh generator in MATLAB. *SIAM Review*, 46: 329-345, 2004.
- [95] F. Aurenhammer. Voronoi diagrams: A survey of a fundamental geometric data structure. *ACM Comput. Surv.*, 23: 345-405, 1991.

- [96] K.A. DeBruin and W. Krassowska. Modeling electroporation in a single cell. I. Effects of field strength and rest potential. *Biophys. J.*, 77: 1213-1224, 1999.
- [97] A.C. Sabuncu, J. Zhuang, J.F. Kolb and A. Beskok. Microfluidic impedance spectroscopy as a tool for quantitative biology and biotechnology. *Biomicrofluidics*, 6: 34103, 2012.
- [98] V. Raicu, T. Saibara, H. Enzan and A. Irimajiri. Dielectric properties of rat liver in vivo: analysis by modeling hepatocytes in the tissue architecture. *Bioelectrochem. Bioenerg.*, 47: 333-342, 1998.
- [99] J. Chen, M. Abdelgawad, L. Yu, N. Shakiba¹, W.Y. Chien, Z. Lu, W.R. Geddie, M.A.S Jewett and Y. Sun. Electrodeformation for single cell mechanical characterization. *J. Micromech. Microeng.* 21: 054010, 2011.
- [100] Y. Zhao, D. Chen, H. Li, Y. Luo, B. Deng, S.B. Huang, T.K. Chiu, M.H. Wu, R. Long, H. Hu, J. Wang and J. Chen. A microfluidic system enabling continuous characterization of specific membrane capacitance and cytoplasm conductivity of single cells in suspension. *Biosens. Bioelectron.*, 43: 304-307, 2013.
- [101] A. Irimajiri, Y. Doida, T. Hanai and A. Inouye. Passive electrical properties of cultured murine lymphoblast (L5178Y) with reference to its cytoplasmic membrane, nuclear envelope, and intracellular phases. *J. Membr. Biol.*, 38: 209-232, 1978.
- [102] Y. Polevaya, I. Ermolina, M. Schlesinger, B.Z. Ginzburg and Y. Feldman. Time domain dielectric spectroscopy study of human cells: II. Normal and malignant white blood cells. *Biochim. Biophys. Acta*, 1419: 257-271, 1999.
- [103] J. Yang, Y. Huang, X. Wang, X.B. Wang, F.F. Becker and P.R. Gascoyne. Dielectric properties of human leukocyte subpopulations determined by electrorotation as a cell separation criterion. *Biophys. J.*, 76: 3307-3314, 1999.
- [104] F.H. Labeed, H.M. Coley and M.P. Hughes. Differences in the biophysical properties of membrane and cytoplasm of apoptotic cells revealed using dielectrophoresis. *Biochim. Biophys. Acta*, 1760: 922-929, 2006.
- [105] H. Pauly, L. Packer and H.P. Schwan. Electrical properties of mitochondrial membranes. *J. Biophysic. and Biochem. Cytol.*, 7: 589-601, 1960.
- [106] H. Pauly and L. Packer. The relationship of internal conductance and membrane capacity to mitochondrial volume. *J. Biophysic. and Biochem. Cytol.*, 7: 603-612, 1960.
- [107] J.C. Waymire, W.F. Bennett, R. Boeheme, L. Hankins, K.G. Waymire and J.W. Haycock. Bovine adrenal chromaffin cells: High-yield purification and viability in suspension culture. *J. Neurosci. Methods*, 7: 329-351, 1983.

- [108] G.L. Craviso. Generation of functionally competent single bovine adrenal chromaffin cells from cell aggregates using the neutral protease dispase. *J. Neurosci. Methods*, 137: 275-281, 2004.
- [109] L. Rems, M. Ušaj, M. Kandušer, M. Reberšek, D. Miklavčič and G. Pucihar. Cell electrofusion using nanosecond electric pulses. *Sci. Rep.*, 3: 3382, 2013.
- [110] R.C. Valentine and D.L. Valentine. *Neurons and the DHA principles*. CRC Press, Taylor and Francis Group, 2013.
- [111] H. Qiu, S. Xiao and R.P. Joshi. Simulations of voltage transients across intracellular mitochondrial membranes due to nanosecond electrical pulses. *IEEE Trans. Plasma Sci.*, 42: 3113-3120, 2014.
- [112] I. Semenov, S. Xiao, D. Kang, K.H. Schoenbach and A.G. Pakhomov. Cell stimulation and calcium mobilization by picosecond electric pulses. *Bioelectrochemistry*, 105: 65-71, 2015.
- [113] M.H. Shirvan, H.B. Pollard and E. Heldman. Mixed nicotinic and muscarinic features of cholinergic receptor coupled to secretion in bovine chromaffin cells. *Proc. Natl. Acad. Sci.*, 88: 4860-4864, 1991.
- [114] A.J. O'Sullivan, T.R. Cheek, R.B. Moreton, M.J. Berridge, R.D. Burgoyne. Localization and heterogeneity of agonist-induced changes in cytosolic calcium concentration in single bovine adrenal chromaffin cells from video imaging of fura-2. *EMBO J.*, 8: 401-411, 1989.
- [115] T.R. Cheek and R.D. Bourgogne. Effect of activation of muscarinic receptors on intracellular free calcium and secretion in bovine adrenal chromaffin cells. *Biochim. Biophys. Acta*, 846: 167-173, 1985.
- [116] L. Retelj, G. Pucihar and D. Miklavčič. Electroporation of intracellular liposomes using nanosecond electric pulses - A theoretical study. *IEEE Trans. Biomed.*, 60: 2624-2635, 2013.
- [117] T. Hagan. Finite-Difference Time-Domain modeling of a waveguide-based radiofrequency exposure system for studying non-thermal effects on catecholamine release from chromaffin cells - Characterization and optimization. MS thesis, University of Nevada Reno, 2005.
- [118] R. P. Joshi, A. Nguyen, V. Sridhara, Q. Hu, R. Nuccitelli, S. J. Beebe, J. Kolb and K. H. Schoenbach. Simulations of intracellular calcium release dynamics in response to a high-intensity, ultrashort electric pulse. *Phys. Rev. E*, 75: 041920, 2007.

- [119] J.D. Machado, M. Camacho, J. Alvarez and R. Borges. On the role of intravesicular calcium in the motion and exocytosis of secretory organelles. *Commun. Integr. Biol.*, 2: 71-73, 2009.
- [120] E.M. Fenwick, A. Marty and E. Neher. A patch-clamp study of bovine chromaffin cells and of their sensitivity to acetylcholine. *J. Physiol.*, 331: 577-597, 1982.
- [121] M. Sorimachi, K. Yamagami, T. Yada and S. Nishimura. Spontaneous and secretagogue-induced changes in cytosolic free Ca^{2+} concentration measured by microfluorimetry with fura-2 on single bovine adrenal chromaffin cells. *Jpn. J. Physiol.*, 39: 687-701, 1989.
- [122] V. Nassar-Gentina, H. B. Pollard and E. Rojas. Electrical activity in chromaffin cells of intact mouse adrenal gland. *Am. J. Physiol. Cell Physiol.*, 254: C675-C683, 1988.
- [123] M. Fill and R. Coronado. Ryanodine receptor channel of sarcoplasmic reticulum. *Trends Neurosci.*, 11: 453-457, 1988.
- [124] M.T. Alonso, M.J. Barrero, P. Michelena, E. Carnicero, I. Cuchillo, A.G. García, J. García-Sancho, M. Montero and J. Alvarez. Ca^{2+} -induced Ca^{2+} release in chromaffin cells seen from inside the ER with targeted aequorin. *J. Cell. Biol.*, 144: 241-254, 1999.
- [125] A. Verkhratsky. Physiology and pathophysiology of the calcium store in the endoplasmic reticulum of neurons. *Physiol. Rev.*, 85: 201-279, 2005.
- [126] N. Solovyova and A. Verkhratsky. Neuronal endoplasmic reticulum acts as a single functional Ca^{2+} store shared by ryanodine and inositol-1,4,5-trisphosphate receptors as revealed by intra-ER [Ca^{2+}] recordings in single rat sensory neurones. *Pflügers Arch.*, 446: 447-454, 2003.
- [127] T.R. Cheek, R.B. Moreton, M.J. Berridge, K.A. Stauderman, M.M. Murawsky and M.D. Bootman. Quantal Ca^{2+} release from caffeine-sensitive stores in adrenal chromaffin cells. *J. Biol. Chem.*, 268: 27076-27083, 1993.
- [128] T.R. Cheek, M.M. Murawsky and K.A. Stauderman. Histamine-induced Ca^{2+} entry precedes Ca^{2+} mobilization in bovine adrenal chromaffin cells. *Biochem. J.*, 304: 469-476, 1994.
- [129] P.S. Liu, Y.J. Lin and L.S. Kao. Caffeine-sensitive calcium stores in bovine adrenal chromaffin cells. *J. Neurochem.*, 56: 172-177, 1991.
- [130] K.A. Stauderman, R.A. McKinney and M.M. Murawsky. The role of caffeine-sensitive Ca^{2+} stores in agonist- and inositol 1,4,5-trisphosphate-induced Ca^{2+} release from bovine adrenal chromaffin cells. *Biochem. J.*, 278: 643-650, 1991.

- [131] B.E. Ehrlich, E. Kaftan, S. Bezprozvannaya and I. Bezprozvanny. The pharmacology of intracellular Ca^{2+} -release channels. *Trends Pharmacol. Sci.*, 15: 145-149, 1994.
- [132] H. Teraoka, Y. Nakazato and A. Ohga. Ryanodine inhibits caffeine-evoked Ca^{2+} mobilization and catecholamine secretion from cultured bovine adrenal chromaffin cells. *J. Neurochem.*, 57: 1884-1890, 1991.
- [133] S.J. Smith, T. Imagawa, J. Ma, M. Fill, K.P. Campbell and R. Coronado. Purified ryanodine receptor from rabbit skeletal muscle is the calcium-release channel of sarcoplasmic reticulum. *J. Gen. Physiol.*, 92: 1-26, 1988.
- [134] O. Thastrup. Role of Ca^{2+} -ATPases in regulation of cellular Ca^{2+} signalling, as studied with the selective microsomal Ca^{2+} -ATPase inhibitor, thapsigargin. *Agents and Actions*, 29: 8-15, 1990.
- [135] J.C.J. Poulsen, C. Caspersen, D. Mathiasen, J.M. East, R.E.A. Tunwell, F.A. Lai, N. Maeda, K. Mikoshiba and M. Treiman. Thapsigargin-sensitive Ca^{2+} -ATPases account for Ca^{2+} uptake to inositol 1,4,5-trisphosphate-sensitive and caffeine-sensitive Ca^{2+} stores in adrenal chromaffin cells. *Biochem. J.*, 307: 749-758, 1995.
- [136] J. Novalbos, F. Abad-Santos, P. Zapater, J. Alvarez, M.T. Alonso, M. Montero and A.G. García. Novel antimigraineur dotarizine releases Ca^{2+} from caffeine-sensitive Ca^{2+} stores of chromaffin cells. *British J. Pharm.*, 128: 621- 626, 1999.
- [137] I.M. Robinson, T.R. Cheek and R.D. Burgogne. Ca^{2+} influx induced by the Ca^{2+} -ATPase inhibitors 2,5-di-(t-butyl)-1,4-benzohydroquinone and thapsigargin in bovine adrenal chromaffin cells. *Biochem. J.*, 288: 457-463, 1992.
- [138] H. Winkler and E. Westhead. The molecular organization of adrenal chromaffin granules. *Neurosci.*, 5: 1803-1823, 1980.
- [139] J.R. Haigh, R. Parris and J.H. Phillips. Free concentrations of sodium, potassium and calcium in chromaffin granules. *Biochem. J.*, 259: 485-491, 1989.
- [140] J. SantoDomingo, L. Vay, M. Camacho, E. Hernández-SanMiguel, R.I. Fonteriz, C.D. Lobatón, M. Montero, A. Moreno and J. Alvarez. Calcium dynamics in bovine adrenal medulla chromaffin cell secretory granules. *Eur. J. Neurosci.*, 28: 1265-1274, 2008.
- [141] Y.H. Huh, J.A. Yoo, S.J. Bahk and S.H. Yoo. Distribution profile of inositol 1,4,5-trisphosphate receptor isoforms in adrenal chromaffin cells. *FEBS Lett.*, 579: 2597-2603, 2005.
- [142] J. Alvarez. Calcium dynamics in the secretory granules of neuroendocrine cells. *Cell Calcium*, 51: 331-337, 2012.

- [143] R. Borges, N. Domínguez, J. Estévez-Herrera, D. Pereda and J.D. Machado. Vesicular Ca^{2+} mediates granule motion and exocytosis. *Cell Calcium*, 51: 338-341, 2012.
- [144] C.L. Haynes, L.A. Buhler and R.M. Wightman. Vesicular Ca^{2+} -induced secretion promoted by intracellular pH-gradient disruption. *Biophys. Chem.*, 123: 20-24, 2006.
- [145] A.N. Donald, D.J. Wallace, S. McKenzie and P.D. Marley. Phospholipase C-mediated signalling is not required for histamine-induced catecholamine secretion from bovine chromaffin cells. *J. Neurochem.*, 81: 1116-1129, 2002.
- [146] J. Egea, A.O. Rosa, A. Cuadrado, A.G. García and M.G. López. Nicotinic receptor activation by epibatidine induces heme oxygenase-1 and protects chromaffin cells against oxidative stress. *J. Neurochem.*, 12: 1842-1852, 2007.

APPENDIX A: Abstract of Paper Presented at the Annual Meeting of Bioelectromagnetics Society (BioEM2015), Asilomar, CA, June 14-19, 2015

Ca²⁺ release from internal stores of adrenal chromaffin cells is not evoked by 5 ns electric pulses *

Josette El Zaklit¹, Jihwan Yoon¹, Indira Chatterjee¹, Eric Evans², P. Thomas Vernier³, Normand Leblanc², and Gale L. Craviso²

¹Department of Electrical and Biomedical Engineering, College of Engineering, University of Nevada-Reno, Reno, NV, USA, 89557

²Department of Pharmacology, University of Nevada School of Medicine, Reno, NV, USA, 89557

³Frank Reidy Research Center for Bioelectrics, Norfolk, VA, USA, 23508

Keywords

Chromaffin cells; Nanosecond pulses; Intracellular Ca²⁺; Ca²⁺ influx; Calcium green-1; Carbachol

Summary

Nanosecond electric pulses have been shown to affect intracellular structures in different cell types and evoke a number of cellular responses, such as Ca²⁺ release from internal stores. Adrenal chromaffin cells, however, do not show evidence of Ca²⁺ release from internal stores when exposed to trains of 5 ns pulses but clearly show Ca²⁺ mobilization from internal stores when stimulated by brief exposure to a receptor agonist. The basis for the lack of effect on intracellular Ca²⁺ stores by 5 ns pulses is unclear since preliminary cell modeling results suggest that pores are formed on intracellular membranes.

Introduction

A distinguishing feature of nanosecond-duration electric pulses is that their effects can penetrate into the interior of cells and impact intracellular membrane structures by causing, for example, poration that can lead to the release of Ca²⁺ from internal stores [1]. However, we have previously reported that when excitable adrenal chromaffin cells are exposed to up to ten, 5 ns pulses, the only response observed is influx of Ca²⁺ through voltage-gated Ca²⁺ channels (VGCC). No evidence of Ca²⁺ release from intracellular stores is apparent [2-4].

* BioEM2015 second place platform presentation student award winner.

The present study was undertaken to further address the issue of the lack of poration of intracellular Ca^{2+} stores in these cells. The first goal was to establish that release of Ca^{2+} from intracellular stores is detectable under conditions in which the cells are stimulated by the brief application (several milliseconds) of a drug that evokes both Ca^{2+} influx via VGCC and Ca^{2+} mobilization from intracellular stores. For this purpose, we used the mixed receptor agonist carbachol that causes simultaneous activation of nicotinic and muscarinic acetylcholine receptors. The second goal was to determine whether exposure of the cells to 5 ns pulses under conditions in which sustained rather than transient Ca^{2+} responses are triggered [5] involves Ca^{2+} influx as well as Ca^{2+} release from intracellular stores. The third goal was to construct a two-dimensional cell model based on the meshed transport network method (MTNM) developed by Smith and Weaver [6] to provide insight into the intracellular membrane porative effects of a 5 ns pulse on the cells.

Methods

Bovine chromaffin cells were isolated from the medulla of adrenal glands and maintained in suspension culture. Dissociation of the large aggregates of cells into single isolated cells was carried out using the protease dispase. For fluorescence imaging of intracellular Ca^{2+} , cells were plated onto fibronectin-coated glass-bottomed dishes and loaded with Calcium Green-1 as described [2-4]. The dishes were placed on the stage of a Nikon TE2000 epifluorescence microscope equipped with an Andor iXon DU-897 EMCCD camera. Images were analyzed with the open source microscopy software μ Manager. Cells were bathed in the same balanced salt solution as the one stated previously [2-4].

For receptor agonist stimulation of the cells, the agonists were applied with a pressure ejection Picospritzer^R system. The glass micropipette containing the drug had a tip diameter of 1 μm that was positioned at a distance of one cell diameter from the target cell. A program written in LabVIEW triggered the ejection of the drugs, with the duration of the pressure pulse set at 5 ms. When experiments were carried out with a VGCC blocker, cells were incubated with the blocker for at least 30 minutes before initiating experiments.

5 ns pulse exposure of the cells was carried out by a pulse delivery system that consisted of two cylindrical tungsten rod electrodes spaced 60 μm apart. Pulses were delivered to the electrodes by a fast-recovery diode-switching pulse generator [7]. For exposures, the electrodes were positioned at the bottom of the culture dish by a micromanipulator, with the cell located in the middle of the gap between the electrode tips. Pulse delivery was controlled by a program written in LabVIEW.

The two-dimensional cell model consisted of a chromaffin cell represented by a sphere of radius 8 μm (cell diameter of 16 μm as reported in Craviso et al. [8]) surrounded by a membrane of thickness 5 nm. A spherical nucleus with a radius of 3 μm and a membrane thickness of 10 nm was added off-centered to the cell geometry [6]. The active two-dimensional cell model was constructed using the MTNM [6] and the electrical response of the cell was based on the asymptotic model of electroporation developed by Neu and Krassowska [9]. The simulations were performed using the actual 5 ns pulse trace obtained

from an oscilloscope. Cell membrane parameters (i.e. membrane capacitance and membrane resistance) and balanced salt solution properties (i.e. solution conductivity) were determined in our laboratory by patch clamp (membrane test) and conductivity measurements, respectively. The remaining parameters (i.e. nuclear membrane conductivity and permittivity, cytoplasm conductivity and permittivity, nucleoplasm conductivity and permittivity) were taken from the literature.

Results

To establish the effectiveness of the drug delivery system for evoking Ca^{2+} responses, chromaffin cells were first stimulated with the selective nicotinic cholinergic receptor agonist, 1,1-dimethyl-4-phenylpiperazinium (DMPP) that is known to cause a rapid and transient rise in intracellular Ca^{2+} due solely to influx of Ca^{2+} via voltage-gated Ca^{2+} channels. A single 5 ms application of DMPP caused a rapid and transient rise in intracellular Ca^{2+} . No intracellular Ca^{2+} increase occurred when Ca^{2+} was absent from the balanced salt solution bathing the cells, or when voltage-gated Ca^{2+} channels were blocked with nitrendipine. In contrast, stimulation of the cells with the mixed nicotinic-muscarinic receptor agonist carbachol that is known to evoke a rise in intracellular Ca^{2+} mediated both by Ca^{2+} influx (as a result of nicotinic receptor activation) and release of Ca^{2+} from intracellular stores (as a result of muscarinic receptor activation) caused an elevation of intracellular Ca^{2+} in both the presence and absence of extracellular Ca^{2+} . These results indicate that Ca^{2+} mobilization from internal stores can be readily observed in response to a very brief stimulus.

Exposing the cells to either one pulse or a train of ten, 5 ns pulses under conditions that trigger sustained rather than transient increases in intracellular Ca^{2+} [5] still did not cause detectable Ca^{2+} release from intracellular stores since the Ca^{2+} response was totally absent when Ca^{2+} was eliminated from the extracellular medium. Thus, 5 ns exposure experiments to date have yet to provide evidence of poration of intracellular membranes. These findings are inconsistent with preliminary cell modeling results which indicate that intracellular poration should occur.

Conclusions

Ca^{2+} release from internal stores was used as a determinant of intracellular effects of 5 ns pulses on chromaffin cells. To date we have no evidence of poration of Ca^{2+} storing membrane structures caused by exposure of the cells to 5 ns pulses. Although there may well be intracellular effects, Ca^{2+} mobilization due to membrane poration is not one of them. Future efforts will be directed at reconciling the basis for the disparity between cell modeling results and experimental findings.

Acknowledgements

This work was supported by Grants FA9550-14-1-0018 (G.L. Craviso) and FA9550-14-1-0123 (P.T. Vernier) from the Air Force Office of Scientific Research.

References

- [1] S.S. Scarlett, J.A. White, P.F. Blackmore, K.H. Schoenbach, J.F. Kolb. Regulation of intracellular calcium concentration by nanosecond pulsed electric fields. *Biochim. Biophys. Acta* 1788:1168-1175, 2009.
- [2] P.T. Vernier, Y. Sun, M.T. Chen, M.A. Gundersen and G.L. Craviso. Nanosecond electric pulse-induced calcium entry into chromaffin cells. *Bioelectrochemistry* 73:1-4, 2008.
- [3] G. L. Craviso, S. Choe, P. Chatterjee, I. Chatterjee and P.T. Vernier. Nanosecond electric pulses: a novel stimulus for triggering Ca^{2+} influx into chromaffin cells via voltage-gated Ca^{2+} channels. *Cell. Mol. Neurobiol.* 30:1259-1265, 2010.
- [4] G. L. Craviso, S. Choe, P. Chatterjee, I. Chatterjee and P.T. Vernier. Modulation of intracellular Ca^{2+} levels in chromaffin cells by nanoelectropulses. *Bioelectrochemistry* 87:244-252, 2012.
- [5] J. Yoon, J. El Zaklit, I. Chatterjee, P. T. Vernier, N. Semenova, N. Leblanc and G. L. Craviso. Transient versus sustained Ca^{2+} responses evoked in chromaffin cells by 5 ns pulses: pulse delivery considerations. Abstract, Annual Meeting of the Bioelectromagnetics Society, 2015.
- [6] K.C. Smith and J.C. Weaver. Active mechanisms are needed to describe cell responses to submicrosecond, megavolt-per-meter pulses: Cell models for ultrashort pulses. *Biophys. J.*, 95:1547-1563, 2008.
- [7] A. Kuthi, P.G. Son, M.R. Behrend, P.T. Vernier and M.A. Gundersen. Nanosecond pulse generator using fast recovery diodes for cell electromanipulation. *IEEE Trans. Plasma Sci.* 33: 1192-1197, 2005.
- [8] G. L. Craviso, C. Fisher, I. Chatterjee and P.T. Vernier. Adrenal chromaffin cells do not swell when exposed to nanosecond electric pulses. *Bioelectrochemistry* 103:98-102, 2015.
- [9] J.C. Neu and W. Krassowska. Asymptotic model of electroporation. *Phys. Rev. E*, 59:3471-3482, 1999.

APPENDIX B: Abstract of Paper Presented at the Annual Meeting of Bioelectromagnetics Society (BioEM2016), Ghent, Belgium, June 5-10, 2016

Numerical modeling of intracellular adrenal chromaffin cell responses to high intensity 5 ns electric pulses

Josette Zaklit¹, Gale L. Craviso², Normand Leblanc², Robert Terhune¹, and Indira Chatterjee¹

¹Department of Electrical and Biomedical Engineering, College of Engineering, University of Nevada, Reno, NV, USA, 89557

²Department of Pharmacology, University of Nevada School of Medicine, Reno, NV, USA, 89557

Keywords

Cell modeling; Parametric study; Nanosecond electric pulses; Adrenal chromaffin cells; Intracellular Ca²⁺

Summary

Exposing adrenal chromaffin cells to a 5 ns electric pulse requires a twofold or greater electric field (E-field) amplitude to cause Ca²⁺ release from internal stores than to stimulate Ca²⁺ influx. To examine why intracellular responses require a higher field amplitude, a 2D cell model was constructed to assess pore formation in Ca²⁺-storing organelle membranes. The modeling results suggest that E-field values as low as ~3 MV/m cause pores to form within intracellular membranes, thus contrasting with experimental findings. A parametric study was designed to optimize E-field and cytoplasm conductivity in the cell model for which modeling and experimental results give comparable field threshold values for intracellular Ca²⁺ release.

Introduction

High intensity nanosecond electric pulses can penetrate inside cells and influence intracellular structures by causing, for instance, Ca²⁺ release from internal stores [1]. However, 5 ns pulses applied at an E-field of 5-6 MV/m (at the location of the cell), which is effective for stimulating Ca²⁺ influx, fails to elicit Ca²⁺ release from internal stores in bovine adrenal chromaffin cells [2-4]. In this study, both *in vitro* experiments and numerical modeling approaches were used to assess membrane poration in intracellular Ca²⁺-storing organelles of chromaffin cells exposed to 5 ns pulses. Fluorescence imaging experiments were conducted to determine the threshold value of the E-field amplitude that causes Ca²⁺ release from internal stores. For this purpose, chromaffin cells were exposed to a single 5 ns pulse of different amplitudes while monitoring intracellular Ca²⁺ responses

in the absence of extracellular Ca^{2+} . Such Ca^{2+} responses were used as a determinant of intracellular effects of 5 ns pulses on chromaffin cells. Next, a 2D model representative of a chromaffin cell was constructed to validate the requirement for high field amplitudes to cause intracellular membrane poration in chromaffin cells exposed to 5 ns pulses. A numerical parametric study was conducted to find the E-field threshold for membrane poration of Ca^{2+} -storing organelles. Since the dielectric properties of chromaffin cells are unknown and presently being determined [5], the cytoplasm conductivity (σ_{cyto}) was chosen as another parameter to be varied in the model.

Methods

Preparation of chromaffin cells and fluorescence microscopy

Bovine chromaffin cells were isolated from the adrenal gland and maintained in suspension culture. Large cell clusters were dissociated into single cells with the protease dispase. For fluorescence imaging of intracellular Ca^{2+} , cells were plated onto 35-mm glass bottom dishes coated with fibronectin and loaded with the fluorescent dye Calcium Green-1 as previously described [6, 7]. After washing off the dye, cells were bathed in a Ca^{2+} -free balanced salt solution (BSS) with the following composition: 145 mM NaCl, 5 mM KCl, 1.2 mM NaH_2PO_4 , 1.3 mM MgCl_2 , 1 mM EGTA, 10 mM glucose, 15 mM Hepes, pH 7.4. The dishes of cells were then placed on the stage of a Nikon TE 2000 inverted microscope equipped with a 100X fluorescence objective. Images were captured by an iXonEM + DU-897 EMCCD camera and analyzed with the open source software Micro-Manager.

Pulse delivery system

Nanosecond pulses were applied by means of two cylindrical gold-plated tungsten rod electrodes spaced 100 μm apart. The tips of the electrodes were immersed in the BSS and placed 40 μm above the bottom of the dish, with the cell being imaged positioned in the center of the gap between the electrode tips. Single pulses with amplitudes that produced E-fields ranging from 2 to 20 MV/m at the location of the cells (as determined by Finite-Difference Time-Domain (FDTD) modeling using the software SEMCAD X (SPEAG, Zurich, Switzerland)) were delivered to the electrodes using a nanosecond pulse generator (Transient Plasma Systems), and the pulse traces were captured with an oscilloscope. Each cell was exposed only once to the applied E-field.

Numerical modeling

Construction of the model

The 2D cell model was constructed based on the meshed transport network method (MTNM) developed by Smith and Weaver [8], and the electrical response of the cell was based on the asymptotic model of electroporation developed by Neu and Krassowska [9]. The chromaffin cell model (Figure 1a) consisted of a circle of radius 8 μm (chromaffin cell radius measured in our laboratory) centered inside a bounding box of dimensions 100 μm x 100 μm . Intracellular Ca^{2+} -storing organelles [10] consisted of a large double-membrane circular structure representing a cell nucleus of radius 2.5 μm [11] (the intermembrane space between the membranes was neglected) and a smaller circular double-membrane

structure representing a mitochondrion of 1 μm radius, with the inner (IMM) and outer mitochondrial membranes (OMM) separated by a 15 nm intermembrane space filled with electrolyte. Other Ca^{2+} -storing intracellular organelles were the endoplasmic reticulum (ER), which in chromaffin cells is localized throughout the cytoplasm [12] and represented for simplicity by a circular single membrane structure of radius 500 nm, and a secretory vesicle represented by a single membrane structure of radius 400 nm (because of computational limitations, smaller structures more representative of the nanometer-diameter secretory vesicles [11] could not be modeled). All four structures were placed off-center inside the cell.

Parameters of the model

Plasma membrane resistance (8.3×10^{-10} S/m) and BSS conductivity (1.3 S/m) were measured in our laboratory and used in the model. All other electrical and electroporation parameters were taken from the literature [13, 14]. To take into account the folding of the IMM, the effective IMM area was increased by a factor of 5 compared to the OMM by increasing the local capacitance fivefold [15]. The model took into account the resting potential of the plasma membrane, IMM and secretory vesicle membrane. The two membranes forming the nuclear envelope were considered identical, and the voltage was equally distributed between both membranes. Therefore, the transmembrane potential (TMP) across one nuclear membrane was calculated as half the TMP across the whole nuclear envelope [13, 16]. The actual pulse traces captured during the experiments (Figure 1b) were implemented in the numerical model.

Parametric study and membrane electroporation

The range chosen for σ_{cyto} was 0.1 to 1.3 S/m. The nucleoplasmic conductivity was set to $2\sigma_{\text{cyto}}$ and was changed accordingly [13]. The E-field created by the pulse at the location of the cell ranged from 1 to 20 MV/m, and the temporal evolution and spatial distribution of the TMP and pore density induced in the intracellular membranes were computed. The threshold E-field for significant electroporation was defined as the value for which the pore density at the anodic pole (i.e. the point where the pore density is the highest) of a membrane reached 10^{14} m^{-2} . The membrane was then considered electroporated [13].

Results and Discussion

The experimental application of a single 5 ns electric pulse to adrenal chromaffin cells showed that Ca^{2+} was released from internal stores at E-field amplitudes greater than 8 MV/m. Below this threshold value, no detectable Ca^{2+} release from the cells was observed. In addition, the magnitude of the Ca^{2+} response increased as a function of E-field amplitude.

The 2D cell modeling results indicated that the E-field threshold for electroporating the different intracellular structures by a single 5 ns pulse can be as low as 2.6 MV/m, thus contrasting with experimental results. On the other hand, pore density on all intracellular

membranes increased as the E-field amplitude was increased, consistent with the experimental findings (Figure 2).

Not yet known is the source of Ca^{2+} that is being released in chromaffin cells in response to a 5 ns pulse. The ER, which has been shown to be the target of nanosecond electric pulses in other cell types [1], is a likely source of Ca^{2+} released in chromaffin cells as well. Moreover, another potential target of nanosecond pulses in chromaffin cells is the Ca^{2+} -storing secretory vesicles. Because these vesicles occupy ~30% of the volume of the cytosol [11], we considered the possibility that their presence might affect the dielectric properties of the cytoplasm and thus the modeling results. To address this issue, σ_{cyto} was varied in the model. Figure 3 shows the influence of σ_{cyto} on the E-field threshold values necessary for electroporating the membranes of the different Ca^{2+} -storing intracellular organelles. For the single-membrane organelles that are likely targets (i.e. ER and secretory vesicles), the E-field thresholds for causing their membranes to porate did not exceed 5.5 MV/m regardless of the σ_{cyto} values tested in the simulations. The modeling results thus did not agree with a greater than 8 MV/m E-field needed to show release of Ca^{2+} from internal stores. On the other hand, for σ_{cyto} values greater than 0.3 S/m the modeling results agreed with the experimental findings showing that a lower E-field causes electropermeabilization of the plasma membrane [17] compared to that causing pore formation in the ER and secretory vesicles. Clearly, changing the cytoplasm conductivity alone was not sufficient to explain why higher E-fields were needed to porate intracellular membranes. The model needs to be further refined to identify the electrical parameters for the ER and secretory vesicles that will give results similar to those obtained experimentally.

Conclusions

Establishing agreement between the experimental findings and modeling results will help to explain why E-field thresholds for stimulating chromaffin cells by causing Ca^{2+} influx and those for causing Ca^{2+} release from internal stores differ by more than twofold in magnitude. Such knowledge is important for verifying that nanosecond pulses can excite chromaffin cells and cause Ca^{2+} influx that triggers exocytosis and catecholamine release without causing additional, unwanted effects on intracellular structures.

Acknowledgements

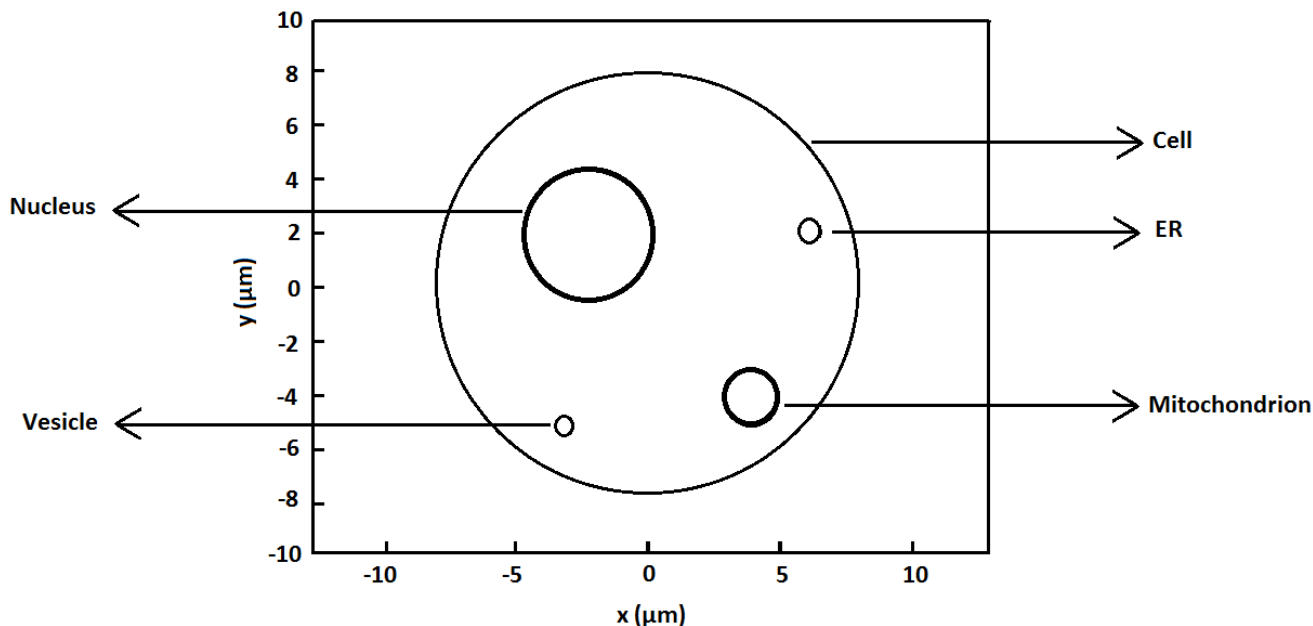
This work was supported by Grant FA9550-14-1-0018 (G.L. Craviso) from the Air Force Office of Scientific Research.

References

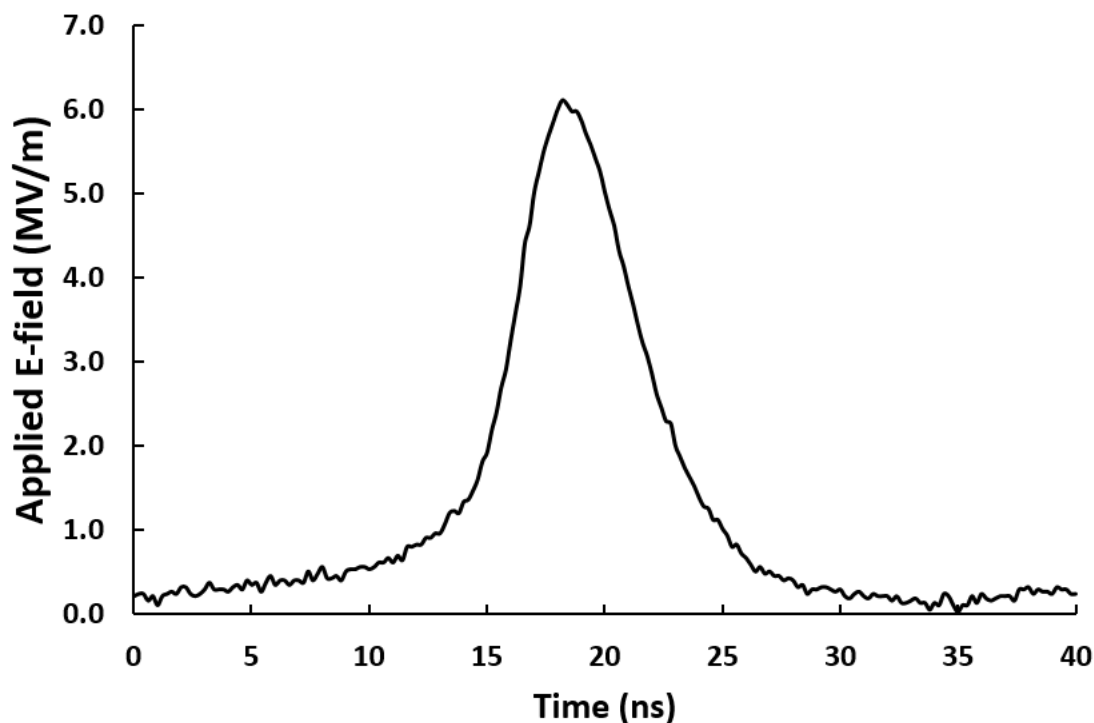
- [1] S.S. Scarlett, J.A. White, P.F. Blackmore, K.H. Schoenbach and J.F. Kolb, *Biochim. Biophys. Acta* **1788**, 1168 (2009).
- [2] P.T. Vernier, Y. Sun, M.T. Chen, M.A. Gundersen and G.L. Craviso, *Bioelectrochemistry* **73**, 1 (2008).
- [3] J. Zaklit, J. Yoon, I. Chatterjee, E. Evans, P. T. Vernier, N. Leblanc and G. L. Craviso, *Proceedings of the Annual Meeting of the Bioelectromagnetics Society and the European Bioelectromagnetics Association*, 2015.

- [4] Personal communications with Nina Semenova and P. Thomas Vernier (Frank Reidy Research Center for Bioelectrics, Old Dominion University, Norfolk, VA, USA).
- [5] Personal communications with Michael Stacey (Frank Reidy Research Center for Bioelectrics, Old Dominion University, Norfolk, VA, USA) and Ahmet Can Sabuncu (Department of Mechanical Engineering, Southern Methodist University, Dallas, TX, USA).
- [6] G. L. Craviso, S. Choe, P. Chatterjee, I. Chatterjee and P.T. Vernier, *Cell. Mol. Neurobiol.* **30**, 1259 (2010).
- [7] G. L. Craviso, S. Choe, P. Chatterjee, I. Chatterjee and P.T. Vernier, *Bioelectrochemistry* **87**, 244 (2012).
- [8] K.C. Smith and J.C. Weaver, *Biophys. J.* **95**, 1547 (2008).
- [9] J.C. Neu and W. Krassowska, *Phys. Rev. E* **59**, 3471 (1999).
- [10] J. García-Sancho and A. Verkhratsky, *Acta Physiol.* **192**, 263 (2008).
- [11] H. Plattner, A.R. Artalejo and E. Neher, *J. Cell Biol.* **139**, 1709 (1997).
- [12] Y. H. Huh, S. J. Bahk, J. Y. Ghee and S. H. Yoo, *FEBS Letters* **579**, 5145 (2005).
- [13] L. Retelj, G. Pucihar and D. Miklavčič, *IEEE Trans. Biomed. Eng.* **60**, 2624 (2013).
- [14] H. Qiu, S. Xiao and R. P. Joshi, *IEEE Trans. Plasma Sci.* **42**, 3113 (2014).
- [15] T. R. Gowrishankar, A. T. Esser, Z. Vasilkoski, K. C. Smith and J. C. Weaver, *Biochem. Biophys. Res. Commun.* **341**, 1266 (2006).
- [16] L. Rems, M. Ušaj, M. Kandušer, M. Reberšek, D. Miklavčič and G. Pucihar, *Scientific Reports* **3**, Article number 3382 (2013).
- [17] J. Yoon, N. Leblanc, J. Zaklit, P. T. Vernier, I. Chatterjee and G. L. Craviso, *J. Membr. Biol.* (Submitted).

Figures



a.



b.

Figure 1: a. Cell system geometry. The cell (radius = $8\ \mu\text{m}$) was centered in a $100\ \mu\text{m} \times 100\ \mu\text{m}$ region representing the $100\ \mu\text{m}$ gap between the electrodes. The E-field was applied to the anode, placed at $x = -50\ \mu\text{m}$. The cathode was represented by the ground and placed at $x = 50\ \mu\text{m}$. A large structure representing the nucleus (radius = $2.5\ \mu\text{m}$) was placed at $(-2\ \mu\text{m}, 2\ \mu\text{m})$. Structures representing the mitochondria (inner radius = $1\ \mu\text{m}$), the ER (radius = $500\ \text{nm}$) and a large vesicle (radius = $400\ \text{nm}$) were placed at $(4\ \mu\text{m}, -4\ \mu\text{m})$, $(6\ \mu\text{m}, 2\ \mu\text{m})$ and $(-3\ \mu\text{m}, -5\ \mu\text{m})$, respectively. Double-membrane structures were represented by thicker lines. b. Example of an actual $5\ \text{ns}$, $6\ \text{MV/m}$ pulse delivered in experiments to chromaffin cells, and used in the numerical model. The $5\ \text{ns}$ pulse duration corresponded to the width at half maximum. The total pulse duration was $40\ \text{ns}$.

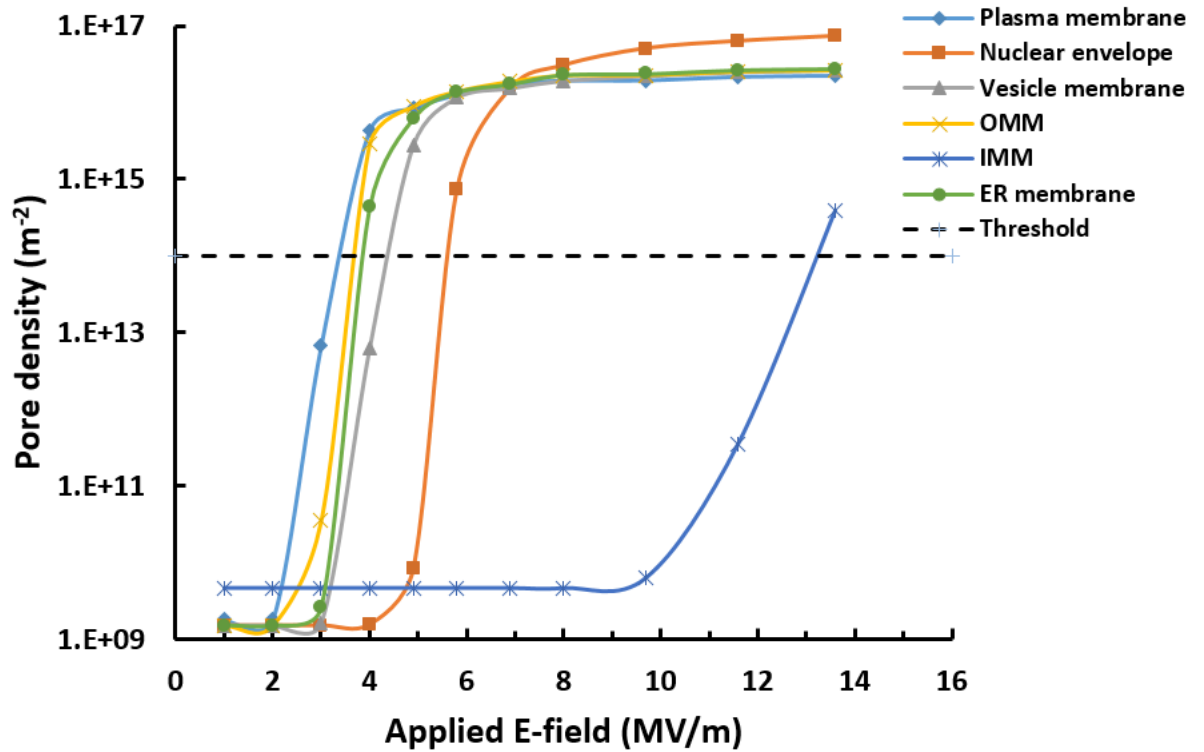


Figure 2: Pore density at the anodic pole of the different membranes as a function of E-field amplitude at the location of the cell, for $\sigma_{\text{cyto}} = 0.3 \text{ S/m}$. The membranes are considered to be electroporated when a pore density of $N = 10^{14} \text{ m}^{-2}$ (dashed line) is reached.

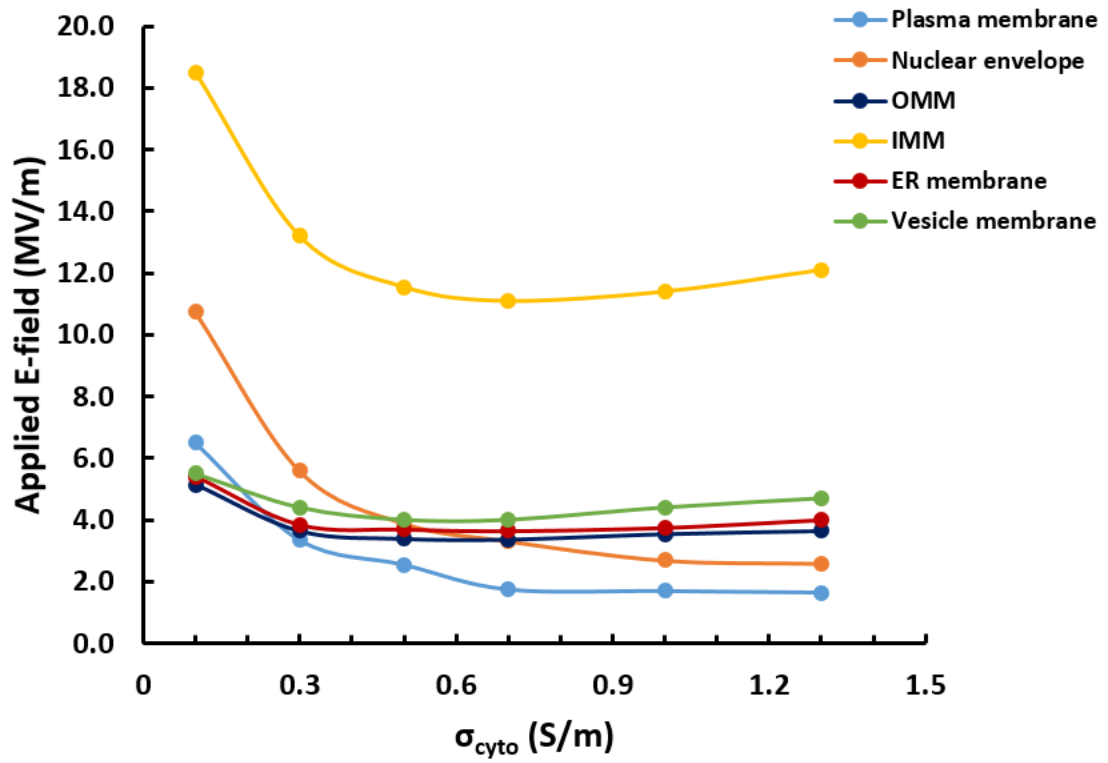


Figure 3: Influence of σ_{cyto} on the E-field threshold values that cause poration of the plasma membrane, nuclear envelope, OMM, IMM, ER membrane and vesicle membrane.